DESIGN OF A DIRECT PI CONTROLLER WITHOUT THE FEEDFORWARD TERMS FOR A VSC-BASED PMSG WIND TURBINE

By

Khethizwe Sihlangu Sukati

A thesis submitted in fulfillment of the requirements for the degree of
MASTER OF SCIENCE IN ELECTRICAL ENGINEERING

DEPARTMENT OF ELECTRICAL, ELECTRONIC AND COMPUTER ENGINEERING
COLLEGE OF AGRICULTURE, ENGINEERING AND SCIENCE
UNIVERSITY OF KWAZULU-NATAL

September 2018

Supervisor:	Prof. David Dorrell
Co-Supervisor:	Prof. John Agee

DECLARATION 1-PLAGIARISM

I, Khethizwe Sihlangu Sukati, declare that

1. The research reported in this dissertation, except where otherwise indicated, is my original research.
2. This dissertation has not been submitted for any degree or examination at any other university.
3. This dissertation does not contain other person's data, pictures, graphs or other information unless specifically acknowledged as being sourced from other persons.
4. This dissertation does not contain other person's writing unless specifically acknowledged as being sourced from other researchers. Where other written sources have been quoted, then:
   a. Their words have been re-written but the general information attributed to them has been referenced.
   b. Where their exact words have been used, then their writing has been placed in italics and inside quotation marks and referenced.
5. This dissertation does not contain text, graphics or tables copied and pasted from the internet, unless specifically acknowledged, and the source being detailed in the thesis and in the Reference sections.

Signed:

…………………………………………….

Mr. Khethizwe Sihlangu Sukati

As the candidate's Supervisor, I agree/do not agree to the submission of this thesis. Signed:

……………………………………………	……………………………………………
Prof. David Dorrell	Prof. John Agee
Date:	Date:

DEDICATION

Dedicated, in thankful appreciation for the support, encouragement, and understanding to my most valued and beloved family, my fiancée, my child, church members, friends and relatives.

ACKNOWLEDGEMENTS

May I take this opportunity to sincerely thank the almighty God for his wisdom, guidance and being the source of my strength and enabled me to successfully conduct this project.

My utmost gratitude extends to all the people who inspired, encouraged, and supported me during the course of this research work:

- My main supervisor, Prof David Dorrell for critically reviewing my works and his invaluable professional and career-building advice, guidance and his enormous patience throughout the development of my research.

- My co-supervisor, Prof. John Agee for his guidance throughout the duration of my studies, for assisting me in understanding the purpose of research works and identifying focus area

- My caring and loving family, relatives, friends and fellow colleagues who have helped and given me encouragement throughout the duration of my studies.

- Eskom, for granting me financial support to pursue my studies under the Eskom Power Plant Engineering Institute (EPPEI) Program. Thank you for believing in me and awarding me the financial grant.

ABSTRACT

Renewable energy (RE) sources – wind and solar, have received attention in South Africa and across the world from investors. The development of the Voltage Source Converter (VSC) has enabled large amount of RE to be integrated to the grid. Direct-drive permanent magnet synchronous generators (PMSGs) are now widely available. A PMSG wind turbine employs a full back-to-back VSC arrangement which is controlled via a pulse width modulated system of insulated gate bipolar transistors (IGBTs). Conventional PI vector controllers have been widely used to control VSC based PMSGs. This thesis proposes a new direct PI controller which excludes the decoupled terms in the configurations. A 690 V, 2 MW direct-drive PMSG wind turbine is modelled in PowerSim (PSIM) to investigate the proposed vector control configuration performance under varying wind speeds.

A detailed mathematical model of a wind turbine and a PMSG is developed. Then a VSC-HVDC detailed modelled is presented. The proposed control configuration is introduced. An optimal torque control Maximum Power Point Tracking (MPPT) algorithm and vector control method are applied to implement the system.

Finally, simulation studies are carried out to investigate the performance of the proposed controller configuration. A deduction from the results obtained, this thesis successfully implemented the new proposed controller configuration. It can be concluded, therefore, that VSC-based PMSG can be implemented in practice using a direct PI controller to reduce system complexity and improve controller performance.

Index Terms: Wind power, VSC, PMSG, HVDC, control

DECLARATION 2- PUBLICATIONS

The following publications emanated from this research work:

[1] K.S. Sukati, D. Dorrell, J. Agee "A Controller Feedback Design with QFT for a VSC-HVDC link" *Proceedings of the 4th Eskom Power Plant Engineering Institute Student Workshop*, Eskom Academy of Learning, Midrand, South Africa, 29-30 May 2017

[2] K. S. Sukati, D. G. Dorrell and J. Agee, "A Direct PI Controller without the Feedforward Terms for a VSC-based Permanent Magnet Synchronous Generator for a Wind Turbine," IEEE International Industrial Electronics Conference (IECON), October 2018

Signed:

…………………………………………….
Khethizwe Sukati

TABLE OF CONTENTS

LIST OF TABLES

LIST OF FIGURES

LIST OF ACRONYMS

DFIG	Doubly Fed Induction Generator
GSC	Generator Side Converter
HVDC	High Voltage Direct Current
MPPT	Maximum Power Point Tracking
MSC	Machine Side Converter
OTC	Optimum Torque Control
PCC	Point of Common Coupling
PLL	Phase-Locked-Loop
PMSG	Permanent Magnate Synchronous Generator
PWM	Pulse Width Modulation
REIPPPP	South African Renewable Energy Independent Power Producer Procurement Programme
SCIG	Squirrel Cage Induction Generator
SPWM	Sinusoidal Pulse Width Modulation
TSR	Tip Speed Ratio
VSC	Voltage Source Converter
VSC-HVDC	Voltage Source Converter based High Voltage Direct Current

CHAPTER 1: INTRODUCTION AND LITERATURE REVIEW

1.1 Introduction

Renewable energy generation has gained much attention from investors in South Africa and across the world: the South African government has, through the Integrated Resource Plan (IRP 2010), made a commitment to derive 17 800 MW (42%) of utility produced power from renewable sources: wind power production systems and solar plants (CSP and PV). The renewable energy pricing has competitively edged that from non-renewable energy sources: for the third tendering process in August 2013, the price for solar PV and onshore wind were R0.88/kWh and R0.66/kWh respectively. Comparing these prices to that of coal-fired power stations such as the estimates for Medupi and Kusile (R1.05 kWh), the wind and solar renewable sources have achieved pricing parity with the grid and with future projections continuing to forecast a drop, renewable energy sources are more cost effective other than preventing the carbon emissions.

Currently there are 12 wind farms in South Africa. Eskom owns a 100MW Sere Wind Farm worth R2.7 Billion with another Solar PV 100MW along the pipeline. This underlines the vast interest into the renewable energy industry and further project an upward trend. Land accessibility and existing grid infrastructures are limiting factors in the construction of wind farms. Wind power potential is best along the coastline. This will push investors to consider offshore investment. This project, therefore, proposes a modelling of several Direct Drive generators for offshore integration to the Eskom grid.

Direct Drive generators have been employed since 1992. The generator can be a synchronous machine excited using a rotor winding or a permanent magnet (PM). The high magnet prices around the year 2011 have increased the interest in alternatives for PMs [1]. Variable speed operation is preferred as it yields 20-30% more energy than the fixed speed operation, reduces power fluctuations and improves reactive power supply [2].

There are three commonly used variable speed wind turbines: 1.) Doubly-Fed Induction Generator (DFIG) which is attached to the grid via a half-rated power converter, 2.) Direct-driven or geared Squirrel-Cage Induction Generator (SCIG) connected to the utility grid through a fully –rated power converter, 3.) And the emerging one which is the focus of this research; Permanent Magnet Synchronous Generator (PMSG) which is coupled to the grid using a fully-rated power converter. [3]. The application of a half-rated or reduced rating of the power converter in the DFIG system is considered as a generous advantage in terms of cost of the system. Reference [3] estimates the rating of the power converter for the DFIG to be 30% of its power rating.

The generator speed in the DFIG system is limited to a range of 30% of its rated speed. In the PMSG and SCIG systems a fully rated converter is used hence the generator operates at full speed range. Having the generator fully decoupled from the grid presents great opportunities in terms of project costs reduction: the fully rated power converter shields the generator from propagating faults if occurred in the grid-side-of the converter. This, therefore, reduces the protection costs for systems such as PMSG, and SCIG. This cost reduction opportunity, however, is not available to DFIG system since they employ partially rated power converters connected to the rotor windings.

The main challenge of the vector control technique is the decoupling of the frequency induced terms. In [4] and[5], the conventional vector control structure has been implemented by adding the decoupled terms and putting limiters before the pulse width modulation (PWM) block to avoid the PWM from entering saturation mode. In [6], an optimal control of a PMSG wind turbine system under a direct-current dq vector configuration is proposed. The work done in [6] challenges the conventional vector control configuration where the current signal is added to the decoupled terms before it is sent to the PWM block. Reference [6] proposes that the current signal be converted to a voltage signal thereafter be sent to the PWM block.

1.1.1 Purpose of the thesis and main contribution

The core objective of this project is to study, develop and design a direct robust PI control system for a Direct Drive generator to improve onshore wind integration into the utility grid. The project is be simulated in Psim and Matlab software. The robust PI controller should be able to reject disturbances.

There are other different types of control system designs that have been applied in technical literature beside the common conventional PI controller: Multivariable Dynamic Model (MDM) and Backstepping Finite Time Fast Sliding Mode (BFTSM). The MDM is a very much improved control system as compared to the other vastly employed controllers in technical literature. It uses the instantaneous real and reactive power components as the dynamic variables. This exploits the main feature of Voltage Source Converter (VSC): its decoupled instantaneous real and reactive power control capability [7-9]. This, therefore, differentiates it from the common control methods which use conventional *dq* current components as dynamic variables, real and reactive power components produce their own waveforms irrespective of the used reference frame; differing from other electrical parameters [10]. This makes it possible to determine the real and reactive power components instantaneous values from the *abc* reference frame. The main drawback of the real and reactive power based model approach is the inability to control overcurrent to the acceptable limits [10]. On the other hand, BFTSM models the variations in the converter system due to disturbances in system inputs and frequency of the system [11].

From the literature review, the widely used control configuration is the conventional controller configuration where the decoupled terms are added. Therefore, the main contribution of this thesis, is to propose a new controller configuration: direct-current vector control without decoupled terms (DVCWDT). This controller exploits the advantages of using a feedback design to strategically set the integrator in the PI controller to negate the effects of the decoupled terms and produces a controller configuration structure without the decoupled terms. The proposed control configuration is then simulated in the Psim software to analyse the performance of the system.

1.1.2 Thesis organisation

The thesis is made up of seven chapters: chapter 1 gives the introduction and the background of the literature including the overview of the progress of renewable energy implementation in South Africa. Chapter 2 and 3 introduce the deep understanding for the wind turbine and PMSG systems then the VSC-HVDC systems. Chapter 4 gives the component sizing and rating of each item that is used in this project together with the justification and reasoning behind the choices made. Engineering trade-offs are made with a goal of achieving better performances and efficiency. The full design of the controllers is presented in chapter 5 where the modifications and optimisations are done to produce a good robust controller. Chapter 6 discusses the results obtained from the simulations. Chapter 7 provides a conclusion from the system project and the discussions made. It further makes suggestions on how the system can be developed and applied in other projects.

1.2 Literature Review

1.2.1 Overview of Renewable Wind Energies in South Africa

In 2011, South Africa adopted a renewable energy plan – Renewable Energy Independent Power Producer Procurement Programme (REIPPPP). This plan has already attracted approximately R200 billion private investments since its inception.

The SA REIPPPP provides an open tender process platform where private investors competitively bid. Four bidding rounds have been concluded from 2011 to 2015 where 390 submissions were made and only 92 were awarded the tenders to procure 6 328 MW power valued at R193 billion investment [11].

The total installed wind power in SA has been progressively growing since 2011. The DoE created a “determination” of how much new generation capacity is required at a particular window and is bound by the Electricity Regulation Act of 2006 (Amended in 2007) read together with the Electricity Regulation on new generation capacity published in November 2010 and May 2011. The first determination required a maximum and a great response from private investors, the second determination was opened very close in 2012 where an additional 1 470 MW was made available for REIPPPP wind power generation. Further to that in 2015, almost double of the two 2011 and 2012 determinations was availed for REIPPPP bidding ,see table 1-1 [11].

Table 1-1: The determinations of the wind power for the REIPPPP allocated by Minister of Energy to date [11]

Technology	**First Determination (Aug-2011)**	**Second Determination (Oct-2012)**	**Third Determination (Aug-2015)**	**Total**	**Percentage of total**
Onshore wind (MW)	1,850	1,470	3,040	6,360	48%
Concentrated Solar Plant (CSP) (MW)	200	400	600	1,200	9%
Solar PV (MW)	1,450	1,075	2,200	4,725	36%
Biomass (MW)	13	48	150	210	2%
Biogas (MW)	13	48	50	110	1%
Landfill gas (MW)	25	0	0	25	0%
Small hydro (≤ 40MW)	75	60	60	195	1%
Small Projects (1-5MW)	100	100	200	400	3%
Total (MW)	**3,725**	**3,200**	**6,300**	**13,225**	**100%**

To date, a total of 2 094 MW wind power has been installed in South Africa, see figure 1.1 below [12]. As of end of 2016, 1 473 MW had been installed. In 2017, 621 MW wind power was installed.

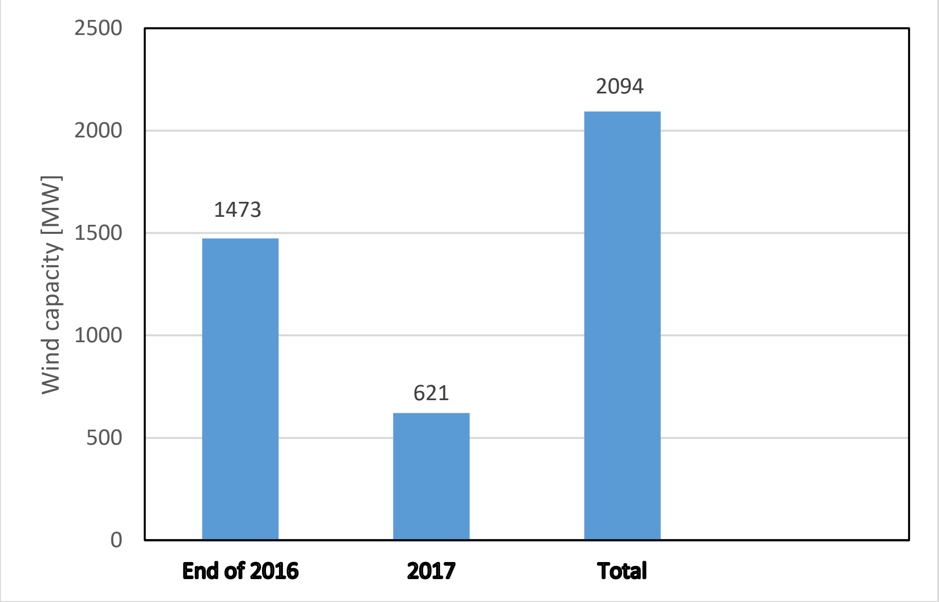

Figure 1.1: The SA cumulative wind capacity 2011-2017

South Africa leads the African and Middle East regions on wind power production, see figure 1.2 [12]. Egypt is the second with a total of 810 MW. In 2017, there were no newly installed wind power from Egypt, Morocco, Ethiopia and Tunisia. This slows down the growth rate projection for the Africa continent. Governments should continue to create incentives in this continent.

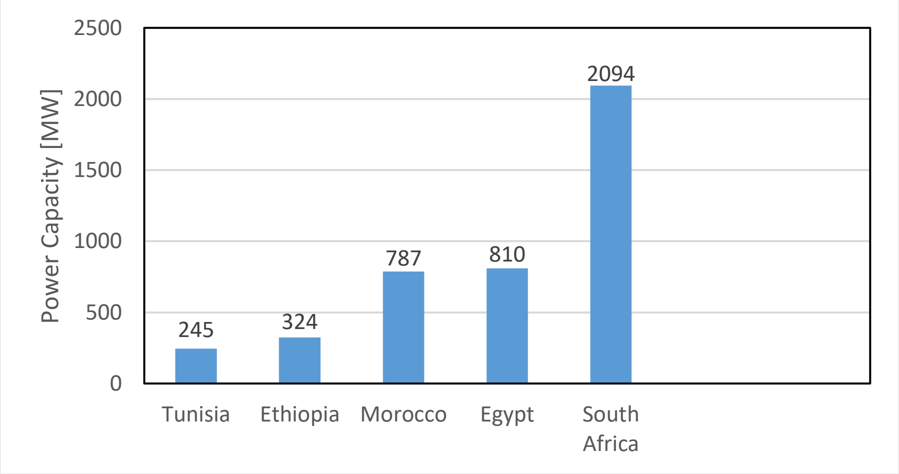

Figure 1.2: Installed wind power capacity in some African countries

South Africa is doing well as compared to other countries globally. In 2017, 52 573 MW wind capacity was installed globally of which 621 MW came from South Africa. This represents 1.18% global share. China leads the world with 19 500 MW installed wind capacity followed by United State of America (USA) with 7 017 MW. Germany was third with 6 581 MW, United Kingdom (UK) had 4 2750 MW and completing the world's top 5 was India with 4 148 MW, see figure 1.3 below.

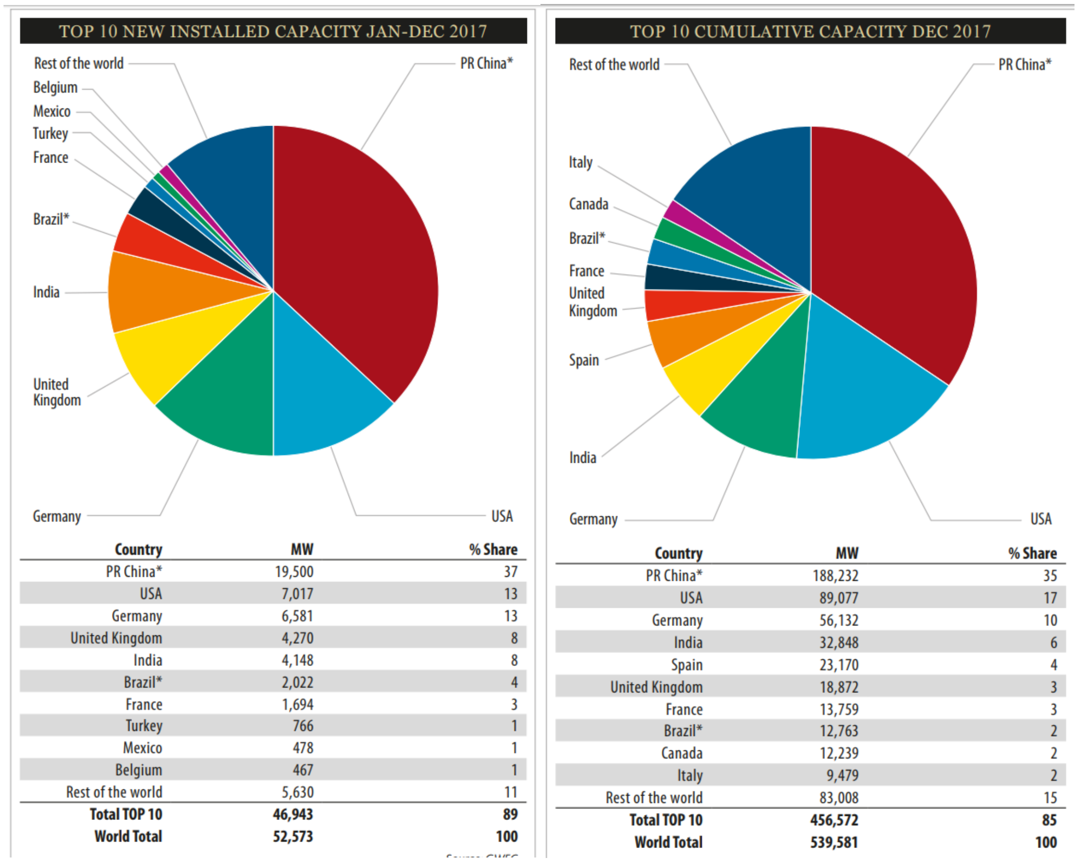

Country	MW	% Share
PR China*	19,500	37
USA	7,017	13
Germany	6,581	13
United Kingdom	4,270	8
India	4,148	8
Brazil*	2,022	4
France	1,694	3
Turkey	766	1
Mexico	478	1
Belgium	467	1
Rest of the world	5,630	11
Total TOP 10	**46,943**	**89**
World Total	**52,573**	**100**

Country	MW	% Share
PR China*	188,232	35
USA	89,077	17
Germany	56,132	10
India	32,848	6
Spain	23,170	4
United Kingdom	18,872	3
France	13,759	3
Brazil*	12,763	2
Canada	12,239	2
Italy	9,479	2
Rest of the world	83,008	15
Total TOP 10	**456,572**	**85**
World Total	**539,581**	**100**

Figure 1.3: Top ten new installed capacity and top ten cumulative capacity globally [12]

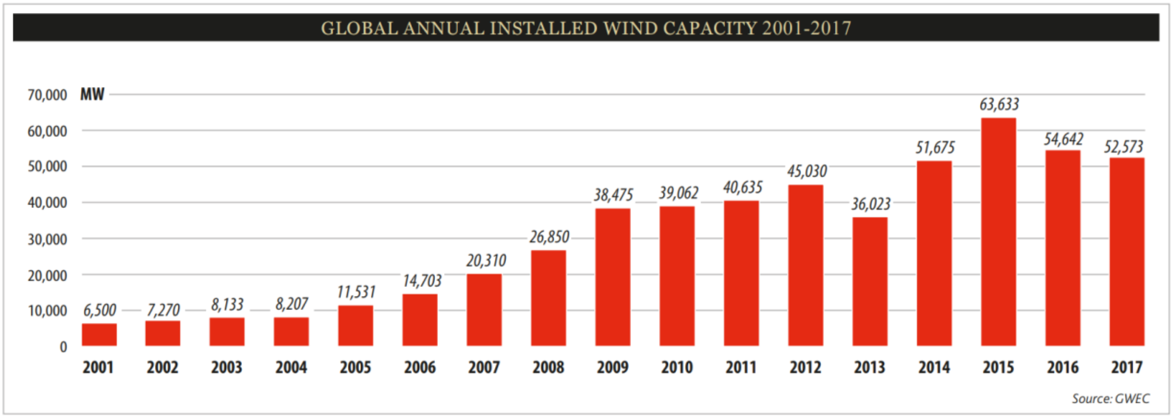

Source: GWEC

Figure 1.4: Total global annual installed wind capacity [12]

The total cumulative installed wind capacity in 2017 globally stands at 539 587 MW. SA stands at 2 094 MW. This represents a share of 0.388% from SA. This is clear that SA holds a more promising market for renewable energy developments. Again the top five countries cumulative capacity in the world by Dec 2017 is: China with 188 232 MW (35%), USA had 89 077 MW (17%), Germany had 56 132 MW (10%), India had 32 848 (6%) and completing the top 5 is Spain with 23 170 MW (4%), see figure 1.5 [12] below.

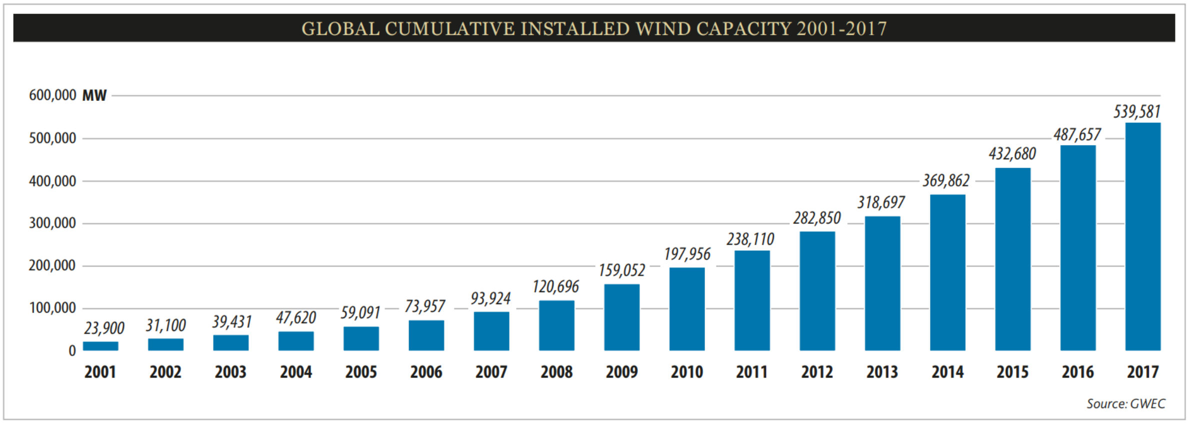

Figure 1.5: Global cumulative installed wind capacity [12]

The table 1-2 below shows a list of the top five wind farms in operation in South Africa currently.

Table 1-2: The top five wind farms in South Africa based on production capacity.

Wind farms	**Capacity (MW)**	**Location**
1. Cookhouse	138.6	Eastern Cape
2. Jeffery’s Bay	136	Eastern Cape
3. Dorper	100	Eastern Cape
4. Sere	100	Western Cape
5. Nobelsfontein	73.8	Northern Cape

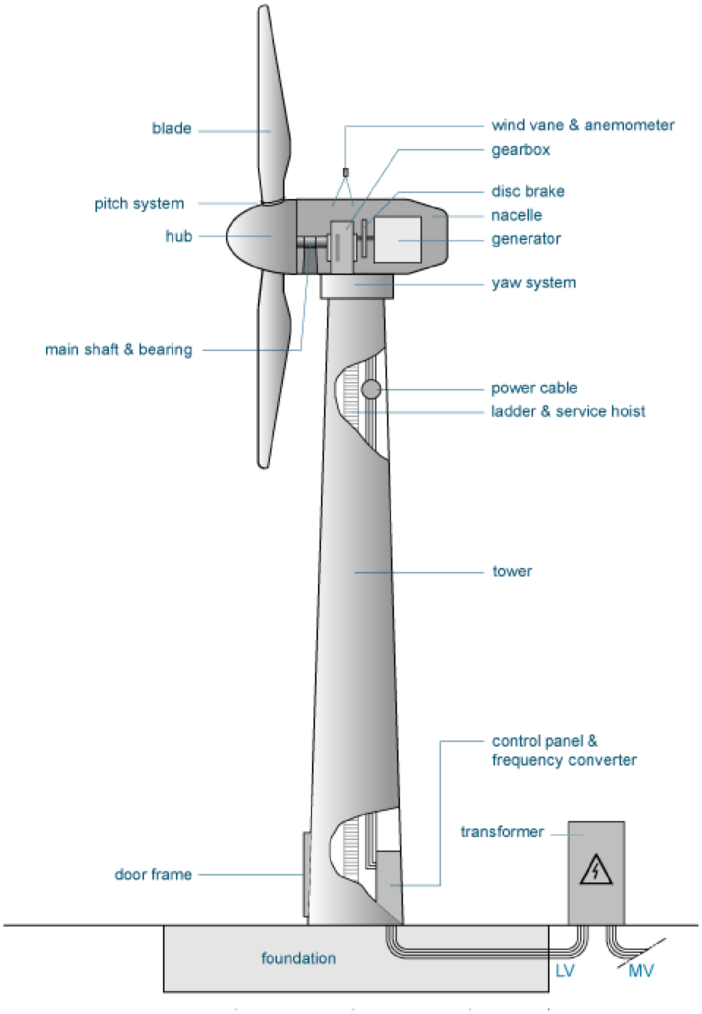

Figure 1.6: A typical wind turbine system [15].

Some short description of the wind turbine components in figure 1.6 [15]:

1. Blades

- Turns or spins as it responds to kinetic energy capture and therefore, rotates the rotor of the generator.

2. Pitch system

- Repositions the blade pitch to control the power produced.

3. Hub/Nacelle

- Houses the components of the generator: gearbox, disc brake, generators, and main shaft and bearings

4. Yaw system

- It rotates the nacelle through its horizontal axis and critically positions the rotor swept area to point at the correct incoming wind speed direction hence improves energy harvest.

5. Power cable

- Transports the generated ac voltage electricity to the frequency converter.

6. Ladder

- Is used by technicians to climb up/down the tower to/from the nacelle.

7. Tower

- Provides the structural support of the nacelle and hub

8. Frequency converter/VSC

- Converts the low frequency voltage to the grid required standard one (50 Hz in South Africa)

9. Transformer

- Steps up the low voltage to a medium voltage level which is then transported to the substation.

The structure of the grid system is connected as *n x m* series –parallel wind turbine interconnections on wind farm. The *n-series* connection of the farm is required to create a voltage high magnitude enough for an HVDC transmission operation. On the other hand, the *m-parallel* branches enable the current to develop in order to produce the projected active power to maintain the main bus bar level, see figure 1.7 [13] below.

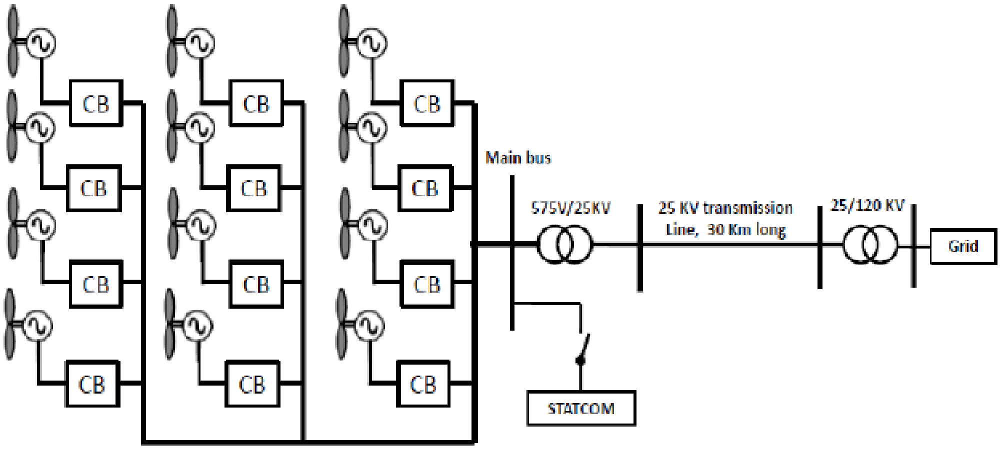

Figure 1.7: Typical wind farm schematic diagram [13].

1.2.2 VSC-HVDC technology

HVDC technology was introduced a way back in time to tackle the submarine power transmission losses. It went on to be further developed and applied in transmitting bulk power over long distances and connecting two different grids having two different frequencies such as the Brazil-Argentina interconnection. The ancient HVDC system employed mercury valves [14]. The valves have been improved since then to thyristor valves and now IGBTs.

The Voltage Source Converter-High Voltage Direct Current (VSC-HVDC) system has been developed recently to provide solutions to the constraints experienced under the classical HVDC. Model: 1) required more reactive power, 2) could not reverse the power flow direction, and 3) was very vulnerable to commutation failures [15]. The VSC-HVDC system's ability to independently control both the reactive and active power flow gave it a superb edge over the classical HVDC [15].

For long time, grids have been realised using AC systems. The extension of the VSC-HVDC system continue to drive change around the ancient grid topologies: A multi-terminal High Voltage Direct Current (MTDC) network has been developed as a DC grid which will be similar to the AC grid [15]. With the demand for electrical energy continuing to rise, and with the power generation stations far away from the demand centres, bulk power transmission would be required. This, therefore, presented the opportunity for the development of DC grids through the MTDC systems.

The VSC-HVDC can be modelled as a synchronous machine with no inertia deriving from the fact that the power control is instantly with no delays. The diodes which are connected anti-parallel to the IGBTs switch valves enable a bidirectional power flow within the VSC without having to change the polarity of the dc-link voltage.

Safety measures have been developed for the MTDC system when selecting the upper and lower voltage limit settings [15]:

1. When a fault or a disturbance occurs on the AC sides, the DC voltage should not experience oscillations.
2. AC voltage support and frequency droop control should be enhanced through MTDC terminal independently controlling the active and reactive power flow.

The dc-link can be implemented using either a cable conductor or an overhead line. For the first time in history, the dc-link has been developed using an overhead line which spans for 970 km long distance in the Caprivi link project between Namibia and Zambia : 951 km +/- 350 kV HVDC transmission line, 300MW monopole HVDC converter [16]. The VSC system here further stabilise the weak networks.

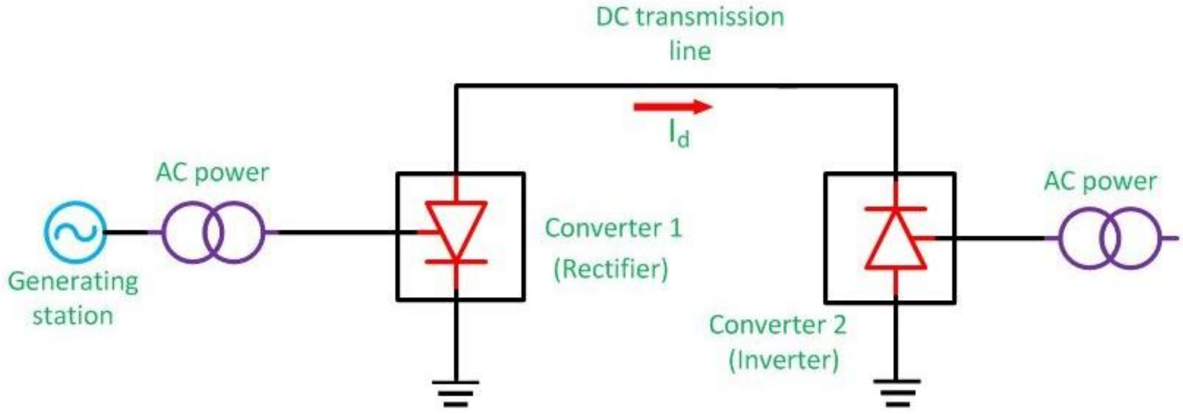

Figure 1.8: Monopolar HVDC link schematic diagram [17]

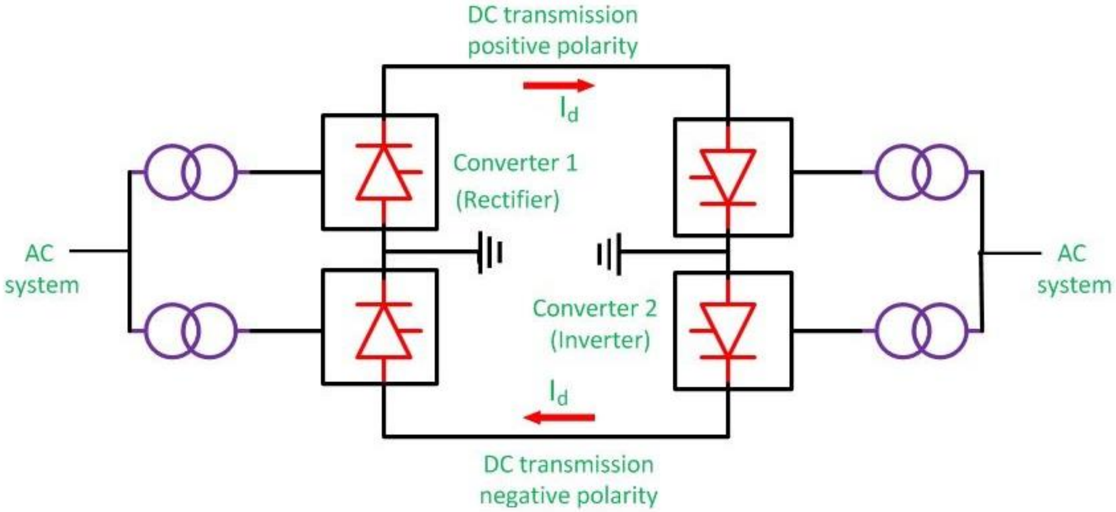

Figure 1.9: Bipolar HVDC link schematic diagram [17]

In this configuration, the monopole converter has one pole energized while the other one is grounded, see figure 1.8. Another arrangement would be a bipolar connection where two identical asymmetric monopoles are connected in parallel, see figure 1.9. One pole is positively energised while the other one is negatively charged [16]. The advantage of this arrangement is that if one pole is lost, the other pole can still supply power to the system even though it would be the half rated full VSC station power. Another type of VSC connection is the symmetrical monopole which employs two conducting conductors and the dc voltages have opposite polarities sourced from splitting the dc capacitor into two equal parts and have the midpoint grounded [17].

1.2.3 Components making up the PMSG based VSC system

1.2.3.1 PMSG components

The turbine and PMSG system is made up of three components: rotor-blade and pitch, drive train and the PMSG as shown in figure 1.10. For an improvement of the simulation speed for the various electrical components, the components are modelled in *dq*-synchronous reference frame [18].

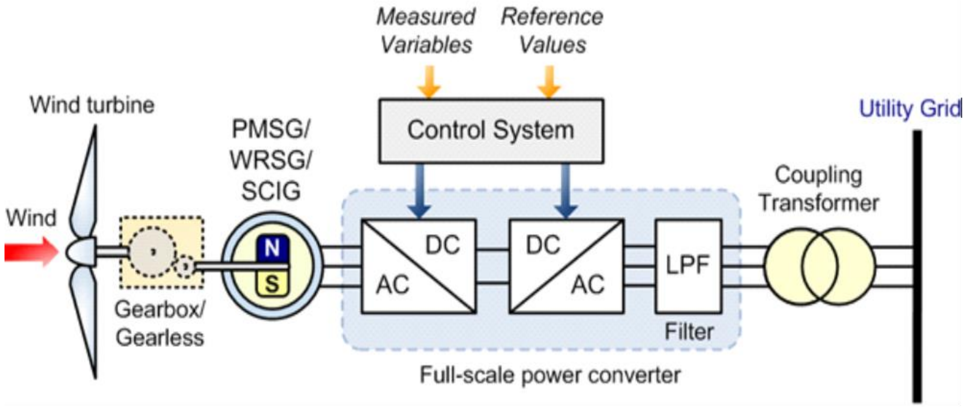

Figure 1.10: A Typical PMSG wind turbine system [18]

The PMSG wind turbine is gaining considerable attention from industry. A direct-driven PMSG reduces the maintenance costs associated with gearbox and reduces the weight of the nacelle. A solid and critical assumption is made in power system analysis that the magnetic flux distribution in the synchronous machine rotor is approximately sinusoidal [19]. Hence the internal voltage E induced in the stator winding due to the permanent magnet flux (ψ_{PM}) is expressed as:

$$|E| = \omega_s \psi_{PM} = 2\pi f_s \psi_{PM} \tag{1.0}$$

where ω_s and f_s are the stator generator speed and frequency respectively.

The rotor speed, n_n (r/min) controls the internal voltage [20].

$$120 f_e = p n_n \tag{1.1}$$

where p is the pole number of the machine and f_e is the electrical frequency.

At no load the internal voltage E (in *abc* reference frame) and the stator voltage U_s (in *abc* reference frame) are equivalent. When a load is connected across the legs of the stator,

$$E = |E_o| \angle \delta^{\circ} \tag{1.2}$$

$$U_s = |U_s| \angle 0^{\circ} \tag{1.3}$$

$$U_s = I_s X_h \tag{1.4}$$

where I_s is the stator current and X_h is the machine reactance, δ is the load angle.

The magnetic field produced by the stator winding is superposed to that of the rotor field [21]. The PMSG characteristic voltage equation expressed in the *dq0*-reference frame are:

$$u_{sd} = R_s i_{sd} - \omega_s \psi_{sq} + \dot{\psi}_{sd} \tag{1.5}$$

$$u_{sq} = R_s i_{sq} + \omega_s \psi_{sd} + \dot{\psi}_{sq} \tag{1.6}$$

With the stator flux components:

$$\psi_{sd} = L_d i_{sd} + \psi_{PM} \tag{1.7}$$

$$\psi_{sq} = L_q i_{sq} \tag{1.8}$$

where u_{sd} and u_{sq} represents *dq0*-componenets of the stator voltages, i_{sd} and i_{sq} represents the *dq*-components of the stator currents, L_d and L_q are the stator inductances and R_s is the stator resistance. At the steady state, the stator transients are negligible, $d\psi_{sd}/dt$ and $d\psi_{sq}/dt$.

The generator electrical torque, if a round-rotor machine is assumed [22], is:

$$\begin{aligned} T_e &= 1.5\,\mathrm{Im}\left[\bar{\psi}_s^* \, \bar{i}_s\right] = 1.5\left[\psi_{sd} i_{sq} - \psi_{sq} i_{sd}\right] \\ T_e &= 1.5\left[\left(L_d - L_q\right) i_{sd} i_{sq} - \psi_{PM} i_{sd}\right] \\ T_e &= 1.5\left[-\psi_{PM} i_{sd}\right] \end{aligned} \tag{1.9}$$

And the power generated by the PMSG is:

$$P = \frac{3}{2}\left(u_{sd} i_{sd} - u_{sq} i_{sq}\right) \tag{1.10}$$

$$Q = \frac{3}{2}\left(u_{sq} i_{sd} - u_{sd} i_{sq}\right) \tag{1.11}$$

If the stator voltage is controlled to the rated value and it is aligned completely with the d-component on the dq0-reference frame such that $U_s = u_{sd}$ as shown in figure 1.11 below, then the stator voltage can be controlled instead of the reactive power.

$$P = \frac{3}{2}\left(u_{sd} i_{sd}\right) \tag{1.12}$$

$$Q = \frac{3}{2}\left(-u_{sd} i_{sq}\right) \tag{1.13}$$

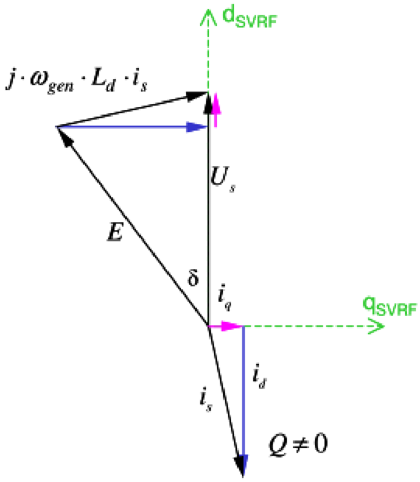

Figure 1.11: Phasor diagram for constant stator voltage in dq-reference frame [20]

1.2.3.2 Wind turbine modelling

Pitch angle control is very important as it enables the blade control of wind turbine and controls the mechanical power extracted from the wind [23]. Maximum power point tracking (MPPT) improves the power extracted from the wind. The two MPPT that are considered are: tip-speed ratio (TSR) control and optimal torque control (OTC) [24-28]. Reference [29, 30] employed small signal model approach to boost the performance of the MPPT control and describe challenges experienced by the generator speed due to the variation of wind speeds. Reference [31] has used the small signal model to improve the output power smoothing capability in TSR and OTC methods.

No additional instrument is added by the OTC method as compared to the TSR one. Further to that, OTC prevents high stress on dc-link capacitor, pitch angle controller, and mechanical system [31]. The OTC method uses the wind speed to set the reference signal for the shaft speed [23, 29, 32, 33]. The mechanical power (P_m) produced by the turbine and the torque (T_m), see figure 1.12 [17], developed is expressed by [34-36]:

$$P_m = \frac{1}{2} C_p \rho A V_W^3 \tag{1.14}$$

$$T_m = \frac{P_m}{\omega_m} = \frac{\frac{1}{2} C_p \rho A V_W^3}{\omega_m} \tag{1.15}$$

where C_p is the turbine power coefficient, ρ is the air density, A is the swept area, R is the radius of the turbine blade, V_w is the velocity of the wind, ω_m is the mechanical angular speed.

The turbine power coefficient depends on the initial blade tip speed ration (λ_0), the tip speed ratio (λ), and blade pitch angle (β) [37-39]:

$$C_p(\lambda,\beta) = k_1\left(k_2\frac{1}{\lambda} - k_3\beta - k_4\beta^{k_5} - k_6\right)\exp\left[\frac{-k_7}{\lambda}\right] \tag{1.16}$$

$$\frac{1}{\lambda} = \frac{1}{\lambda_0 + 0.08\beta} - \frac{0.035}{1+\beta^3} \tag{1.17}$$

And the tip speed ration (λ) is defined as:

$$\lambda = \frac{R\omega_m}{V_w} \tag{1.18}$$

The mechanical angular speed of the turbine is:

$$J\frac{d\omega_m}{dt} = T_e - T_m - B\omega_m \tag{1.19}$$

where J represents the collective inertia of the wind turbine and the rotor, T_e is the generator torque, B is the viscous friction of the rotor.

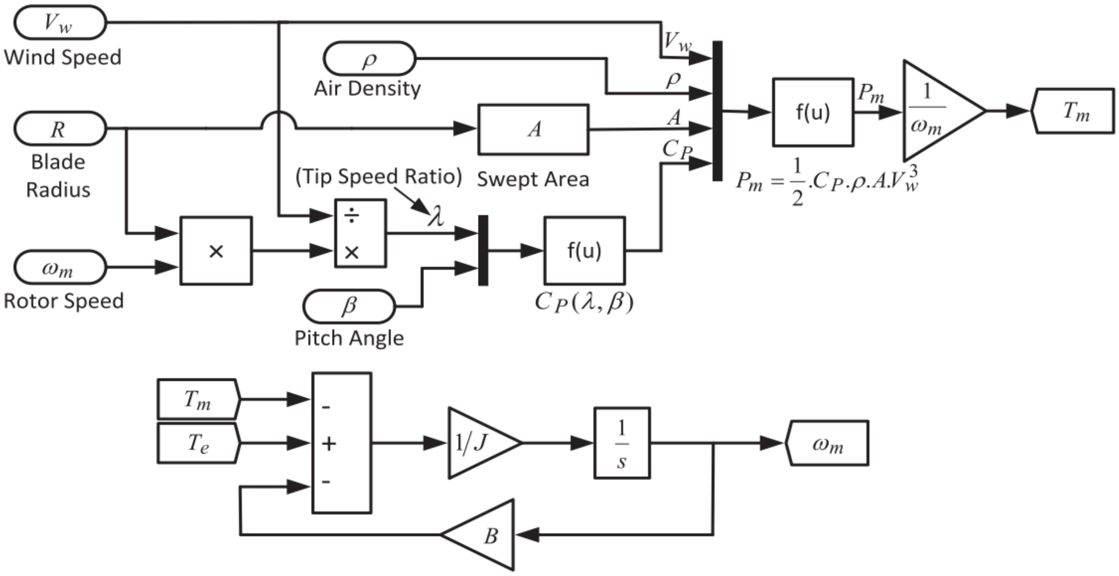

Figure 1.12: The block diagram of the equivalent mechanical angular speed system of the wind turbine [17].

1.2.3.2.1 MPPT algorithms

1.2.3.2.1.1 Tip speed ration (TSR) MPPT algorithm

Maximizing the power extraction from the wind in a TSR achieved by regulating the rotational speed of generator through keeping up the TSR to an optimum value [24, 40, 41]. To extract as much power as possible using the TSR, the wind speed and generator speed are measured continuously to determine the instantaneous optimum TSR (λ_{opt}) of the turbine [42] which can be expressed as:

$$\lambda_{opt} = \frac{R\omega_m^{opt}}{V_w} \tag{1.20}$$

Some drawbacks of the TSR method is the requirement of highly accurate anemometer to supply the readings for the wind speed. This adds costs to the system. Notwithstanding the above setbacks, the TSR method is regarded as highly efficient and can lead to a quick/fast response [31], see figure 1.13 [17] **.** The optimum rotational speed reference signal is obtained from the TSR algorithm. It is then compared with the measured generator signal to produce an error that is corrected by the controller. The MPPT power is being tracked by the generator's mechanical power.

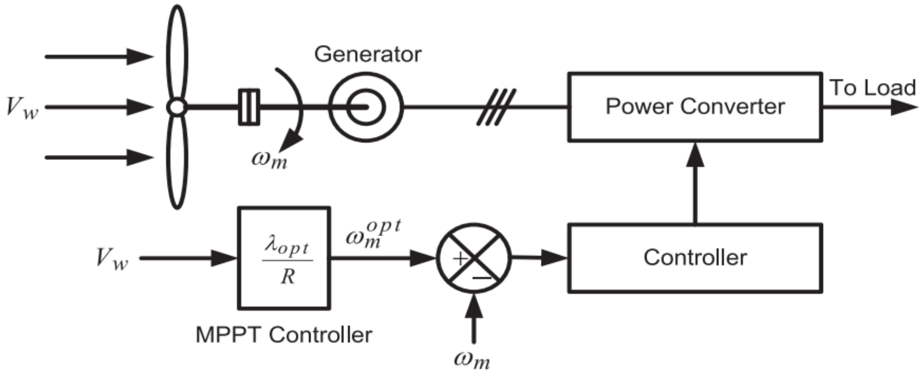

Figure 1.13: The TSR block diagram [17].

1.2.3.2.1.2 Optimal Torque Control (OTC) MPPT algorithm

The torque of the generator is controlled by the OTC algorithm to produce an optimum torque reference curve in accordance with the maximum power of the wind available at a particular wind speed [24, 31, 43].

The optimum mechanical torque of the turbine as a function of λ and ω_m and assuming that the rotor is functioning at optimum, λ_{opt} and C_p max can be defined as:

$$T_m^{opt} = 0.5\rho\pi R^5 \frac{C_p^{\max}}{\lambda_{opt}^3}\omega_m^2 = K_{opt}\omega_m^2 \tag{1.21}$$

And

$$K_{opt} = 0.5\rho\pi R^5 \frac{C_p^{\max}}{\lambda_{opt}^3} \tag{1.22}$$

The characteristics of the optimum curve are shown in figure 1.14 [17] below. The reference signal for the torque is set by the OTC algorithm given in Eq. 1.21 It is then compared with the measured torque to produce a tracking error that the controller rectifies, see figure 1.15 [17] below.

The MPPT efficiency is effectively higher with the OTC method. However, the OTC curve changes as the system ages due to the fact that it is obtained through experimental tests [27, 44, 45]. This, therefore, will reduce the MPPT efficiency.

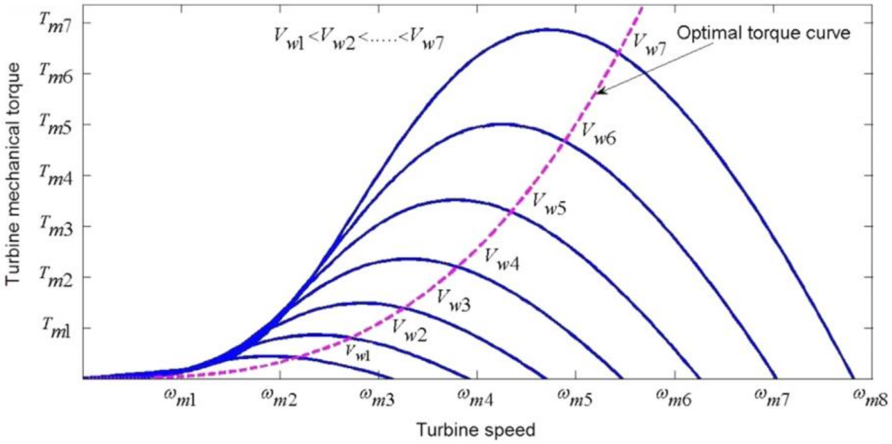

Figure 1.14: The characteristics of the optimum torque curve [17].

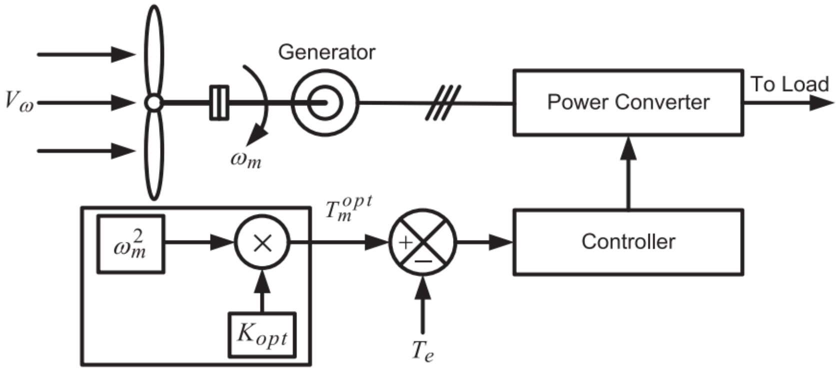

Figure 1.15: The OTC block diagram [17].

1.2.4 Power Converters

The advancements in the development of power electronics over the years enabled the improvement in the integration of renewable energies around the world generally. Power electronics applications date back to the 1980s where thryristor based soft-starters were applied to control a Squirrel Cage Induction Generators (SCIG) system that was synchronised to the grid as shown in figure 1.16 [46]. The main purpose of it was to manage the current surge when the SCIG was started.

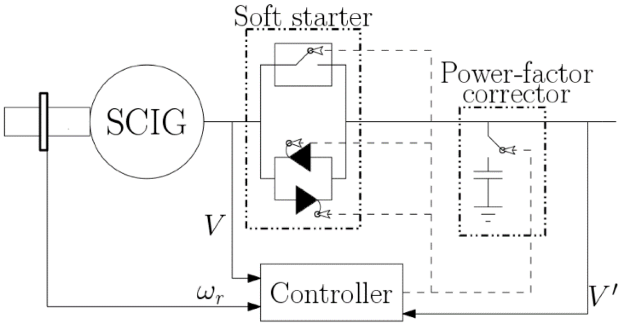

Figure 1.16: The Soft – starter schematic diagram for the SCIG [46].

As time progressed, more development was achieved in the power electronics technology: by 1990, a rotor-resistance was used to control the variable operating speed of the generator, for instance; Wound Rotor Induction Generators (WRIG) [47], see figure 1.17[48].

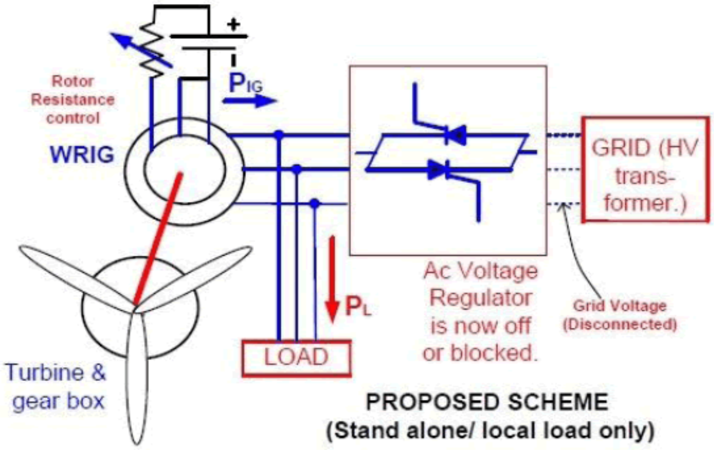

Figure 1.17: The Resistance control system [48].

Recent power electronic technology has played a crucial role in driving large renewable energy (RE) integration to the grid. It forms the backbone of RE. One of the distinct roles of power electronics is the ability to quickly switch on and off when instantly needed. Figures 1.18 to 1.20 show the different application of power converters in industry.

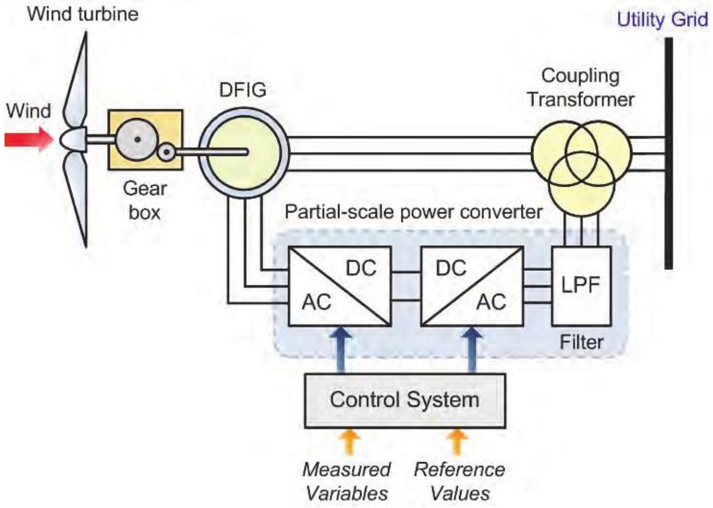

Figure 1.18: DFIG wind turbine schematic diagram [18]

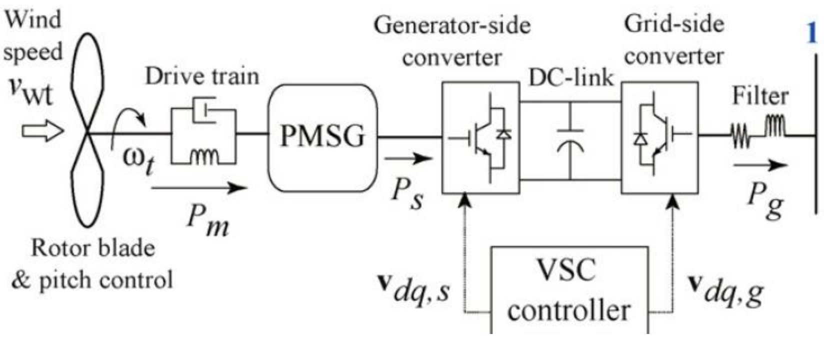

Figure 1.19: A PMSG wind turbine system [49]

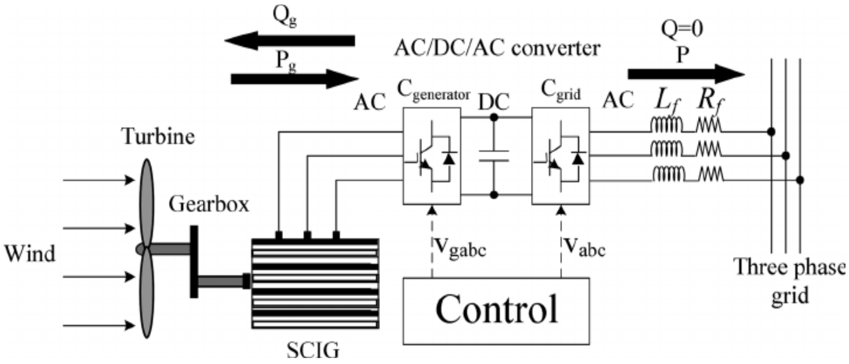

Figure 1.20: A SCIG wind turbine system [50]

Voltage Source Converter is connected back-to-back using the high performing semiconductor devices: IGBTs. It provides full controllability of the instantaneous active and reactive power that is between the wind turbine generator and the grid if employed as a full-scale converter. The conventional two level back-to-back power converters is the engine of wind energy integration. It is deployed at the bottom of the wind turbine structure in most of wind turbines.

1.2.4.1 VSC components

The core equipment of the VSC-based HVDC converter are the converter valves, the converter reactor and the DC capacitors. The capacitors smooth the dc voltage to achieve a ripple free voltage and act as energy storage for the system. Using pulse width modulation (PWM) technology, the DC voltage is converted to an AC voltage by the converter valves and the converter reactor controls the apparent power flow [16, 51]. Wind farms located in the offshore regions have been enabled into the grid by the VSC-HVDC connection due to the flexible active and reactive power control [52]. The components making for a full VSC-HVDC system are shown figure 1.21 [17].

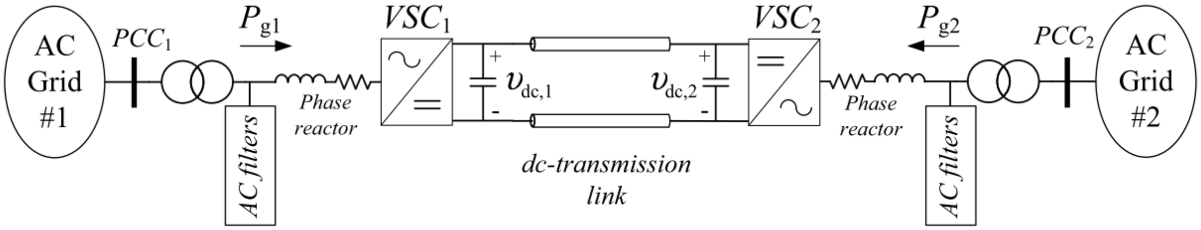

Figure 1.21: A typical VSC-HVDC transmission system [17]

1.2.4.1.1 Coupling Transformer

The voltage from the point of common coupling is then connected to the grid using the coupling transformer. It is stepped up to meet the grid voltage. A three-phase transformer with a tap changer is to limit the injection of third-order harmonics together with its multiples to the main ac system [17] . It is complicated/difficult to design a transformer for an asymmetrical dc-transmission system as the transformer is usually exposed to a dc-offset in the VSC valve-side of ac voltages (the valve that converts dc voltage to ac voltage) [53].

1.2.4.1.2 Phase Reactor

The critical role of the phase reactor is to control the active and reactive power flow within the VSC system. The controlled amount of the active and reactive power depends on the magnitude and phase difference of the induced voltage across the reactor [17].

The reactor together with the coupling transformer also function as filters to block higher harmonic components from the converter’s output current and control the short-circuit currents through the IGBT valves [53]. Typical values of the short-circuit impedance is 0.15 p.u – 0.25 p.u [54, 55].

1.2.4.1.3 AC side filters

Switching on and off the converter values introduces some harmonics in the voltage and current. These harmonics are not needed to the system hence need to be blocked them from reaching the grid. It is important to keep the modulation index m at low values so as to reduce harmonic contents in the VSC voltage and current outputs [17, 53].

1.2.4.1.4 DC capacitor

The critical role played by the dc-capacitors in the VSC system is to keep the voltage ripples very low and keep the dc voltage constant. This is important as the power exchange depends on the dc voltage stability. The capacitor also acts as energy storage of the system: can provide reactive power or consume one. The size of the capacitor (C_{dc}) should be enough to provide smooth voltage and store enough energy. Therefore, the size of the capacitor (C_{dc}) depends on the apparent power (S_n) rating of the VSC, the dc voltage (V_{dc}) across the cap and the capacitor time constant, τ [17, 53, 56, 57]

$$\tau = \frac{C_{dc}V_{dc}^{2}}{2S_{n}} \tag{1.23}$$

1.2.5 Basic switching and modulation

A simple demonstration on how to convert an ac voltage system to a dc voltage is shown in the figure 1.22 a) below [17]. A half-bridge converter is made up of two identical capacitors connected in series. The switches are operated in a complimentary function [17]. Figure 1.22 b) shows the resultant output waveform for the switches [17].

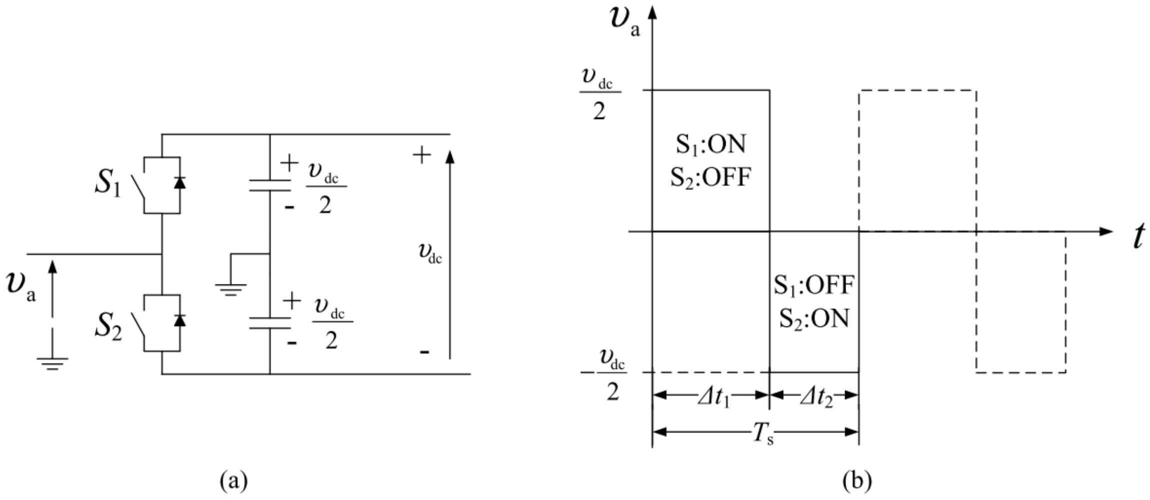

(a) (b)

Figure 1.22: Basic switching; a) Half-bridge converter and b) resultant output waveform [17]

Applying the Fourier series on the output waveform gives:

$$V_a = \frac{V_{a0}}{2} + V_{a1}\sin\left(\omega_0 t + \varphi_1\right) + \sum_{n=2}^{\infty} V_{an}\sin\left(\omega_0 t + \varphi_n\right) \tag{1.24}$$

where V_a is the output voltage, V_{ao} is the dc offset and V_{an} together with ϕ_n are the Fourier coefficients and angles.

Let the duty cycle be 0.5 and then apply again the Fourier series to the output waveform gives:

$$V_a = V_{a1}\sin\left(\omega_0 t + \varphi_1\right) + \sum_{n=2}^{\infty} V_{an}\sin\left(\omega_0 t + \varphi_n\right) \tag{1.25}$$

From Eq. 1.25, the dc offset term, $V_{ao/2}$ has been eliminated.

The terms given by the summer (last term in Eq. 1.25) are the harmonic components contained in the sinusoidal waveform. So the amplitudes of the harmonic waves are:

$$V_{an} = \frac{2V_{dc}}{\pi n}, n = 1,3,5... \tag{1.26}$$

$$V_{an} = 0, n = 0,2,4... \tag{1.27}$$

This result demonstrates the magnitude of the fundamental harmonic component and further shows that keeping the duly cycle fixed at 0.5 value requires more bulk filters to produce a clean voltage waveform. Investigation into finding a better way of triggering the switches was made. Two prominent solutions used extensively in literature are pulse width modulations (PWM), space-vector modulation, and/ or the selective-harmonic elimination [17].

The pulse width modulation method manipulates the index depending on the response needed at the moment. The duty cycle is varied continuously. A sinusoidal pulse width modulation is most applied in the VSC switch triggering controls [17]. It samples the desired reference signal and matches it with the carrier wave to produce the modulation index, see figure 1.23 below [17].

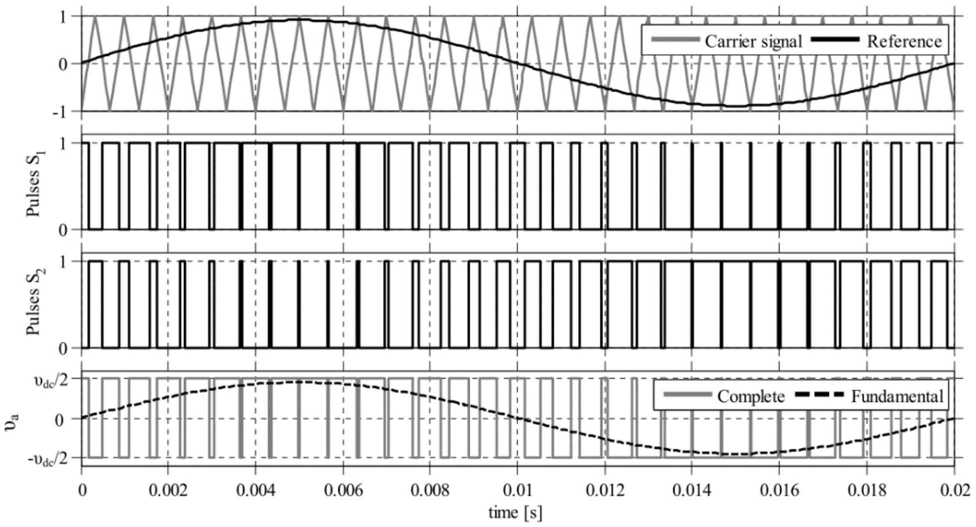

Figure 1.23: The modulation technique using a SPWM [17]

If the VSC output voltage is:

$$V_{abc} = A\sin\left(\omega t + \varphi\right) \quad (1.28)$$

where *A* is the amplitude.

Then the modulation index *m* defined as:

$$m = \frac{A}{A_c} \quad (1.29)$$

where A_c is the amplitude of the carrier wave.

From figure 1.23 above, S_1 is a compliment of S_2 so if S_1 is on, S_2 assumes the off state.

1.2.6 VSC Control

Vector controlling method has been used extensively in industry for the VSC control system: it represents a three-phase ac system in a rotating *dq*-synchronous reference frame [49, 55]. Once in the *dq*-frame, the system can be controlled thereafter changed back to its three phase form.

A general control structure of a VSC control system is demonstrated in figure 1.24 [17] below. It is made up of six control loops: two inner current controllers, AC voltage controller, dc-link voltage controller, reactive controller and active power controller.

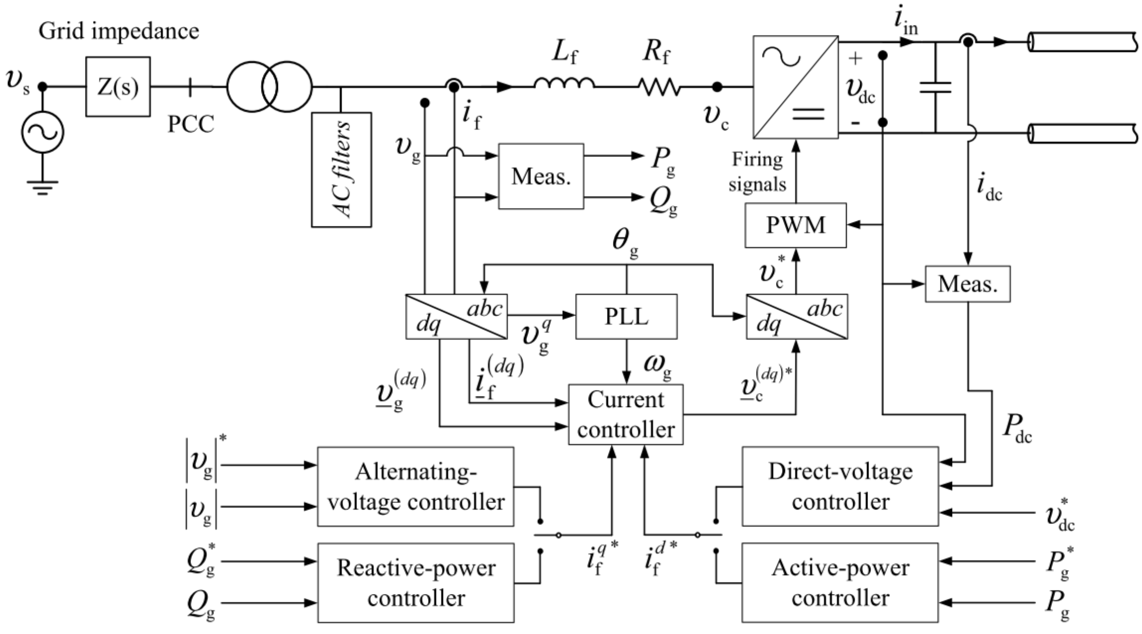

Figure 1.24: The summary control system for a VSC [17]

The outer controller sets the current loop reference signals, $i_f^{d}*$ and $i_f^{q}*$, which are then compared with the measured current values from the grid. The resultant signal is sent through a PI-ontroller which adjusts it. Thereafter, the signals are sent to a *dq*-*abc* signals that are modulated and are imported to the PWM block. The transformation block use the phase locked loop (PLL) to perfectly synchronise the *dq*-reference frame to the *abc* coordinated frame.

1.2.6.1 Inner Current Control

The inner current controller forms the heart engine of the VSC control system. In Figure 1.25 [58], V is the stator voltage from the PMSG system and U is the converter voltage at the foot of the VSC. I_{as},I_{bs},I_{cs} are the currents from the source flowing through the system. δ is the load angle. L_s and R_s represents the PMSG and transmission parameters. The dc-link voltage is represented by U_{dc} and i_{dc} and i_L are the currents of the HVDC line. C is the dc capacitor.

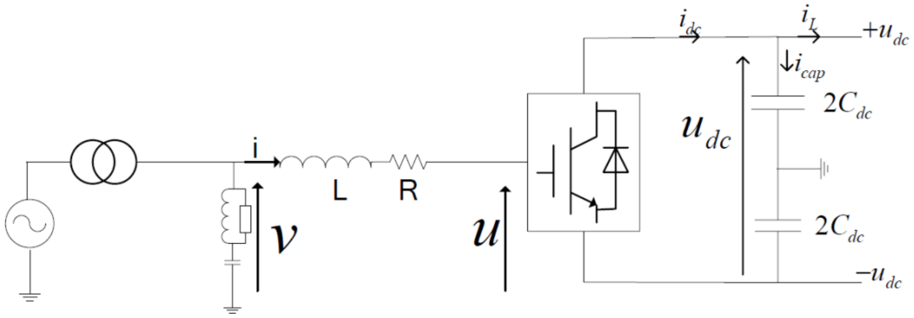

Figure 1.25: Basic structure of VSC [58].

1.2.6.1.1 Machine side Converter modelling

Applying a Kirchhoff's law in the figure 1.25 [59] above and taking the three phases as a balanced in the network, the following equations are derived from the system [60]:

$$\begin{bmatrix} V_{as} \\ V_{bs} \\ V_{cs} \end{bmatrix} = L_s \frac{d}{dt} \begin{bmatrix} i_{as} \\ i_{bs} \\ i_{cs} \end{bmatrix} + R_s \begin{bmatrix} i_{as} \\ i_{bs} \\ i_{cs} \end{bmatrix} + \begin{bmatrix} U_{as} \\ U_{bs} \\ U_{cs} \end{bmatrix} \tag{1.30}$$

The Eq. (1.30) in vector form is as follows:

$$V_{abc_s} = L_s \frac{di_{abc_s}}{dt} + R_s i_{abc_s} + U_{abc_s} \tag{1.31}$$

Rearranging Eq. (1.31) gives

$$L_s \frac{di_{abc_s}}{dt} = -R_s i_{abc_s} + \left(V_{abc_s} - U_{abc_s}\right) \tag{1.32}$$

Park transformation matrix P and its inverse P^{-1} are given below. And ω_s is the stator frequency.

$$P = \frac{2}{3} \begin{bmatrix} \cos(\omega_s t) & \cos\left(\omega_s t - \frac{2\pi}{3}\right) & \cos\left(\omega_s t + \frac{2\pi}{3}\right) \\ \sin(\omega_s t) & \sin\left(\omega_s t - \frac{2\pi}{3}\right) & \sin\left(\omega_s t - \frac{2\pi}{3}\right) \\ \tfrac{1}{2} & \tfrac{1}{2} & \tfrac{1}{2} \end{bmatrix} \tag{1.33}$$

$$P^{-1} = \begin{bmatrix} \cos(\omega_s t) & -\sin(\omega_s t) & 1 \\ \cos\left(\omega_s t - \frac{2\pi}{3}\right) & -\sin\left(\omega_s t - \frac{2\pi}{3}\right) & 1 \\ \cos\left(\omega_s t + \frac{2\pi}{3}\right) & -\sin\left(\omega_s t + \frac{2\pi}{3}\right) & 1 \end{bmatrix} \tag{1.34}$$

Applying a Park transformation to Eq. (1.32) gives Eq. (1.35) in the vector form.

$$\frac{di_{dq0_s}}{dt} = -\frac{R_s}{L_s} i_{dq0_s} + \frac{1}{L_s}\left(V_{dq0_s} - U_{dq0_s}\right) - P\frac{dP^{-1}}{dt} I_{dq0_s} \tag{1.35}$$

In a synchronous rotating reference frame, there is no zero sequence component in the 3 phase balanced system hence Eq. (1.35) becomes Eq. (1.36):

$$s\begin{bmatrix} i_{ds} \\ i_{qs} \end{bmatrix} = \frac{1}{L_s}\begin{bmatrix} -R_s & \omega_s L_s \\ -\omega_s L_s & -R_s \end{bmatrix}\begin{bmatrix} i_{ds} \\ i_{qs} \end{bmatrix} + \frac{1}{L_s}\begin{bmatrix} V_{ds} \\ V_{qs} \end{bmatrix} - \frac{1}{L_s}\begin{bmatrix} U_{ds} \\ U_{qs} \end{bmatrix} \tag{1.36}$$

where s is the Laplace operator, V_{ds} and V_{qs} are the components of the stator voltages in the dq-axis frame. I_{ds} and I_{qs} are the components of the line currents in the dq-axis frame, U_{ds} and U_{qs} are the components of the converter input voltages.

If the stator voltage is assumed to be in complete synchronism with the d-axis, then V_{ds} is equal to V_{abcs} and V_{qs} is equal to 0. Eq. (1.36) therefore becomes Eq. (1.37).

$$s\begin{bmatrix} i_{ds} \\ i_{qs} \end{bmatrix} = \frac{1}{L}\begin{bmatrix} -R_s & \omega_s L_s \\ -\omega_s L_s & -R_s \end{bmatrix}\begin{bmatrix} i_{ds} \\ i_{qs} \end{bmatrix} + \frac{1}{L_s}\begin{bmatrix} V_{ds} \\ 0 \end{bmatrix} - \frac{1}{L_s}\begin{bmatrix} U_{ds} \\ 0 \end{bmatrix} \tag{1.37}$$

The vector form of Eq. (1.37) is given by Eq. (1.38) and (1.39) below:

$$V_{ds} = R_s i_{ds} + sL_s i_{ds} - \omega_s L_s i_{qs} + U_{ds} \tag{1.38}$$

$$V_{qs} = R_s i_{qs} + sL_s i_{qs} + \omega_s L_s i_{ds} \tag{1.39}$$

1.2.6.1.2 Grid side Converter modelling

The grid side converter (GSC) is modelled differently from the machine side one even though there are symmetrically; the power flow is different in direction both sides. So that has to be taken into consideration when modelling the GSC for the control system. U_{abcg} is the grid voltage from the VSC system and V_{abcg} is the grid voltage at the point of common coupling (PCC). I_{ag},I_{bg},I_{cg} are the currents from the VSC source flowing through the grid system. δ is the phase angle. L_g and R_g represent the transmission parameters. The dc-link voltage is represented by U_{dc} and C is the dc capacitor. Figure 1.26 [59] shows a typical GSC system even though the labelling is different, but the same logic remains the same throughout.

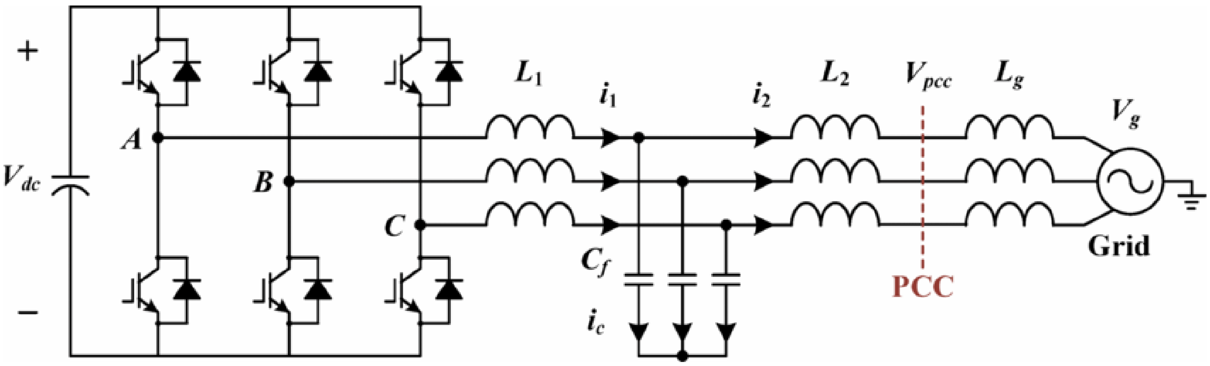

Figure 1.26: A typical Grid Side Converter system [59]

Applying a Kirchhoff’s law in the figure 1.26 [59] above and taking the three phases as a balanced in the network, the following equations are derived from the system [60]:

$$\begin{bmatrix} U_{ag} \\ U_{bg} \\ U_{cg} \end{bmatrix} = L_g \frac{d}{dt} \begin{bmatrix} i_{ag} \\ i_{bg} \\ i_{cg} \end{bmatrix} + R_g \begin{bmatrix} i_{ag} \\ i_{bg} \\ i_{cg} \end{bmatrix} + \begin{bmatrix} V_{ag} \\ V_{bg} \\ V_{cg} \end{bmatrix} \tag{1.40}$$

The Eq. (1.40) in vector form is as follows:

$$U_{abc_g} = L_g \frac{di_{abc_g}}{dt} + Ri_{abc_g} + V_{abc_g} \tag{1.41}$$

Where

$$U_{abc_g} = \frac{mV_{dc}}{2} \begin{bmatrix} \sin\left(\omega_g t + \delta\right) \\ \sin\left(\omega_g t + \delta - 120^o\right) \\ \sin\left(\omega_g t + \delta + 120^o\right) \end{bmatrix} \tag{1.42}$$

M and δ are respectively the modulation index and the initial phase angle of modulation wave. The following Eq. (1.43) is obtained by transforming Eq. (1.41)

$$L_g \frac{di_{abc_g}}{dt} = -R_g i_{abc_g} + \left(U_{abc_g} - V_{abc_g}\right) \tag{1.43}$$

Park transformation matrix P and P^{-1} are given below. And ω is the angular frequency of system.

$$P = \frac{2}{3} \begin{bmatrix} \cos\left(\omega_g t\right) & \cos\left(\omega_g t - \frac{2\pi}{3}\right) & \cos\left(\omega_g t + \frac{2\pi}{3}\right) \\ \sin\left(\omega_g t\right) & \sin\left(\omega_g t - \frac{2\pi}{3}\right) & \sin\left(\omega_g t - \frac{2\pi}{3}\right) \\ 1/2 & 1/2 & 1/2 \end{bmatrix} \tag{1.44}$$

$$P^{-1}=\begin{bmatrix}\cos\left(\omega_g t\right) & -\sin\left(\omega_g t\right) & 1\\ \cos\left(\omega_g t-\frac{2\pi}{3}\right) & -\sin\left(\omega_g t-\frac{2\pi}{3}\right) & 1\\ \cos\left(\omega_g t+\frac{2\pi}{3}\right) & -\sin\left(\omega_g t+\frac{2\pi}{3}\right) & 1\end{bmatrix} \tag{1.45}$$

Applying a Park transformation to Eq. (1.43) gives Eq. (1.46) in the vector form.

$$\frac{di_{dq0_g}}{dt}=-\frac{R_g}{L_g}i_{dq0_g}-\frac{1}{L_g}\left(V_{dq0_g}-U_{dq0_g}\right)-P\frac{dP^{-1}}{dt}I_{dq0_g} \tag{1.46}$$

In a synchronous rotating reference frame, there is no zero sequence component in the 3 phase balanced system hence Eq. (1.46) becomes equation (1.47):

$$s\begin{bmatrix}i_{dg}\\ i_{qg}\end{bmatrix}=\frac{1}{L_g}\begin{bmatrix}-R_g & \omega_g L_g\\ -\omega_g L_g & -R_g\end{bmatrix}\begin{bmatrix}i_{dg}\\ i_{qg}\end{bmatrix}+\frac{1}{L_g}\begin{bmatrix}U_{dg}\\ U_{qg}\end{bmatrix}-\frac{1}{L_g}\begin{bmatrix}V_{dg}\\ V_{qg}\end{bmatrix} \tag{1.47}$$

where s is the Laplace operator, V_{dg} and V_{qg} are the components of the grid voltages and U_{dg} and U_{qg} are the components of the converter input voltages in the *dq*-axis frame respectively. I_{dg} and I_{qg} are the components of the line currents in the *dq*-axis frame.

If the grid voltage is assumed to be in complete synchronism with the d-axis, then U_{ds} is equal to U_{abcs} and U_{qs} is equal to 0. Eq. (1.47) therefore becomes Eq. (1.48).

$$s\begin{bmatrix}i_{dg}\\ i_{qg}\end{bmatrix}=\frac{1}{L_g}\begin{bmatrix}-R_g & \omega_g L_g\\ -\omega_g L_g & -R_g\end{bmatrix}\begin{bmatrix}i_{dg}\\ i_{qg}\end{bmatrix}+\frac{1}{L_g}\begin{bmatrix}V_{dg}\\ 0\end{bmatrix}-\frac{1}{L_g}\begin{bmatrix}U_{dg}\\ 0\end{bmatrix} \tag{1.48}$$

The vector form of Eq. (1.48) is given by Eq. (1.49) and (1.50) below:

$$V_{dg}=R_g i_{dg}+sL_g i_{dg}-\omega_g L_g i_{qg}+U_{dg} \tag{1.49}$$

$$V_{qg}=R_g i_{qg}+sL_g i_{qg}+\omega_g L_g i_{dg} \tag{1.50}$$

The decoupling approach given by [59] is that manipulating Eq. (1.51), Eq. (1.52), Eq. (1.53) gives the decoupled systems in Eq. (1.54) and Eq. (1.55). This according to [59] gets the cross coupling terms cancelled out and an independent control in d and q axis is achieved. Moreover, the equations in d and q axis show the same form.

$$V_{dg} - U_{dg} = R_g i_{dg} + sL_g i_{dg} - \omega_g L_g i_{qg} \tag{1.51}$$

$$V_{qg} - U_{qg} = R_g i_{qg} + sL_g i_{qg} + \omega_g L_g i_{dg} \tag{1.52}$$

$$U_{dq_g}(s) = \left(i_{dq_g}^{ref} - i_{dq_g}(s)\right) H(s) \tag{1.53}$$

Where, *H(s)* is the regulator term.

$$V_{dg} = L_g \frac{di_{dg}}{dt} + R_g i_{dg} \tag{1.54}$$

$$V_{qg} = L_g \frac{di_{qg}}{dt} + R_g i_{qg} \tag{1.55}$$

It is good to note that the explanation is not very clear on how the decoupling is achieved. This thesis proposes a decoupling approach using feedback design which is discussed in detail in subsequent chapters.

1.2.6.2 Phase Locked Loop (PLL)

The function of a PLL is to calculate the angle of rotation for the measured quantities: voltage and current. This angle is used in the transformation block diagram from the abc reference frame. Figure 1.27 shows the block diagram of the PLL [17]. The measured voltage, $V_g(abc)$ is first projected to the synchronous reference frame as shown in figure 1.28 then the q-component of the voltage is sent to the PI controller to be modified and then a corrected signal, $\Delta\omega$ is added to the frequency term of the ac system, ω_g to produce the resultant ω_g. The angle of rotation is obtained by integrating the resultant frequency ω_g. The bandwidth of the closed loop is selected in the range, 3 – 5 Hz [61-63].

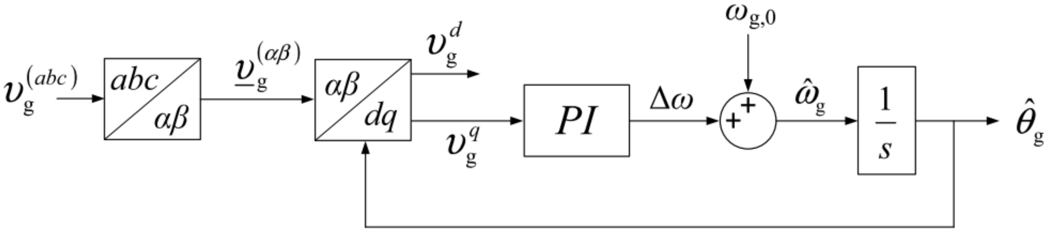

Figure 1.27 The block diagram of the PLL [17].

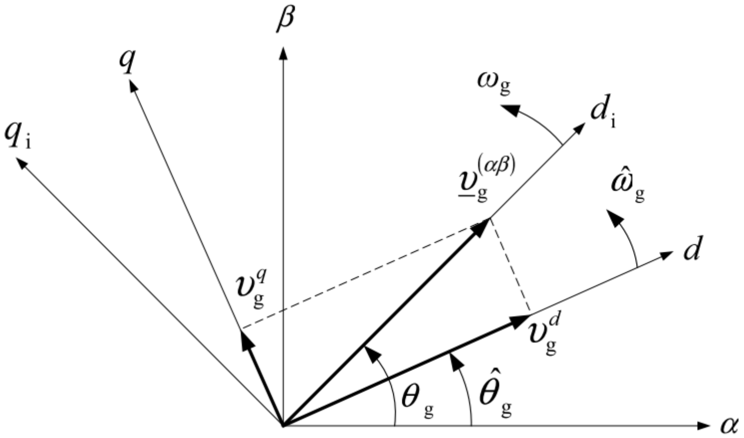

Figure 1.28: The measured voltage projected to the synchronous reference frame [17].

1.2.6.3 Direct-Voltage control

The function of the DC voltage controller is to keep the link dc voltage of the VSC constant all the time. A block diagram is shown below in figure 1.29. The energy stored in the dc capacitor is [17]:

$$\frac{1}{2}C_{dc}\frac{dW}{dt}=P_{dc,in}-P_{dc} \tag{1.56}$$

where C_{dc} is the capacitance, W is the energy stored in the cap, $P_{dc,in}$ and P_{dc} are the powers that flow in the dc side.

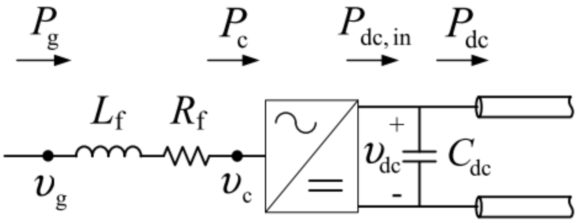

Figure 1.29: A single line block diagram for a VSC [17].

If the power passing through the dc-side is assumed to be lossless and the dc voltage is kept constant then the active power from the ac side should be equal to the power passing through the dc-side:

$$P_g \approx P_c \approx P_{dc,in} \tag{1.57}$$

So this means that the capacitor receives the power from the grid to keep it charged and then passes it to the other side of the converter. If the assumption that the capacitor remains fully charged across the period, then [15, 47, 64]

$$I_{dc}=I_{cap} \tag{1.58}$$

$$C\frac{dV_{dc}}{dt} = I_{dc} \tag{1.59}$$

Therefore, the transfer function of the dc dynamics is given by:

$$sCV_{dc} = I_{dc} \tag{1.60}$$

$$\frac{V_{dc}}{I_{dc}} = \frac{1}{sC} \tag{1.61}$$

1.2.6.4 Active Power control

The power injected to the ac side from the VSC is controlled to the desired value by the active power controller as shown in figure 1.30 [15, 47, 64].

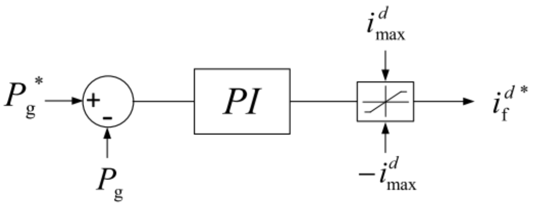

Figure 1.30: A block diagram for active power controller [15, 47, 64].

The measured power P_g from the point of common coupling is compared to the reference value. Then the difference signal is then sent to the PI-controller where it is corrected and sent out to the inner controller as a current reference signal for the d-component.

1.2.6.5 Reactive Power controller

The VSC is capable of consuming or supplying the reactive power. What is most interesting about the VSC is that the reactive power from one side of the converter is not passed to the other side of the converter. The reactive power is sourced from capacitor and helps in supporting the ac voltage when required such as during ac faults on the line. The reactive power controller controls the reactive power injected to the grid by the VSC [3, 8]. The reference reactive power is set to zero and the measured value from the PCC is compared to the reference value then the difference is sent to the PI-controller which then corrects it and set the corrected signal to the inner current controller q-component see figure 1.31 below [17].

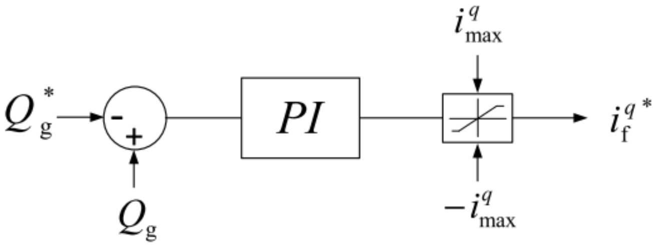

Figure 1.31: The block diagram of the reactive power control system [17].

1.2.6.6 AC-voltage control

The VSC also plays a vital role in helping stabilise weak networks as they are characterised by very large grid impedances. The AC voltage controller needs to keep the voltage stable to the required value. It takes the difference of the measured value and compares it to the reference one [15, 47, 64]. The output difference is then sent to the PI-controller which corrects it. Once corrected, it then serves as a reference signal for the inner current loop, see figure 1.32 [17].

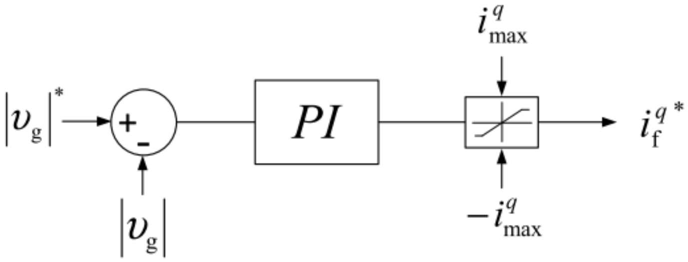

Figure 1.32: The block diagram of the AC voltage control system block diagram [17].

CHAPTER 2: WIND TURBINE AND PMSG CONTROL MODELLING

This chapter introduces the detailed modeling of the wind turbine and PMSG systems.

2.1 Wind Aerodynamic Model

Wind flow is harnessed in the renewable energy industry to generate the mechanical power needed to turn the turbines. Wind flow carries kinetic energy as it drifts in space as shown in figure 2.1 [65] below. Wind is made up of air particles generally which are diverse in nature: mostly nitrogen and oxygen, the other gases make up to 1% of the remaining space including water vapor and carbon dioxide.

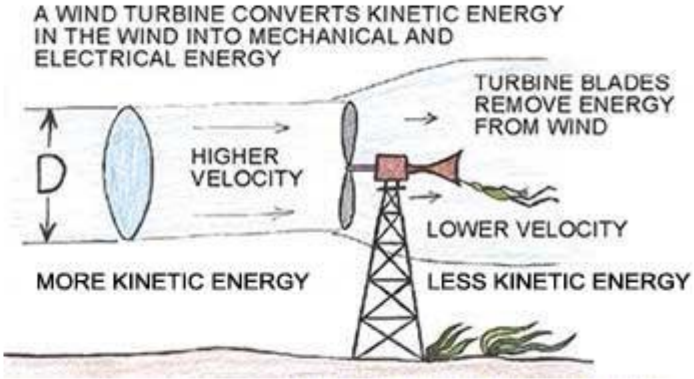

Figure 2.1: Typical wind flow system representation [65]

Assuming that *m* (m/s) represents the total mass of the particles colliding with the blades and v_w (m/s) represents the speed at which the particles flow, the air’s kinetic energy, *E* , is expressed as:

$$E = \frac{1}{2} m v_w^2 \tag{2.1}$$

But the total mass, *m* depends on the quantity of particles at that moment flowing in the direction of the wind turbine blades so the rate of change of mass, $\dot{m}$ (kg/s) drives the kinetic energy system. Hence:

$$\dot{E} = \frac{1}{2} \dot{m} v_w^2 \tag{2.2}$$

But,

$$\dot{m} = \rho \mathrm{A} v_w \tag{2.3}$$

$$\mathrm{A} = \pi r^2 \tag{2.4}$$

Where the variables computed are: ρ for the density of air (kg/m^3), A for the area covered by the wind turbine blades (m^3), and r is the length of each wind turbine blade (m).

Therefore, the rate of change of the kinetic energy is:

$$\dot{E} = \frac{1}{2}\rho\pi r^2 v_w^3 \tag{2.5}$$

which gives the power stored in the wind flow. Varying the length of the blades in increments of two, for instance can greatly increase the power captured from the wind by a quadruple factor. A solid observation can be derived from the relationship of power and speed: an increase in wind speed can harvest more energy from the wind. This maybe the genesis drive for variable wind turbines development.

The complete instantaneous wind power, P_i is:

$$P_i = \frac{1}{2}\left[\left(2mv_w\dot{v}_w\right) + \left(\rho\pi r^2 v_w^3\right)\right] \tag{2.6}$$

Where,

$$m = \int \rho \mathrm{A} v_w dt \tag{2.7}$$

Taking an integral of the mass flow rate gives the instantaneous mass, *m*. The first term bracketed in Eq. 2.6 carries important information for research drive. It gives that keeping the wind velocity oscillating increases the harvested power output as compared to when the wind velocity is constant.

The kinetic energy stored in the air particles is not fully captured by the turbine blades – some of it is retained by the air particles after colliding with the blades as shown in figure 2.1 and figure 2.2 [47]. Betz law which is explained in detail by [66], summarily states that no machine can harvest exactly 100% of the power stored in the wind system – the maximum that can be extracted from the wind system is 59.3%.

Hence the power, $P_{turbine}$ extracted from the wind in relation to the power stored in the wind system, P_{wind} is:

$$P_{turbine} = C_p P_{wind} \tag{2.8}$$

Where the ratio of turbine power, $P_{turbine}$ to wind power, P_{wind} gives the power coefficient C_p (dimensionless)

The power coefficient is a function of a blade angle, a rotor tip speed ratio, mechanical speed and the ratio of the rotor blade length to the wind velocity as shown in Eq. 2.9 [38, 39, 67]

$$C_p(\lambda_i,\beta) = k_1(k_2\frac{1}{\lambda_i} - k_3\beta - k_4\beta^{k_5} - k_6)e^{-k_7\frac{1}{\lambda_i}} \tag{2.9}$$

where,

$$\frac{1}{\lambda_i} = \frac{1}{\lambda + 0.08\beta} - \frac{0.035}{1+\beta^3} \tag{2.10}$$

and,

$$\lambda = \frac{\omega_m r}{V_w} \tag{2.11}$$

The type of wind machine controls the selection of the coefficient values for (k_1-k_7). For instance, a variable speed wind turbine has approximated values for the coefficients as $k_1 = 0.73,\ k_2 = 151,\ k_3 = 0.58,\ k_4 = 0.002,$ $k_5 = 2.14,\ k_6 = 13.2,\ k_7 = 18.4$ [67-69]. ω_m refers to the mechanical angular speed.

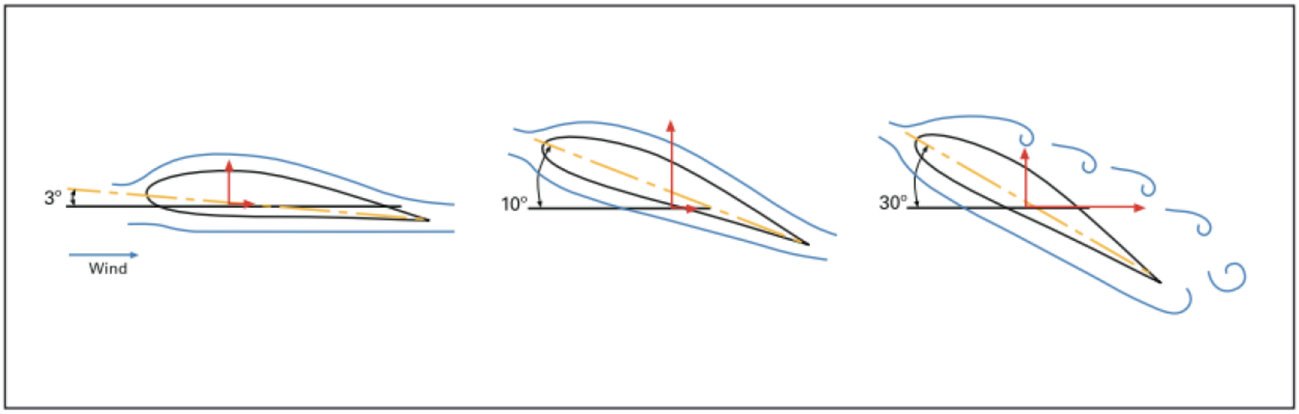

Figure 2.2: The schematic diagram for the blade angle for the wind turbine [47].

The schematic diagram above shows how the wind velocity collides with the turbine blades. The blade angle refers to the axis rotation of orientation for the blade and the wind velocity. Using advanced turbine control technology, the blade angle is varied to control the power harnessed from the wind. For a wind speed below the rated speed, the blade angle is usually modified to angle closer to the horizontal line having 3% as shown above yielding more power capture. Equation 2.12 below shows the inverse proportional relationship between $P_{turbine}$ and $C_p(\lambda_i,\beta)$. As the blade angle decreases due to lower speed for instance, it increases the power captured from the wind hence improves efficiency of the system. For high wind speeds, the turbine control technology slights the blade angle to high in degrees so as to reduce the power captured from the wind if it exceeds the rated one. This helps protect the equipment and the turbine structure from any damage that can translate to high costs to fix.

As it can be derived from Equation 2.8, the maximum power extracted depends on successfully maintaining the operational points of the coefficient factor to its maximum value, $C_p^{\max}(\lambda_i, \beta)$ and varying accordingly the rotor speed. The turbine output power depends on the corresponding turbine speed, see figure 2.3 below [36, 70, 71]. The maximum power extracted from the wind is usually 13m/s for a 2MW rated wind turbine system corresponding to its rated mechanical speed.

The power's empirical formula is given by:

$$P_{turbine} = \frac{1}{2}\rho\pi r^2 v_w^3 C_p(\lambda_i, \beta) \tag{2.12}$$

And the turbines' mechanical torque is:

$$T_{turbine} = \omega_m P_{turbine} \tag{2.13}$$

$$T_{turbine} = \frac{1}{2}\frac{\rho\pi r^2 v_w^3 C_p(\lambda_i, \beta)}{\omega_m} \tag{2.14}$$

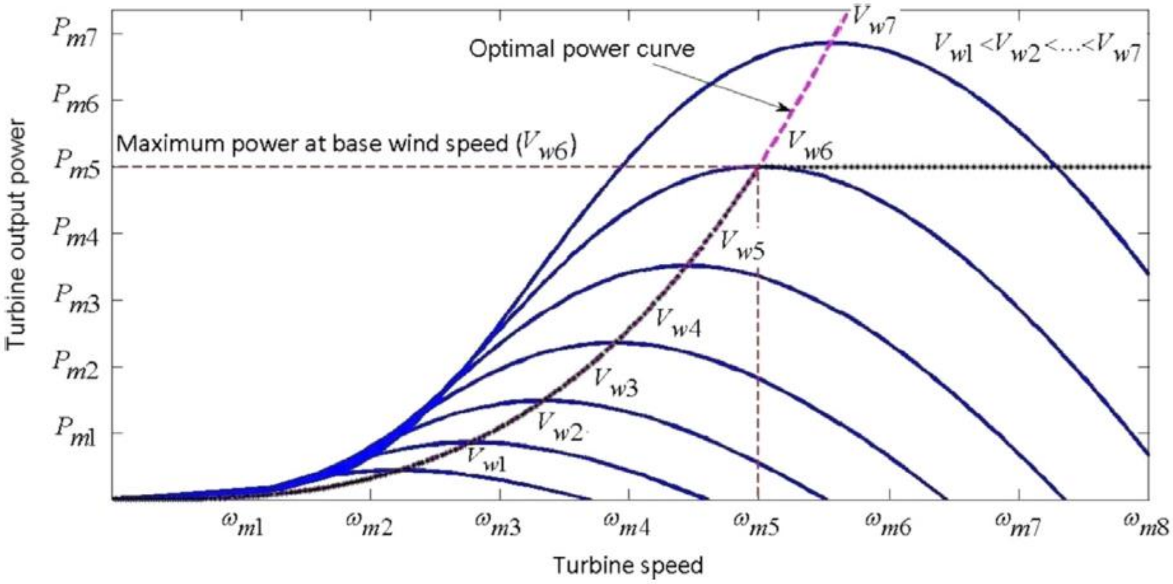

Figure 2.3: The characteristic behaviour of the power curve [36, 70, 71].

2.2 Wind Mechanical model

A PMSG wind turbine with multipole is a preferred generator for a direct driven system. The high pole pairs in the generator has distinct advantages: 1.) the generator inertia increases [20], 2.) The generator's effective shaft stiffness decreases[72, 73], 3.) For a certain electrical angle, the corresponding mechanical angle is much smaller as is with another generator having small pole pairs[21]. The electrical system connected to a generator with multipole usually have a strong effect when a torsional twist occurs in the shaft therefore a detailed shaft model is required [72], see figure 2.4 [20].

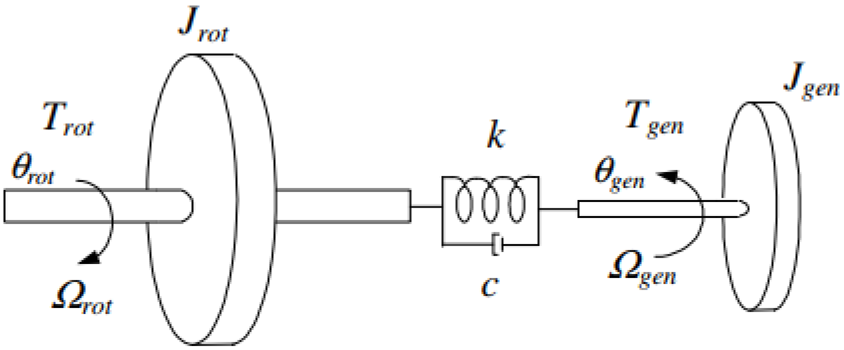

Figure 2.4: The shaft system model [20].

The two-mass modelling of the shaft is crucial in that it gives the information about oscillation that can be triggered by wind gusts. The model is made up of a spring, k and a damper, c and the two masses represent the turbine inertia J_{rot} and the PMSG inertia J_{gen} [20, 21]. The oscillations' frequency is sometimes referred to as free-free frequency:

$$f_{osc} = \frac{1}{2\pi} . \sqrt{\frac{k}{J_{eq}}} \tag{2.15}$$

where the total equivalent mass of inertia is represented by J_{eq}, expressed as:

$$J_{eq} = \frac{J_{rot} J_{gen}}{J_{rot} + J_{gen}} \tag{2.16}$$

and the shaft's resultant stiffness:

$$K_s = \frac{k}{S_n} . \frac{\omega_m}{p} \tag{2.17}$$

completes the shaft model. The term K_s refers to the resultant stiffness, k is the shaft stiffness, S_n is the rated apparent power for the PMSG and p is the number of pole pairs. K_s has an inverse proportional relationship with the p term so when the number of pole pairs increase the resultant stiffness decreases.

2.3 Pitch Angle model

The main function of the pitch angle is to control the speed of the generator to its reference. This control helps to regulate the generator speed as the wind speed may vary to a high value. The power being harnessed is controlled via blade pitching technology. As shown in figure 2.5 [74], the speed controller is implemented using a PI –controller. It takes a reference value ω_{ref} and checks it up with the measured speed ω_{meas}. If the measured speed is higher than the reference value, a signal is sent via a value of the angle θ_m to the control equipment to adjust the angle value up. And similarly, if the measured speed is low, a signal is sent to the equipment which reduces the pitch angle. When the measured value equals the reference the value of the angle is not changed. The pitch system has a servomechanism model that implements the time constant T_{servo}, the rate of change limit ($\pm 10\deg/ s$) and the pitch angle limit (0 to 30 deg) [74]. The power is controlled indirectly as it's tied to the speed hence it is also controlled and limited to its rated value.

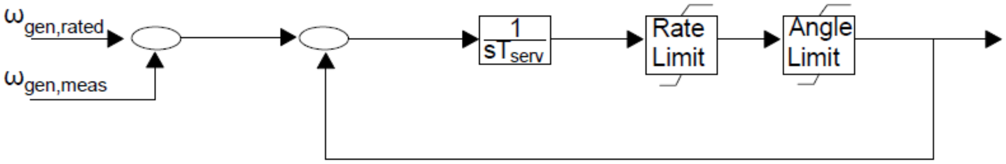

Figure 2.5: PI-controller for the speed control loop [74].

The pitch angle is modeled as:

$$\dot{\theta}_m = \omega_m \tag{2.18}$$

$$J_{eq}\dot{\omega}_m = T_m - T_e - B_{eq}\omega_m \tag{2.19}$$

where β_{eq} represents the equivalent damping coefficient [N.m/s], T_e represents the electromagnetic torque [N.m], and T_m represents the aerodynamic torque [N.m],

A general representation of the wind model in a Linear Time Invariant (LTI) system expression is:

$$\dot{x}(t) = Ax(t) + Bu(t) \tag{2.20}$$

$$y(t) = Cx(t) + Du(t) \tag{2.21}$$

where,

$u = \left[u_1,...u_p\right]^T$ represents the input vectors while $y = \left[y_1,...y_q\right]^T$ represents the output vectors. A valid assumption is that the matrices A, B, C, and D are compatible matrices.

A shorthand notation in the Laplace domain:

$$G(s) = \left[\begin{array}{c:c} A & B \\ \hdashline C & D \end{array}\right] \tag{2.22}$$

And the Matlab command line; $G(s) = ss(A, B, C, D)$ and $T = tf\,(G(s))$ returns a transfer function of the system.

Let

$$x_1 = \theta_m \tag{2.23}$$

$$x_2 = \frac{d\theta_m}{dt} \tag{2.24}$$

$$y = x_1 \tag{2.25}$$

Therefore, in the state space modelling the system can be represented as in a matrix form as:

$$\begin{bmatrix} \dot{x}_1 \\ \dot{x}_2 \end{bmatrix} = \begin{bmatrix} 1 & 0 \\ 0 & -\dfrac{B_{eq}}{J_{eq}} \end{bmatrix} \begin{bmatrix} x_1 \\ x_2 \end{bmatrix} + \begin{bmatrix} 0 \\ \dfrac{1}{J_{eq}} \end{bmatrix} u \tag{2.26}$$

where,

$$u = \left[T_m - T_e\right] \tag{2.27}$$

and,

$$y = \begin{bmatrix} 1 & 0 \end{bmatrix} \begin{bmatrix} x_1 \\ x_2 \end{bmatrix} \tag{2.28}$$

Hence,

$$A = \begin{bmatrix} 1 & 0 \\ 0 & -\dfrac{B_{eq}}{J_{eq}} \end{bmatrix} \tag{2.29}$$

$$B = \begin{bmatrix} 0 \\ \dfrac{1}{J_{eq}} \end{bmatrix} \tag{2.30}$$

$$C = \begin{bmatrix} 1 & 0 \end{bmatrix} \tag{2.31}$$

$$D = \begin{bmatrix} 0 \end{bmatrix} \tag{2.32}$$

2.4 Developing a state-space Permanent Magnet Synchronous Generator Model

Permanent Magnet Synchronous Generators (PMSG) have gradually penetrated the wind energy market at a high rate recently. PMSG's high power density provides an edge over other machines available in the wind industry. Developing an accurate model that closely mimic the practical behavior of the machine is of paramount importance in control system design. A single phase diagram shown in figure 2.6 [21] is sufficient to give an accurate electrical representation of the synchronous machine.

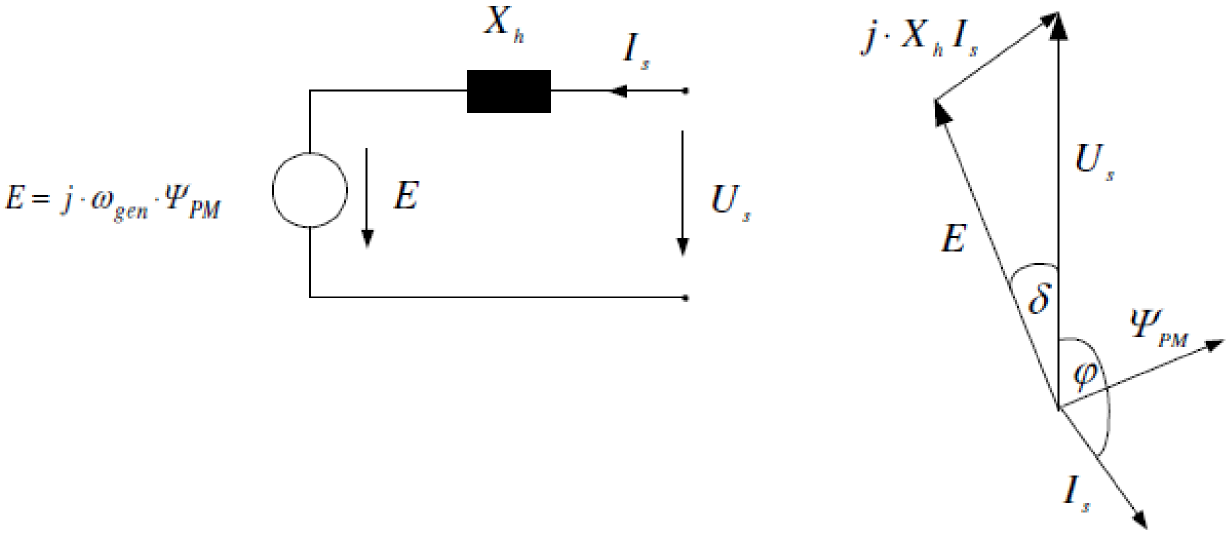

Figure 2.6: Single phase equivalent model and phasor diagram for a PMSG [21].

The validity of the PMSG electrical model is based on some crucial assumptions that are closely related to its real practical characteristics[21, 47]:

- The rotor and magnets have insignificant damping effects
- Omit all hysteresis losses and eddy currents in the system

- There is no importance derived from the magnetic saturation effects
- A sinusoidal approximation is imagined for the evenly distributed magnetic flux.

Under the above assumptions, the rate of change of the permanent magnet flux ψ_{PM} induces the internal voltage E in the stator windings:

$$E = \dot{\psi}_{PM} \tag{2.33}$$

Which in vector form is:

$$\vec{E} = j\omega_{gen}\vec{\psi}_{PM} \tag{2.34}$$

where the rotor mechanical angular speed ω_{gen} (rad/s) controls the amount of electrical voltage E produced by the generator.

The total reactance of the generator is:

$$X_h = R_s + j\omega_{gen}L_s \tag{2.35}$$

where the load angle δ (deg/ °) is a result of a voltage drop across the generators' reactance X_h **(Ω)** due to a load applied across the stator legs. The stator's winding resistance is R_s **(Ω)** and L_s (H)is the stator inductance.

According to the Kirchhoff's Voltage Law which states that the algebraic sum of all the voltage drops and the voltage sources around a closed loop sum to zero. Hence applying this principle in respect of the current flow in figure 2.6 above gives:

$$I_{s_{abc}}X_h + E_{abc} - U_{s_{abc}} = 0 \tag{2.36}$$

Substituting Eq. 2.34 and Eq. 2.35 into Eq. 2.36 gives

$$U_{s_{abc}} = R_s I_{s_{abc}} + j\omega_{gen}L_s I_{s_{abc}} + j\omega_{gen}\psi_{PM} \tag{2.37}$$

Which can be rewritten as,

$$U_{s_{abc}} = R_s I_{s_{abc}} + L_s\frac{dI_{s_{abc}}}{dt} + \frac{d\psi_{PM}}{dt} \tag{2.38}$$

Converting Eq. 2.38 to the rotor-oriented *dq*-reference frame (RRF) using the Park's transformation matrix:

$$\left[U_{s_{dq0}}\right]=\begin{bmatrix} \cos(\theta) & \cos\left(\theta-\frac{2\pi}{3}\right) & \cos\left(\theta+\frac{2\pi}{3}\right) \\ -\sin(\theta) & -\sin\left(\theta-\frac{2\pi}{3}\right) & -\sin\left(\theta+\frac{2\pi}{3}\right) \\ \frac{\sqrt{2}}{2} & \frac{\sqrt{2}}{2} & \frac{\sqrt{2}}{2} \end{bmatrix}\left[U_{s_{abc}}\right] \tag{2.39}$$

Gives

$$u_{sd}=R_s i_{sd}+L_d\frac{di_{sd}}{dt}-\omega_{gen}L_q i_{sq}+\frac{d\psi_{PM}}{dt} \tag{2.40}$$

$$u_{sq}=R_s i_{sq}+L_q\frac{di_{sq}}{dt}+\omega_{gen}L_d i_{sd}+\omega_{gen}\psi_{PM} \tag{2.41}$$

which can be represented in the equivalent *dq*-axes diagram in figure 2.7 below,

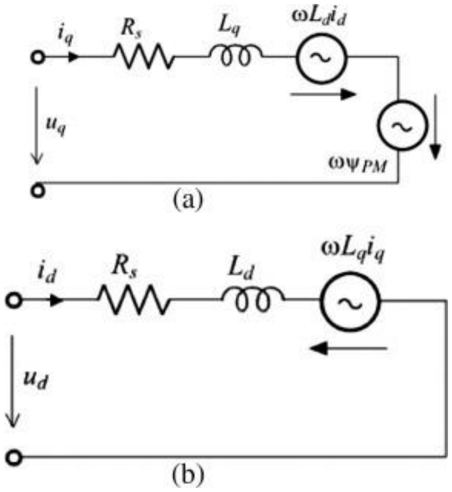

Figure 2.7: Equivalent *dq*-axis for a PMSG [21].

For state space modelling, let the state variable be:

$$\begin{bmatrix} x_3 & x_4 \end{bmatrix}^T=\begin{bmatrix} i_{sd} & i_{sq} \end{bmatrix}^T \tag{2.50}$$

Writing (1) and (2) in matrix form:

$$\begin{bmatrix} \dot{x}_3 \\ \dot{x}_4 \end{bmatrix} = \begin{bmatrix} \frac{-R}{L_d} & \frac{\omega_{gen} L_q}{L_d} \\ -\frac{\omega_{gen} L_d}{L_q} & \frac{-R}{L_q} \end{bmatrix} \begin{bmatrix} x_3 \\ x_4 \end{bmatrix} + \begin{bmatrix} \frac{1}{L_d} & 0 & \frac{1}{L_d} \\ 0 & \frac{1}{L_q} & \frac{1}{L_q} \end{bmatrix} u \tag{2.51}$$

$$y = \begin{bmatrix} 1 & 1 \end{bmatrix} \begin{bmatrix} x_3 \\ x_4 \end{bmatrix} + \begin{bmatrix} \frac{1}{L_d} & 0 & \frac{1}{L_d} \\ 0 & \frac{1}{L_q} & \frac{1}{L_q} \end{bmatrix} u \tag{2.52}$$

where

$$u = \begin{bmatrix} V_d & V_q & \dot{\psi}_{PM} \end{bmatrix}^T \tag{2.53}$$

If the rotating reference frame is in complete synchronism with the q-axis, then $V_q = 0$ hence

$$\begin{bmatrix} \dot{x}_3 \\ \dot{x}_4 \end{bmatrix} = \begin{bmatrix} \frac{-R}{L_d} & \frac{\omega_{gen} L_q}{L_d} \\ -\frac{\omega_{gen} L_d}{L_q} & \frac{-R}{L_q} \end{bmatrix} \begin{bmatrix} x_3 \\ x_4 \end{bmatrix} + \begin{bmatrix} \frac{1}{L_d} & 0 & \frac{1}{L_d} \\ 0 & \frac{1}{L_q} & \frac{1}{L_q} \end{bmatrix} u \tag{2.54}$$

$$y = \begin{bmatrix} 1 & 0 \end{bmatrix} \begin{bmatrix} x_3 \\ x_4 \end{bmatrix} + \begin{bmatrix} \frac{1}{L_d} & 0 & \frac{1}{L_d} \\ 0 & 0 & 0 \end{bmatrix} u \tag{2.55}$$

where

$$A = \begin{bmatrix} \frac{-R}{L_d} & \frac{\omega_{gen}}{L_d} \\ -\frac{\omega_{gen}}{L_q} & \frac{-R}{L_q} \end{bmatrix} \tag{2.56}$$

$$B = \begin{bmatrix} \frac{1}{L_d} & 0 & \frac{1}{L_d} \\ 0 & \frac{1}{L_q} & \frac{1}{L_q} \end{bmatrix} \tag{2.57}$$

$$C = \begin{bmatrix} 1 & 0 \end{bmatrix} \tag{2.58}$$

$$D = \begin{bmatrix} \frac{1}{L_d} & 0 & \frac{1}{L_d} \\ 0 & 0 & 0 \end{bmatrix} \tag{2.59}$$

2.5 PMSG’s Torque and Power modelling

The electrical power produced by the generator is [75, 76]:

$$P_{abc} = U_{abc} I_{abc} \cos\varphi \tag{2.60}$$

$$Q_{abc} = U_{abc} I_{abc} \sin\varphi \tag{2.61}$$

Where P_{abc} is the active power in abc reference frame, U_{abc} and I_{abc} are the voltage and currrent respectively. $\cos\varphi$ is the power factor.

In the *dq*-reference frame, the active and reactive powers are

$$P_{dq} = \frac{3}{2}\left[u_{sd} i_{sd} + u_{sq} i_{sq}\right] \tag{2.62}$$

$$Q_{dq} = \frac{3}{2}\left[u_{sq} i_{sd} - u_{sd} i_{sq}\right] \tag{2.63}$$

The the electrical torque that is produced by the PMSG is:

$$T_e = \frac{3}{2} p\left[i_{sq}\psi_{PM} + \left(L_d - L_q\right) i_{sd} i_{sq}\right] \tag{2.64}$$

where T_e is the electrical torque developed from the generator and p is the pole pairs.

If $L_d = L_q$ as is in many cases, then

$$T_e = \frac{3}{2} p\left[i_{sq}\psi_{PM}\right] \tag{2.65}$$

CHAPTER 3: VOLTAGE SOURCE CONVERTER – HIGH VOLTAGE DIRECT CURRENT (VSC-HVDC) MODELLING

Voltage Source Converter commonly referred to as a VSC forms the backbone infrastructure of a wind turbine generation system. It is made up of two converters connected back-to-back: generator-side or machine-side converter and grid side converter as shown in figure 3.1 [21] below. This chapter presents the full detail modelling of the VSC.

3.1 A Direct Driven PMSG Wind Turbine Based on VSC-HVDC Converter

A direct driven PMSG wind turbine based on a VSC-HVDC converter has three parts: a turbine system, a synchronous machine, and a VSC-HVDC converter [18], see figure 3.1 [21]. The turbine system captures the wind energy which is used to rotate the rotor of the generator; hence mechanical energy processed. The generator then converts this processed energy into electricity. A rare-earth permanent magnet synchronous machine has a constant magnet field that induces a variable voltage both in terms of magnitude and frequency in stator windings as the turbine rotates which needs to be stabilized into a source with constant magnitude and frequency through a converter [18].

The core equipment of the VSC-based HVDC converter are the converter switches, the converter reactor and the DC capacitors. The capacitor smoothens the dc voltage to achieve a ripple free voltage and act as an energy storage for the system. Using pulse width modulation (PWM) technology, the weak AC voltage from the PMSG is first converted to a DC voltage by the generator side converter, then the DC voltage is converted to an AC voltage by the grid side converter valves and the converter reactor controls the apparent power flow [16, 51]. Wind farms located in the offshore regions have been enabled into the grid by the VSC-HVDC connection due to the flexible active and reactive power control [52].

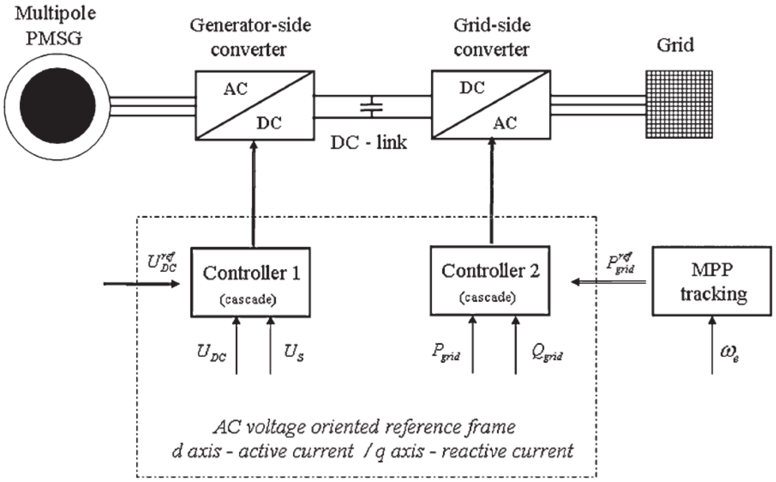

Figure 3.1: A typical VSC application system [21].

3.2 Machine-side converter modelling

The objective of the machine side controller (MSC) is to regulate the DC-link voltage across the capacitor and maintain the correct stator voltage from the PMSG [18]. The orthodox approach for the MSC controller is to carry out the MPPT control and stabilize the stator voltage of the PMSG [21]. The former approach improves the fault ride-through capability of the PMSG when compared to the latter [21]. The MSC has two loops: a faster inner current loop and a slower outer loop [18]. The slower outer loop provides dq axis references for the inner current loop: the DC-link voltage control provides a d-axis reference signal and the stator voltage control provides a q-axis reference signal.

The switching frequency for the VSC-HVDC system is taken to be 2 kHz. This is because IGBTs do not have an over-capability hence high switching frequency may damage them. The 2 kHz switching frequency is more applicable for a MW system. The inner current controller frequency bandwidth is taken to be one-fourth of the switching frequency [77] so that

$$\begin{aligned} f_{\mathrm{BANDWIDTH}} &= \frac{1}{4} f_{switching} = \frac{1}{4} \times 2\ \mathrm{kHz} \\ &= 500\ \mathrm{Hz}\ \left(3141\ \mathrm{rad/s}\right) \end{aligned} \tag{3.1}$$

The delay introduced by the converter PWM is equal to half the converter switching frequency. Hence

$$\begin{aligned} T_a &= \frac{T_{\mathrm{switch}}}{2} = \frac{1}{2 f_{\mathrm{switch}}} = \frac{1}{2 \times 2\ \mathrm{kHz}} \\ &= 250\ \mu\mathrm{s} \end{aligned} \tag{3.2}$$

3.2.1 Inner current control loops

The PMSG model as developed in detailed in chapter 2 is given by:

$$\begin{bmatrix} \dot{x}_1 \\ \dot{x}_2 \end{bmatrix} = \begin{bmatrix} \frac{-R}{L_d} & \frac{\omega_e}{L_d} \\ -\frac{\omega_e}{L_q} & \frac{-R}{L_q} \end{bmatrix} \begin{bmatrix} x_1 \\ x_2 \end{bmatrix} + \begin{bmatrix} \frac{1}{L_d} & 0 & 0 \\ 0 & \frac{1}{L_q} & 0 \end{bmatrix} u \tag{3.3}$$

$$y = \begin{bmatrix} 1 & 0 \end{bmatrix} \begin{bmatrix} x_1 \\ x_2 \end{bmatrix} + \begin{bmatrix} 0 & 0 & -\frac{\omega_e}{L_q} \end{bmatrix} u \tag{3.4}$$

where

$$u = \begin{bmatrix} V_d & V_q & \lambda \end{bmatrix}^T$$

If the rotating reference frame is in complete synchronism with the q-axis, then $V_q = 0$ hence

$$\begin{bmatrix} \dot{x}_1 \\ \dot{x}_2 \end{bmatrix} = \begin{bmatrix} \frac{-R}{L_d} & \frac{\omega_e}{L_d} \\ -\frac{\omega_e}{L_q} & \frac{-R}{L_q} \end{bmatrix} \begin{bmatrix} x_1 \\ x_2 \end{bmatrix} + \begin{bmatrix} \frac{1}{L_d} & 0 & 0 \\ 0 & 0 & 1 \end{bmatrix} u \tag{3.5}$$

$$y = \begin{bmatrix} 1 & 0 \end{bmatrix} \begin{bmatrix} x_1 \\ x_2 \end{bmatrix} + \begin{bmatrix} 0 & 0 & -\frac{\omega_e}{L_q} \end{bmatrix} u \tag{3.6}$$

Clearly converting from the abc reference frame to the dq0 synchronous frame has introduced frequency induced terms hence created a coupling effect between the dq equations. The rotor flux linkage appears on the q axis only. So decoupling the system, a controller feedback design is proposed as explained below.

3.2.1.1 Controller feedback design benefits

For the proposed vector control strategy, the direct-current vector control without the decoupled terms uses the benefits of a feedback design to eliminate the effects of the decoupled-terms, see Figure 3.2. There are three main reasons for a controller feedback design [78]: stabilising an open loop unstable process, reducing the effect of disturbances on the system output, and reducing the effect of plant variations on performance.

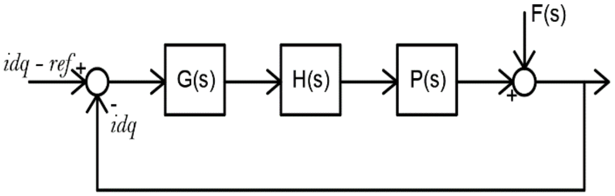

Figure 3.2: Inner loop block diagram.

The stator voltage system in Eq. 3.3 and Eq. 3.4 from the conventional vector modelling and taking Laplace gives

$$\frac{I_d(s)}{V_d(s) + \omega_e L_q I_q(s)} = \frac{1}{(R + sL_d)} \tag{3.7}$$

For simplification of the mathematics and clear presentation, let:

$$F(s) = \omega_e L_q i_q \tag{3.8}$$

$$P(s) = \frac{1}{\left(R + sL_d\right)} \tag{3.9}$$

$$H(s) = \frac{1}{\left(sT_a + 1\right)} \tag{3.10}$$

where T_a is the converter delay and also $G(s)$ in Fig. 3.2 is the PI controller. Therefore, for the block diagram shown Figure 3.2;

$$I_d = \frac{GHP}{1+GHP} I_d^{ref} + \frac{1}{1+GHP} F \tag{3.11}$$

The last term indicates how the feedback loop can reduce the effect of the coupling term

$$F = \omega_e L_q i_q \tag{3.12}$$

It can be shown from Eq. 3.11 that as *G* increases, the effect of the coupling term on the output becomes smaller. To eliminate the effect then the gain *G* should approach infinite; i.e.:

$$\lim_{G\to\infty}\left(I_d\right) = \lim_{G\to\infty}\left(\frac{GHP}{1+GHP} I_d^{ref}\right) + \lim_{G\to\infty}\left(\frac{1}{1+GHP} F\right) \tag{3.13}$$

Evaluating Eq.3.13,

$$I_d = I_d^{ref} \tag{3.14}$$

The controller is implemented as shown in Figure 3.3. The current signal references are provided by the DC-link and stator voltage controllers.

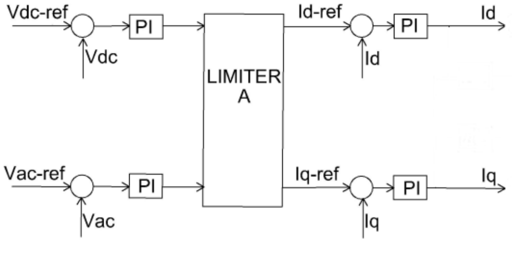

Figure 3.3: Proposed control configuration.

3.2.2 Outer current control loops

The outer control loops are made up of either a direct voltage control, alternating voltage control, apparent power control. The outer control should be faster that the inner control so as to effectively damp out oscillations: the triggering frequency is 1/4th of the inner loop frequency [59].

3.2.2.1 Direct voltage control

The importance of the DC voltage control in the VSC-HVDC is to regulate the DC-link voltage to its reference value [58]. There are two conditions that can be measured so as to derive the DC voltage model:

$$I_{dc} = I_L + I_{cap} \tag{3.15}$$

I_{cap} is the current through the DC capacitor so that

$$I_{cap} = I_{dc} + I_L \tag{3.16}$$

$$C\frac{dV_{dc}}{dt} = I_{dc} + I_L \tag{3.17}$$

Considering I_L as a disturbance into the system model and applying the same design reasoning approach as in the inner current control loop. Therefore

$$sCV_{dc} = I_{dc} \tag{3.18}$$

$$\frac{V_{dc}}{I_{dc}} = \frac{1}{sC} \tag{3.19}$$

3.2.2.2 AC voltage control

The role of the ac voltage is to keep the stator voltage constant to the reference value. To achieve this goal, the voltage drop caused by the stator impedance and the transmission parameters are use employed to determine the measured value. And it is the measured value that is compared to the reference one. If a difference in signal is obtained, it is sent to a PI-controller which adjusts the control signal so as to bring the voltage to the desired value. The ac voltage model is derived using Eq. (4.42) [79, 80]

$$\Delta U = U_s - U_{con} = \frac{RP_{gen} + XQ_{gen}}{U_s} \tag{3.20}$$

Where, U_s is the sending voltage from the stator winding, U_{con} is the voltage at the foot of the converter, R is the stator winding resistance together with the transmission one and X is the synchronous reactance combined with the transmission reactance.

A general assumption is that the resultant reactance is far greater than the resultant resistance such that $X >> R$, then the voltage drop across the resultant reactance depends only on the reactive power flow.

$$\Delta U = U_s - U_{con} = \frac{XQ_{gen}}{U_s} = \frac{-3Xu_{sd}}{2u_{sd}} i_{sq} \tag{3.21}$$

$$\frac{\Delta u_{sd}}{\Delta i_{sq}} = -\frac{3X_s}{2} = \frac{3sL}{2} \tag{3.22}$$

3.3 Grid-Side Converter

The grid-side converter converts the dc voltage to ac voltage using the pulse width modulation technology, see figure 3.4 [59]. The ac voltage should modulate a fixed frequency of 50 Hz. The objective of the GSC controller is to regulate the reactive power and conduct the MPPT control [21, 81]. Again the traditional approach has been for the GSC to regulate the dc-link voltage and control the reactive power. The former approach improves the fault ride-through capability of the PMSG as compared to the later [82] . The GSC has two loops: a faster inner current loop and a slower outer loop [18]. The slower outer loop provides *dq* axis references for the inner current loop: the speed controller provides a d-axis reference signal and the reactive power controller provides a q-axis reference signal.

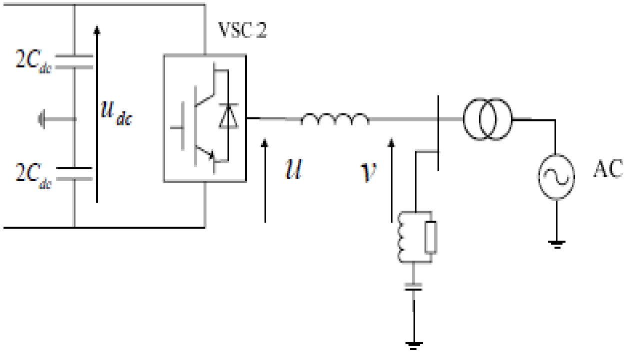

Figure 3.4: A typical Grid-Side Converter schematic diagram [59].

Applying a Kirchhoff's law in the figure 3.4 [59] above and taking the three phases system as balanced in the network, the following equations are derived from the system [60]:

$$\begin{bmatrix} u_a \\ u_b \\ u_c \end{bmatrix} = L_g \frac{d}{dt}\begin{bmatrix} i_a \\ i_b \\ i_c \end{bmatrix} + R_g \begin{bmatrix} i_a \\ i_b \\ i_c \end{bmatrix} + \begin{bmatrix} v_a \\ v_b \\ v_c \end{bmatrix} \tag{3.23}$$

where u_{abc} is the sending ac voltage after being converted from the dc voltage, i_{abc} is the current in the grid and v_{abc} is the point of common coupling voltage. L_g and R_g are the grid transmission parameters: inductance and resistance respectively.

Eq. 3.23 in vector form is:

$$u_{abc} = R_g i_{abc} + L_g \frac{di_{abc}}{dt} + v_{abc} \tag{3.24}$$

Then converting Eq. 3.24 to the rotor-oriented *dq*-reference frame (RRF) using the Park's transformation matrix:

$$\left[u_{s_{dq0}}\right] = \begin{bmatrix} \cos(\theta) & \cos\left(\theta - \frac{2\pi}{3}\right) & \cos\left(\theta + \frac{2\pi}{3}\right) \\ -\sin(\theta) & -\sin\left(\theta - \frac{2\pi}{3}\right) & -\sin\left(\theta + \frac{2\pi}{3}\right) \\ \frac{\sqrt{2}}{2} & \frac{\sqrt{2}}{2} & \frac{\sqrt{2}}{2} \end{bmatrix} \left[u_{s_{abc}}\right] \tag{3.25}$$

Gives

$$v_{gd} = u_{gd} - R_g i_{gd} - L_{gd}\frac{di_{gd}}{dt} + \omega_g L_{gq} i_{gq} \tag{3.26}$$

$$v_{gq} = u_{gq} - R_g i_{gq} - L_{gq}\frac{di_{gq}}{dt} - \omega_g L_{gd} i_{gd} \tag{3.27}$$

where v_{gd} and v_{gq} are the *dq*-axis pcc grid voltages, u_{gd} and u_{gq} are the modulated grid voltages from the foot of the converter, i_{gd} and i_{gq} are the *dq*-axis grid currents, ω_g is the grid frequency term.

If the rotating reference frame is in complete synchronism with the q-axis, then $u_{gq} = 0$ hence

$$v_{gd} = u_{gd} - R_g i_{gd} - L_{gd} \frac{di_{gd}}{dt} + \omega_g L_{gq} i_{gq} \tag{3.28}$$

$$v_{gq} = -R_g i_{gq} - L_{gq} \frac{di_{gq}}{dt} - \omega_g L_{gd} i_{gd} \tag{3.29}$$

The sending ac voltage u_{gd} is controlled by the dc voltage and the modulation index m. If the dc voltage increases the modulation index decreases in such a way that that it keeps the ac voltage constant. The relationship between the ac voltage, dc voltage and the modulation index summed up in the mathematical equation below; Eq. 3.30

$$u_{gd} = u_{dc} \cdot m \cdot \frac{\sqrt{3}}{2\sqrt{2}} \tag{3.30}$$

So substituting Eq. 3.30 into Eq. 3.28 gives

$$v_{gd} = -R_g i_{gd} - L_{gd} \frac{di_{gd}}{dt} + u_{dc} \cdot m \cdot \frac{\sqrt{3}}{2\sqrt{2}} + \omega_g L_{gq} i_{gq} \tag{3.31}$$

$$v_{gq} = -R_g i_{gq} - L_{gq} \frac{di_{gq}}{dt} - \omega_g L_{gd} i_{gd} \tag{3.32}$$

For state space modelling, let the state variables be:

$$\begin{bmatrix} x_5 & x_6 \end{bmatrix}^T = \begin{bmatrix} i_{gd} & i_{gq} \end{bmatrix}^T \tag{3.33}$$

Writing Eq. 3.31 and Eq. 3.32 in matrix form:

$$\begin{bmatrix} \dot{x}_5 \\ \dot{x}_6 \end{bmatrix} = \begin{bmatrix} \frac{-R_g}{L_{gd}} & \frac{\omega_g}{L_{gd}} \\ -\frac{\omega_g}{L_{gq}} & \frac{-R_g}{L_{gq}} \end{bmatrix} \begin{bmatrix} x_5 \\ x_6 \end{bmatrix} + \begin{bmatrix} \frac{1}{L_{gd}} & 0 & m \cdot \frac{\sqrt{3}}{L_{gd} \cdot 2\sqrt{2}} \\ 0 & \frac{1}{L_{gq}} & 0 \end{bmatrix} u \tag{3.34}$$

$$y = \begin{bmatrix} 1 & 0 & 0 \end{bmatrix} u \tag{3.35}$$

where

$$u = \begin{bmatrix} V_{gd} & V_{gq} & u_{dc} \end{bmatrix}^T \tag{3.36}$$

Applying the proposed decoupling method as described in chapter 2, the decoupled model of the inner current loop is given by:

$$\begin{bmatrix} \dot{x}_5 \\ \dot{x}_6 \end{bmatrix} = \begin{bmatrix} \frac{-R_g}{L_{gd}} & 0 \\ 0 & \frac{-R_g}{L_{gq}} \end{bmatrix} \begin{bmatrix} x_5 \\ x_6 \end{bmatrix} + \begin{bmatrix} \frac{1}{L_{gd}} & 0 & 0 \\ 0 & 0 & 0 \end{bmatrix} u \tag{3.37}$$

$$y = \begin{bmatrix} 1 & 0 & 0 \end{bmatrix} u \tag{3.38}$$

Therefore,

$$A = \begin{bmatrix} \frac{-R_g}{L_{gd}} & 0 \\ 0 & \frac{-R_g}{L_{gq}} \end{bmatrix} \tag{3.39}$$

$$B = \begin{bmatrix} \frac{1}{L_{gd}} & 0 & 0 \\ 0 & 0 & 0 \end{bmatrix} \tag{3.40}$$

$$C = \begin{bmatrix} 1 & 0 \end{bmatrix} \tag{3.41}$$

$$D = \begin{bmatrix} 0 \end{bmatrix} \tag{3.42}$$

3.3.1 Outer current controller

The outer controller is made up of two PI-controllers: active power controller which receives its reference signal from the optimal curve model and the reactive power controller which sets the q-axis reference signal for the inner control loop, see figure 3.5 [59] below.

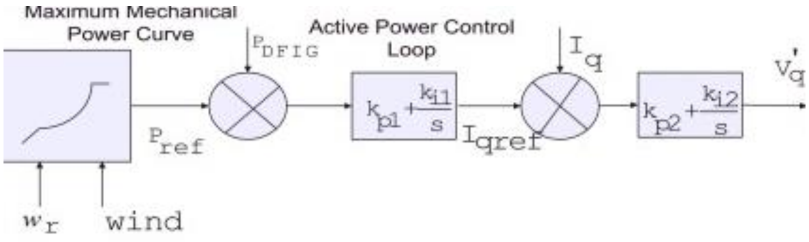

Figure 3.5: A block diagram for active power control loop [59].

3.3.1.1 Active power controller

The reference signal to the active power controller is set using a maximum power point tracking (MPPT) method. It employs an optimal relationship-based (ORB) control to provide the reference signal in which the measured rotor speed of the PMSG is compared to the wind speed variation. This then generates the optimal power value P_{ref} from the wind turbine's maximum power curve [80, 83, 84].

$$P_{ref} = \frac{1}{2}\rho A C_{P_{opt}} \left(\frac{\omega_{r_{opt}} r}{\lambda_{opt}} \right)^3 \tag{3.43}$$

$$P_{ref} = K_{opt} \omega_{r_{opt}}^3 \tag{3.44}$$

where, K_{opt} is the optimal power constant given by

$$K_{opt} = \frac{1}{2}\rho A C_{P_{opt}} \left(\frac{r}{\lambda_{opt}} \right)^3 \tag{3.45}$$

The power exchange between the VSC and the network system can be represented in equation below. The active instantaneous powers, P_{grid} in the *dq0* reference frame as described in [59].

$$P_{grid} = \frac{3}{2}\left(v_{gd}i_{gd} + v_{gq}i_{gq}\right) \tag{3.46}$$

In the *dq0* axis, the V_{gd} is assumed to be in perfect synchronism with the d-axis hence $V_{gq} = 0$.

$$P_{grid} = \frac{3}{2}v_{gd}i_{gd} \tag{3.47}$$

Therefore, the power transfer function is given by:

$$\frac{P_{grid}}{i_{gd}} = \frac{3}{2}v_{gd} \tag{3.48}$$

3.3.1.2 Reactive Power controller

The reference signal, Q_{ref} of the reactive power control loop is usually set to zero as the converter does not generate reactive power to the grid. The ref signal is then compared to the measured grid reactive power, the difference is then set to the PI-controller for adjustment, see figure 3.6 [59]. Thereafter, the controller sends a q-ref signal for the inner current loop.

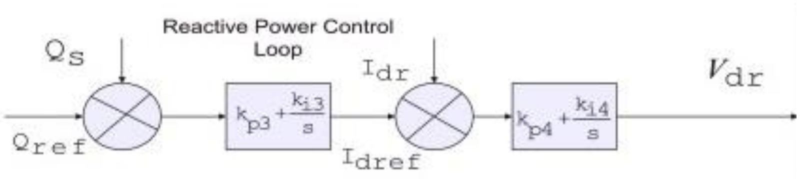

Figure 3.6: A block diagram for reactive power control loop [59].

The reactive power exchange between the VSC and the network system can be represented in equation below. The reactive instantaneous power, Q_{grid} in the *dq0* reference frame as described in [59].

$$Q_{grid} = \frac{3}{2}\left(v_{gd}i_{gq} - v_{gq}i_{gd}\right) \tag{3.49}$$

In the *dq0* axis, the v_{gd} is assumed to be in perfect synchronism with the d-axis hence $v_{gq}=0$.

$$Q_{grid} = \frac{3}{2}v_{gd}i_{gq} \tag{3.50}$$

Therefore, the power transfer function is given by:

$$\frac{Q_{grid}}{i_{gq}} = \frac{3}{2}v_{gd} \tag{3.51}$$

CHAPTER 4: PMSG AND VSC-HVDC RATING AND SIZING

This chapter gives the component sizing and rating of each item that is used in this project together with the justification and reasoning behind the choices made. Engineering trade-offs are made with a goal of achieving better performances and efficiency

4.1 PMSG rating and components sizing

The direct driven wind turbine based PMSG is rated from literature as follows:

Table 4-1: Specifications for a wind turbine system [3]

Parameters	Values
Rated Mechanical Power (MW)	2
Cut-in wind speed (m/s)	4
Rated wind speed (m/s)	13
Cut-out wind speed (m/s)	25
Number of rotor blades	3
Length of blades (m)	37.5
Rotor diameter (m)	76.42
Rotor area (m^2)	4587
Speed range (rpm)	13 – 21.9
Rated speed (rpm)	19
Rotor mass (kg)	40

Table 4-2: Specifications for a PMSG [85]

Parameters	**Value**
Generator Type	Direct driven PMSG
Rated Mechanical Power (MW)	2.0
Rated Apparent Power (MVA)	2.2419
Rated line-to line voltage (V, peak)	975.80
Rated Phase Voltage (V, peak)	563.42
Rated Stator Current (A, peak)	2641.41
Rated Stator Frequency (Hz)	9.75
Rated Power factor	0.8921
Rated Rotor speed (rpm)	22.5
Number of Pole Pairs	26
Rated Mechanical Torque (kNm)	848.826
Rated Rotor Flux Linkage (Wb, peak)	8.24
Stator Winding Resistance (mΩ)	8.21
d-axis Synchronous Inductance (mH)	1.5731
q-axis Synchronous Inductance (mH)	1.5731

From the information derived in the tables above, the inertia of the wind turbine is [85]:

$$J_{turbine} = m\left(\frac{L_{blade}}{n_{blade}}\right)^2 \tag{4.1}$$

Where the mass of the rotor *m* [kg] is directly proportional to the wind inertia. *L* and *n* are the rotor blades length and the number of rotor blades making up the wind turbine.

Therefore, the wind inertia of the system used in this study is taken to be:

$$J_{turbine} = 40 \text{ kg } \times\left(\frac{37.5 \text{ m}}{3}\right)^2 = 6250 \text{ kg/m}^2 \tag{4.2}$$

Then the energy potential in the wind turbine is [85] :

$$E_{turbine} = \frac{1}{2} J_{turbine} \left(\omega_r\right)^2 \tag{4.3}$$

$$E_{turbine} = \frac{1}{2} \times 6250 \left(\frac{2\pi \times 9.75}{26} \right)^2 = 7.363 \times 10^3 \tag{4.4}$$

The inertia constant which is usually used in small signal power system stability is given by [85]:

$$H_{turbine} = \frac{E_{turbine}}{S_{turbine}} \tag{4.5}$$

$$H_{turbine} = \frac{7.363 \times 10^3}{2.5 \times 10^6} = 0.002945 \tag{4.6}$$

The power coefficient C_p as discussed in chapter 2 is rated as follows:

$$C_p = \frac{2P_m}{\rho A v_w^3} \tag{4.7}$$

With the rated power as 2 MW, the air density as 1.225 kg/m^3, the rated speed as 13 m/s and the given area swept by the rotor as 4587 m^2, the C_p then is:

$$C_p = \frac{2\left(2 \times 10^6\right)}{1.225 \times 4587 \times 13^3} = 0.324 \tag{4.8}$$

4.1.1 Implementation of the Wind turbine in Psim software

A wind turbine is implemented as shown figure 4.1 below. The wind speed is realised using a piecewise linear voltage source. It changes/varies according to the time and speed entered in its data. The pitch value is controlled by the pitch controller. The turbine produces the torque that is used to the rotor. The drive-train system has one gear to gear ratio to depict as a gearless system. The parameters entered in the wind data box are obtained from calculations and the table 4-1 above.

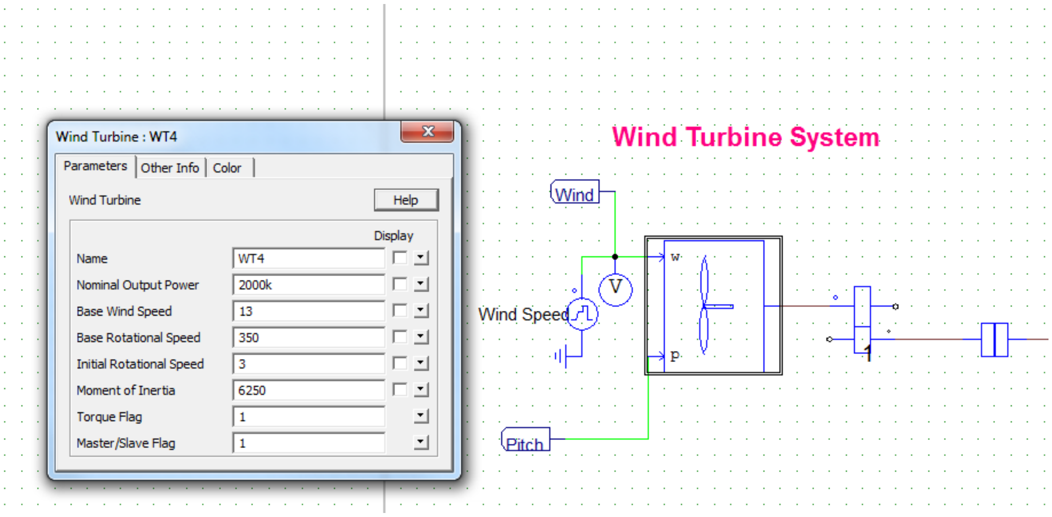

Wind Turbine

		Display
Name	WT4	☐
Nominal Output Power	2000k	☐
Base Wind Speed	13	☐
Base Rotational Speed	350	☐
Initial Rotational Speed	3	☐
Moment of Inertia	6250	☐
Torque Flag	1	
Master/Slave Flag	1	

Figure 4.1: Wind turbine system implementation in Psim software

4.1.2 Implementation of the PMSG in Psim software

A permanent magnet synchronous machine or generator is connected to the wind turbine via a mechanical coupling block which couples together the two mechanical systems. Then a torque sensor is used to measure the torque transferred from the wind turbine to the generator and a speed sensor is used to measure the mechanical angular speed. This information is sent to the control unit to monitor the maximum mechanical power extracted in the system. The parameters entered in the wind data box are obtained from calculations and table 4.2 above. Figure 4.2 shows the implementation of the system.

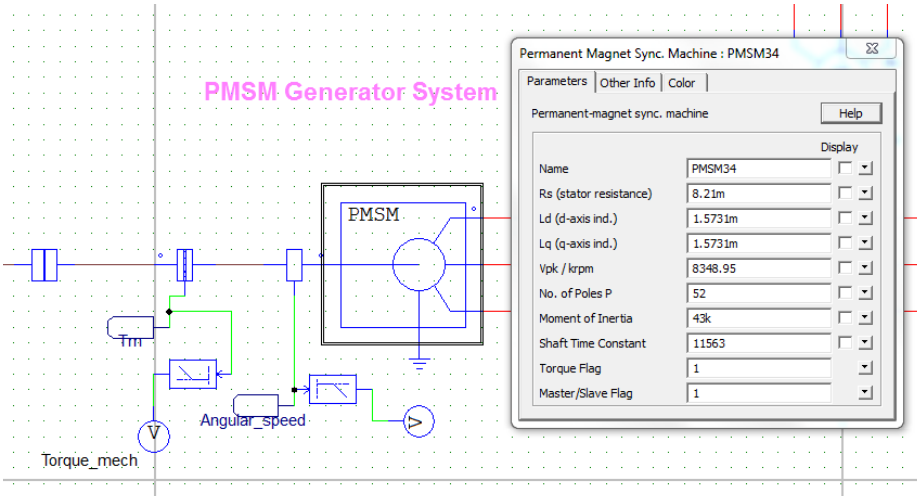

Permanent-magnet sync. machine

		Display
Name	PMSM34	☐
Rs (stator resistance)	8.21m	☐
Ld (d-axis ind.)	1.5731m	☐
Lq (q-axis ind.)	1.5731m	☐
Vpk / krpm	8348.95	☐
No. of Poles P	52	☐
Moment of Inertia	43k	☐
Shaft Time Constant	11563	☐
Torque Flag	1	
Master/Slave Flag	1	

Figure 4.2: PMSG generator system implementation in Psim software

4.2 VSC-HVDC rating and component sizing

The VSC-HVDC system acts as a synchronous machine whereby the ac voltage is controlled almost instantly, Eq. 4.9 describes the relationship between the dc voltage, modulation index and the fundamental frequency, ω_e. [17]

$$u_{ac} = \frac{1}{2} u_{dc} M \sin\left(\omega_e t + \delta\right) + h\left(n_i\right) \tag{4.9}$$

where the ac voltage phase shift is represented by δ and the harmonics produced by the modulating the system voltage is represented by *h(n)* and depends on the harmonic order.

The harmonics affect the output voltage wave profile and create ripples in the system. In today's very sensitive systems, the harmonics can damage the system. So filters are designed to remove them.

The desired output voltage is achieved by varying the modulation index and the phase shift separately. If the output voltage is too high to that of which is wanted, the modulation index is reduced.

The power flow is controlled instantaneously: the reactive power produced by the PMSG is consumed by the converter hence does not reach the grid-side level. Only the active power passes through the converter to the grid. The relationship of active and reactive power flow is described by Eq.4.10 and Eq.4.11 below:

$$P = \frac{|v||u|\sin\delta}{X} \tag{4.10}$$

$$Q = \frac{|v|\left(|v| - |u|\cos\delta\right)}{X} \tag{4.11}$$

4.2.1 Converter rating

The size of the converter rating is designed on the fact that modern power systems need to meet the voltage limit requirement at all times respective of the conditions of operation. So the active power being transmitted across the converter controls the converter rating design as well.

Since the rated mechanical power from the PMSG specifications is 2 MW and the rated apparent power is 2.2419 MVA, the VSC-HVDC rating is selected to be 6 MVA taking into consideration the ac filters and that the converter has to consume the reactive power from the generator. It is also expected to support the grid voltage with its reactive power whenever it is required.

4.2.2 IGBT rating

Technology advancement has tremendously improved the performances of IGBTs and its applications in industry. For the wind turbine system, the IGBT is connected in anti-parallel with a diode to enable the bi-directional flow of power in the converter system. Each IGBT electronic device is rated a nominal current of 500-1500 A, 2.5 kV rated voltage and rated frequency of 2 kHz [86].

The low frequency (2 kHz) is chosen so as to handle the mega power that is produced by the wind turbine generator. A high switching frequency could cause communication failure in the converter valves. Figure 4.3 [86] shows a typical IGBT hardware available in the market.

Figure 4.3: A typical IGBT hardware for a VSC system [86].

4.2.3 Implementation of the IGBTs in Psim software

The machine side converter is realised by connecting the IGBTs in parallel with diodes. The signals are generated by the control system unit. It switches on and off depending on the received signal see figure 4.4 below.

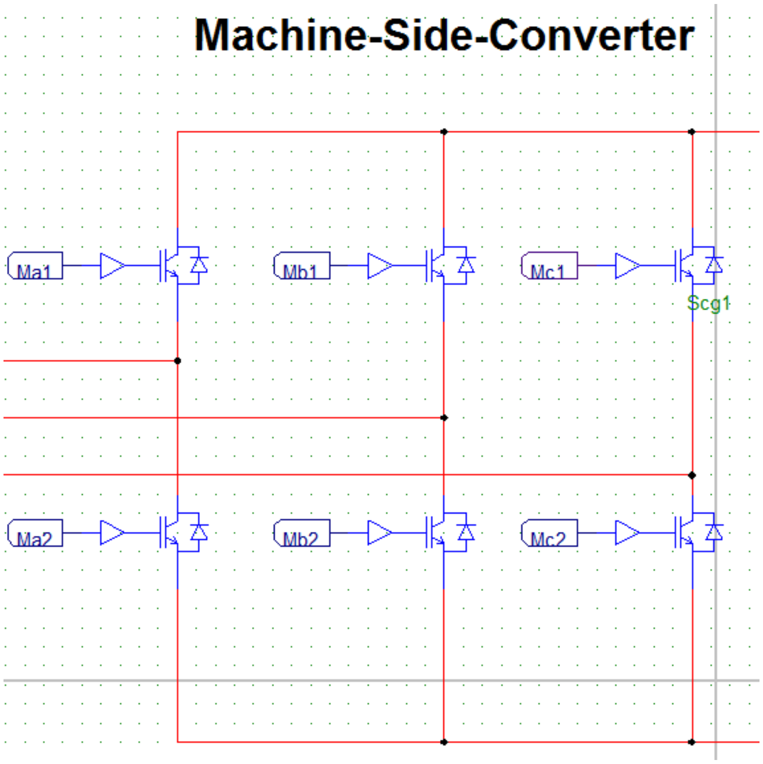

Figure 4.4: The implementation of the MSC

4.2.4 Grid Transformer

The transformer connects the point of common coupling (PCC) voltage to the grid. It plays an important role during faults as it helps regulate the fault current through its reactance. The transformer steps up the PCC voltage to meet that of the grid. Voltage regulation can be improved by using transformers with tap changers [87].

4.2.5 Implementation of the coupling transformer in Psim software

The transformer is realised in Psim as shown in figure 4.5 below. It connects the wind turbine power system to the utility grid with the required voltage.

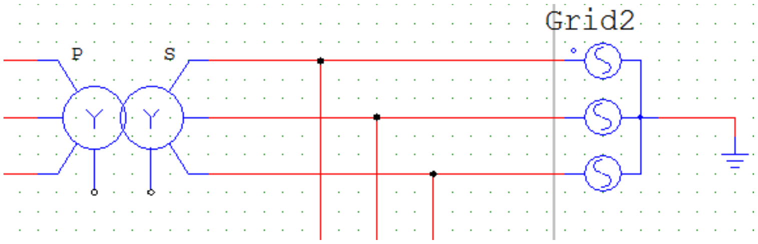

Figure 4.5: Grid coupling transformer

4.2.6 Transmission line parameters

The VSC-HVDC system has a phase reactor which models the transmission line behaviour. The phase reactor is crucial in supporting the VSC-HVDC to control the active and reactive powers independently. The reactor's other function is to filter out the higher order harmonics contained by the grid's output current [88]. It is crucial to appropriately select a correct coupling inductance as this affects the resultant filtering and harmonic tracking capability directly [89].

$$L = \frac{\delta_v v_{dc}}{r\omega_g I_c} \tag{4.12}$$

where δ_v is a factor value with typical range of 0.1-0.3, r represents the expected harmonic order and I_c is the rated grid current.

Taking the factor value δ_v as 0.23, then r as 3 and the rated current I_c as 5 kA, the coupling inductance is:

$$L = \frac{0.23\times 1800}{3\times 2\pi \times 50\times 5\times 10^3} = 0.08751 \text{ mH} \tag{4.13}$$

4.2.7 Implementation of the coupling inductance in Psim software

The coupling reactance is implemented as shown in figure 4.6 below.

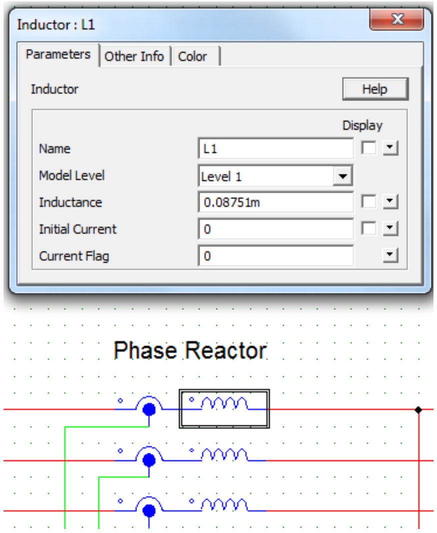

Name: L1
Model Level: Level 1
Inductance: 0.08751m
Initial Current: 0
Current Flag: 0

Figure 4.6: Phase reactor model

4.2.8 DC-Capacitor rating

The capacitor functions as energy storage of the system. It also works perfectly to decrease some voltage ripples in the dc-voltage. This stable dc voltage is then used to generate an ac-voltage on the grid-side of the converter. The capacitor consumes the unwanted high-frequency current components built by the converter switching operation [17]. The capacitor rating is determined by the magnitude of power that is being transported across the converter so the general *capacitor time constant* is defined as [57, 90].

$$\tau = \frac{C_{dc} v_{dc}^2}{2S_m} \tag{4.14}$$

Where the dc capacitance C_{dc} varies proportional to the time constant. V_{dc} is the dc voltage and S_m is the rated apparent power of the converter.

The time constant is equivalent to the time it takes to charge the capacitor from zero to V_{dc} using the active power produced by the PMSG [57]. In [17], a time constant selection is based on 4ms whereas ABB in [88] based the time constant in 2 ms. So selecting an average time constant of 3.2 ms, the capacitor size is:

$$C_{dc} = \frac{2\tau P_m}{v_{dc}^2} \tag{4.15}$$

$$C_{dc} = \frac{2 \times 3.2 \times 10^{-3} \times 6 \times 10^{6}}{(1800)^2} \tag{4.16}$$

$$C_{dc} = 11.83 \text{ mF} \tag{4.17}$$

4.2.9 Implementation of the dc capacitor in Psim software

The dc-capacitor is implemented as shown in figure 4.7. The values are from the calculations above.

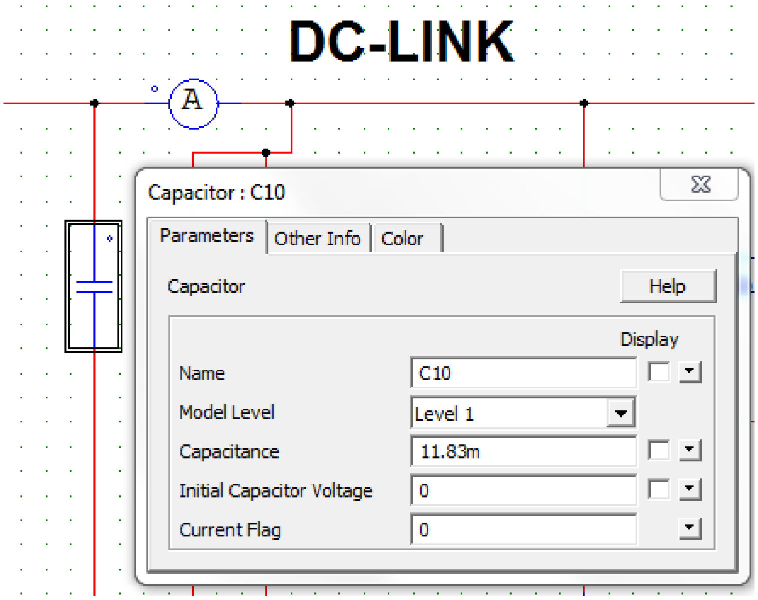

Name: C10

Model Level: Level 1

Capacitance: 11.83m

Initial Capacitor Voltage: 0

Current Flag: 0

Figure 4.7: The dc-link voltage in psim software

4.2.10 DC voltage rating

The dc voltage rating is determined in such a way that the converter does not saturate when it is switching on/off using the SPWM technology [21, 79, 91]. So the minimum dc voltage is:

$$v_{dc} = 2\sqrt{\frac{2}{3}} v_{LL} \cdot m \tag{4.18}$$

Where v_{LL} is the line-line peak voltage value and m is the modulation index.

Therefore, the rated dc voltage is given by Eq.4.19 with the rated voltage v_{LL}=1.25 kV and $m = 0.9$

$$v_{dc} = 2\sqrt{\frac{2}{3}} \times 1250 \times 0.9 \tag{4.19}$$

$$v_{dc} = 1.836 \text{ kV} \tag{4.20}$$

4.2.11 AC- grid filters

Producing a good output voltage and current waveforms is very crucial in meeting the grid integration of the renewable energy. The switching operation of the converter valves introduces harmonics in the system voltage and current. So these harmonics must be prevented from entering the grid as it can cause system failure and damage to today's very delicate equipment. Passive filters are employed to filter out the harmonic contents in the voltage waveforms, see figure 4.8. There are connected in between the phase reactor and the transformer [88, 92]. The ac-filters are designed following a close example of matlab's example: *power_wind_type_4_det.* The ac-filters are rated at 30% of the converter rating [93].

$$Q_{cap-filter} = 0.15 \text{ MVAr}$$

$$Z = \frac{[kV]^2}{Q_{cap-filter}} \tag{4.21}$$

$$Z = \frac{1}{0.15} = 6.67\ \Omega$$

$$C_{cap-filter} = 0.5 \text{ mF} \qquad 4.22)$$

And also,

$$Q_{RC-filter} = 1.6 \text{ MVA}$$

$$Z = \frac{[kV]^2}{Q_{RC-filter}} \tag{4.23}$$

$$|Z| = \frac{1}{1.6} = 6.67\ \Omega$$

$$\begin{aligned} R_{RC-filter} &= 0.5\ \Omega \\ C_{RC-filter} &= 30 \text{ mF} \end{aligned} \tag{4.24}$$

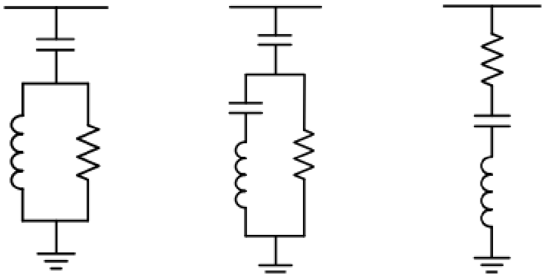

Figure 4.8: A typical ac-side filter system configuration

4.2.11 Implementation of the ac filters in Psim software

The ac-filters are implemented as shown the figure 4.9 below.

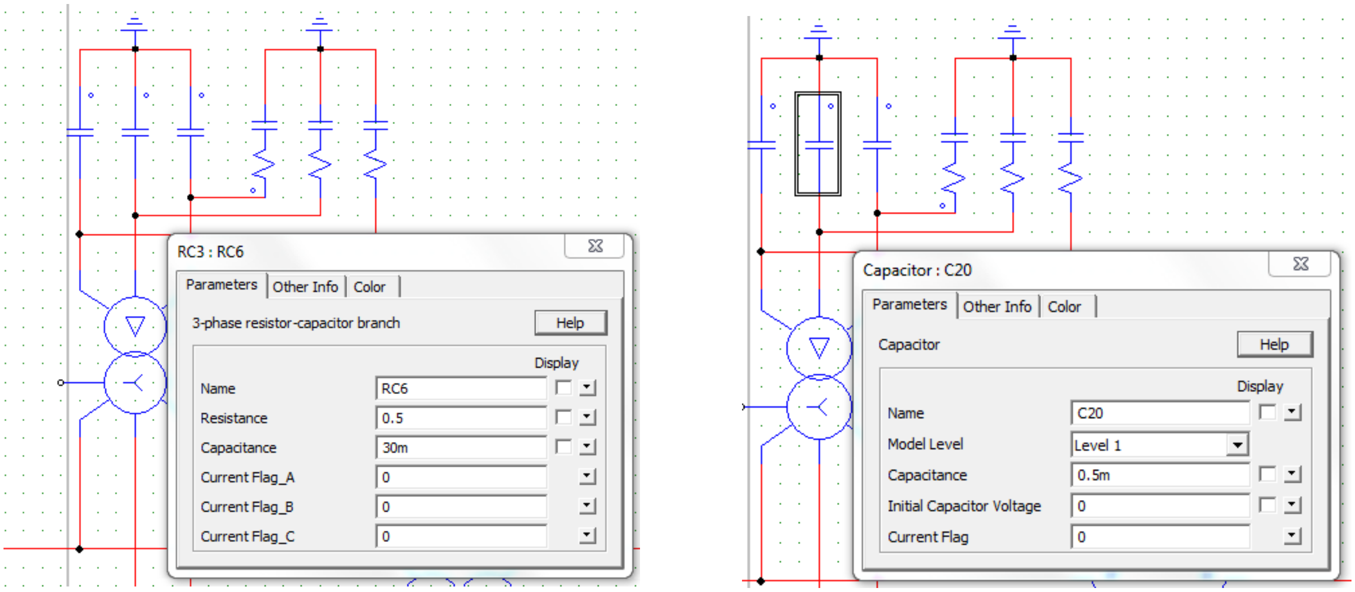

3-phase resistor-capacitor branch

Name	RC6
Resistance	0.5
Capacitance	30m
Current Flag_A	0
Current Flag_B	0
Current Flag_C	0

Capacitor

Name	C20
Model Level	Level 1
Capacitance	0.5m
Initial Capacitor Voltage	0
Current Flag	0

Figure 4.9: AC filters implementation in psim.

CHAPTER 5: CONTROLLER DESIGN

The detailed modelling of the system has been carried out in chapter 2 and chapter 3. This chapter presents the controller design of building from the detailed mathematical models already derived. The controllers for the MSC: inner loop and outer loop are first presented. Thereafter, the controllers for the GSC: inner loop and outer loops are presented. The PI-controllers are designed in Matlab using the PID built in tool.

5.1 MSC controller design

The MSC controllers have two loops: inner loop which is made up of a current loop and the outer loop which is made up of the V_{dc} controller and the ac controller.

5.1.1 Inner current loop

The final mathematical model as derived in chapter 3 is:

$$A = \begin{bmatrix} \frac{-R_s}{L_{sd}} & 0 \\ 0 & \frac{-R_s}{L_{sq}} \end{bmatrix} \tag{5.1}$$

$$B = \begin{bmatrix} \frac{1}{L_{sd}} & 0 & 0 \\ 0 & 0 & 0 \end{bmatrix} \tag{5.2}$$

$$C = \begin{bmatrix} 1 & 0 \end{bmatrix} \tag{5.3}$$

$$D = \begin{bmatrix} 0 \end{bmatrix} \tag{5.4}$$

Matlab software is used to obtain the system’s transfer function given in Eq. 5.5 below. The detailed coding is available on the Appendix A.

$$T_{inner\_open} = \frac{635.7}{s + 0.5219} \tag{5.5}$$

Then, the closed loop is:

$$T_{inner\_closed} = \frac{635.7s + 331.8}{s^2 + 636.7s + 332} \tag{5.6}$$

Therefore, this closed loop is then imported to the pidtoool design space using the matlab command: pid(T_{inner_closed}). Table 5.1 shows the un-tuned parameters and figure 5.1 shows the step response of the system. The control design approach here is to set the outer loop to be slower than the inner loop so that the reference signal can be readily available for the outer controller when it starts working.

Table 5-1: The open loop response of the inner current loop parameters

Gain, K_p	0.00085572
Integrator gain, K_i	0.024097
Rise time	0.0863 s
Settling time	0.315 s
Overshoot	13.8 %
Peak	1.14
Phase Margin	60 deg @16.7 rad/s
Closed-loop	stable

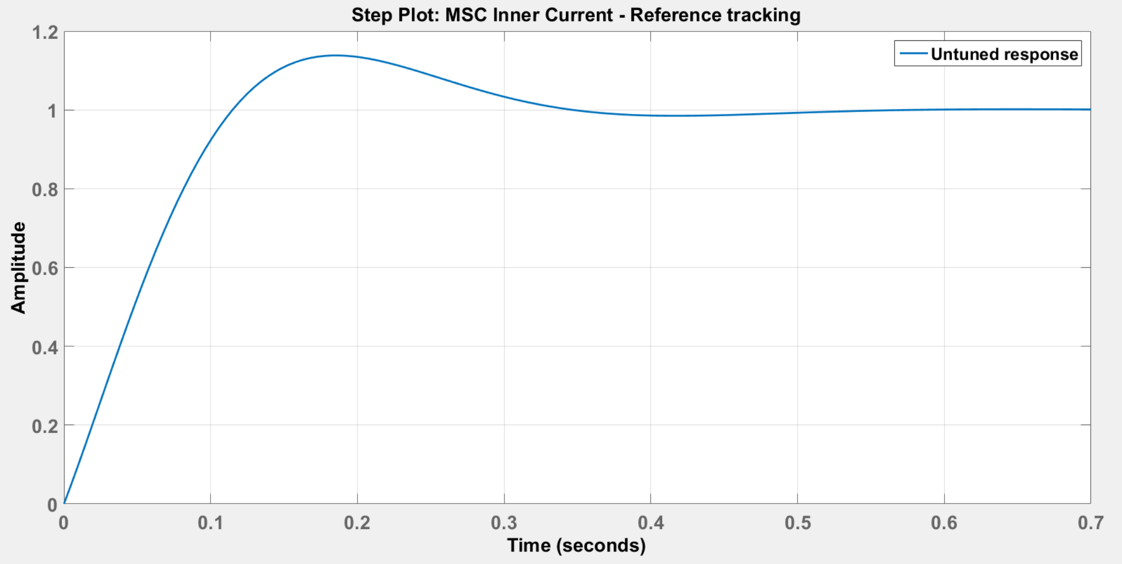

Figure 5.1: The open loop response of the MSC inner current loop

From the information in table 5.1 and figure 5.1, the inner current loop is tuned such that the rise time is slower than that of the outer controllers. The achieved results are presented in table 5.2 and figure 5.2 below.

Table 5-2: The Inner current loop parameters due to PID tunning

Gain, K_p	3.1981
Integrator gain, K_i	2046.3904
Rise time	500.72 ms
Settling time	900.22 ms
Overshoot	1.54 %
Peak	1.02
Phase Margin	89 deg @ 30.66x10^3 rad/sec
Closed-loop	stable

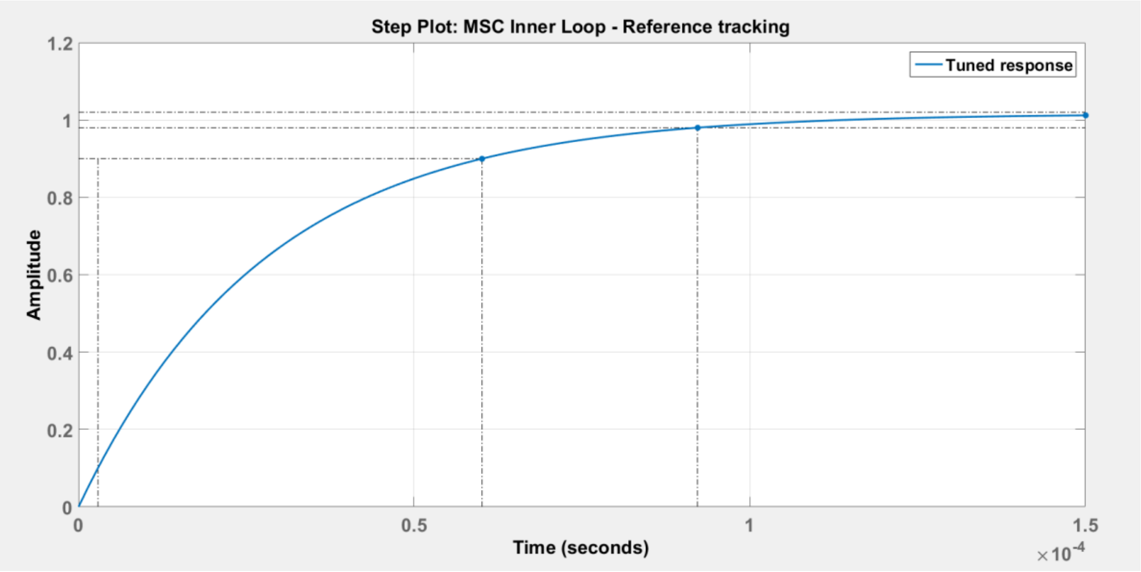

Figure 5.2: Step response of the MSC inner current loop due to PID control

5.2 Outer Current Controller

These controllers must have almost the same time response so that they would simultaneously provide the reference signals to the inner loop at the time it is required as set out.

The closed loop of the inner current loop with the tuned response included is:

$$T_{tuned\_inner\_closed} = \frac{2033s^3 + 1.302\times10^6 s^2 + 6.789\times10^5 s}{s^4 + 2034s^3 + 1.302\times10^6 s^2 + 6.789\times10^5 s} \tag{5.7}$$

5.2.1 DC-Link voltage control

Designing a DC-link controller for a full converter is very challenging. The control objective is not only to track the reference but also to reject the disturbances during power production changes and keep the dc-voltage stable.

The initial un-tuned response parameters are shown in table 5.3 and figure 5.3 below. The control approach here is to coordinate the time response of the controller so as to provide the signal to the inner loop at the same time. This is very important.

The DC voltage transfer function closed loop developed using the actual voltage values to design the controller is:

$$T_{dc} = \frac{24.05s^8 + 6.432\times10^4 s^7 + 6.265\times10^7 s^6 + 2.009\times10^{10} s^5 + 2.091\times10^{10} s^4 + 5.453\times10^9 s^3}{\begin{pmatrix} 1.399\times10^{-4} s^{10} + 0.5693s^9 + 967.5s^8 + 8.058\times10^5 s^7 \\ +3.003\times10^8 s^6 + 2.033\times10^{10} s^5 + 2.098\times10^{10} s^4 + 5.453\times10^9 s^3 \end{pmatrix}} \tag{5.8}$$

Table 5-3: The open loop response of the DC-link voltage control

Gain, K_p	1.0308
Integrator gain, K_i	263.7206
Rise time	9.27 ms
Settling time	35.0 ms
Overshoot	13.6 %
Peak	1.14
Phase Margin	60 deg @ 151 rad/s
Closed-loop	stable

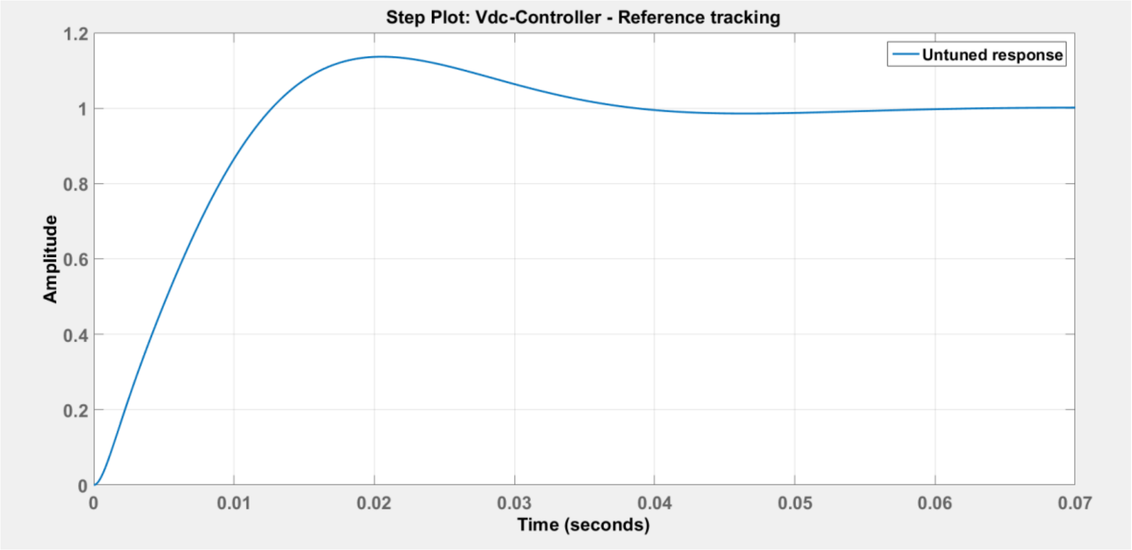

Figure 5.3: The open loop step response of the V_{dc}- control loop

From the information given by table 5.4 and figure 5.4 below, the time response for the inner loop is 500.72 ms and that of the V_{dc}-controller is 24.2 ms. This is adequate for the required reference to be provided on time for the inner loop. The settling times are 900.22 ms and 79.0 ms for the inner current loop and the V_{dc}-controller respectively. The tuned response is satisfactory to the control objective for this system.

Table 5-4: DC-link voltage control parameters due to PID control

Gain, K_p	4.6
Integrator gain, K_i	364
Rise time	24.2 ms
Settling time	79.0 ms
Overshoot	10.6%
Peak	1.11
Phase Margin	58 deg @ 54.9 rad/s
Closed-loop	stable

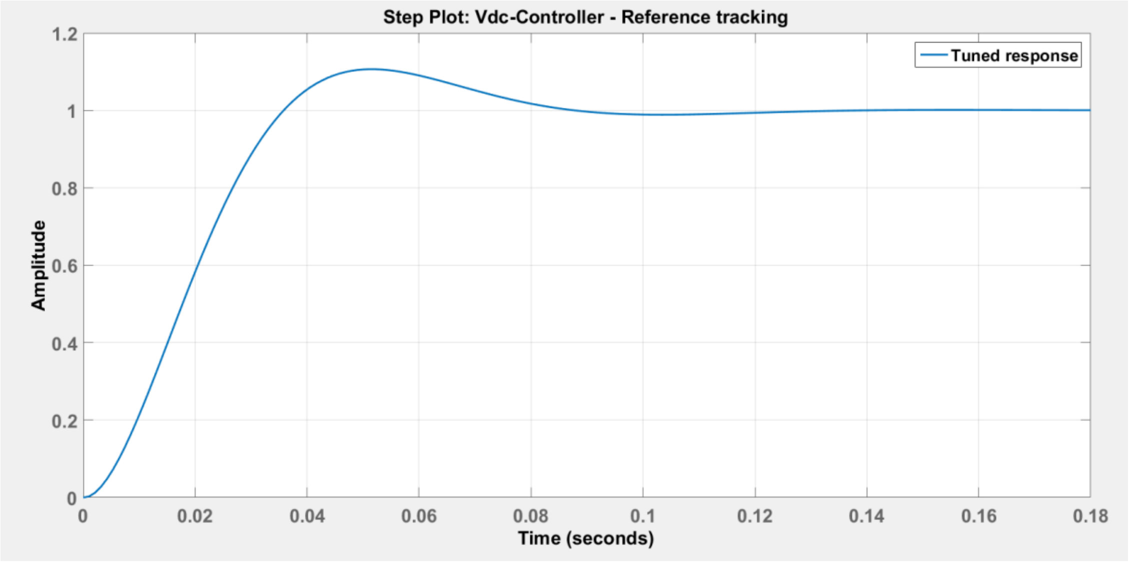

Figure 5.4: Step response of the V_{dc}- due to the PID control

5.2.2 Stator Voltage control

This controller should match the time response of the V_{dc}-controller so that at the end, there are able to provide the reference signals for the inner controller on time simultaneously. Table 5.5 and figure 5.5 show the initial un-tuned parameters for the ac voltage controller.

The ac voltage closed loop transfer function is:

$$T_{ac} = \frac{36.08s^8 + 9.648\times10^4 s^7 + 9.397\times10^7 s^6 + 3.013\times10^{10} s^5 + 3.137\times10^{10} s^4 + 8.18\times10^9 s^3}{\begin{pmatrix}1.861\times10^{-5} s^{10} + 7.571\times10^{-2} s^9 + 128.7s^8 + 1.071\times10^5 s^7 \\ +3.993\times10^7 s^6 + 2.704\times10^9 s^5 + 2.79\times10^9 s^4 + 7.251\times10^8 s^3\end{pmatrix}} \tag{5.9}$$

This closed loop is then imported to the matlab pidtool workspace. It is then tuned according to meet the objectives.

Table 5-5: Open loop stator voltage control parameters

Gain, K_p	0.091378
Integrator gain, K_i	23.3789
Rise time	9.27 ms
Settling time	35.0 ms

Overshoot	13.6 %
Peak	1.14
Phase Margin	60 deg @ 151 rad/s
Closed-loop	stable

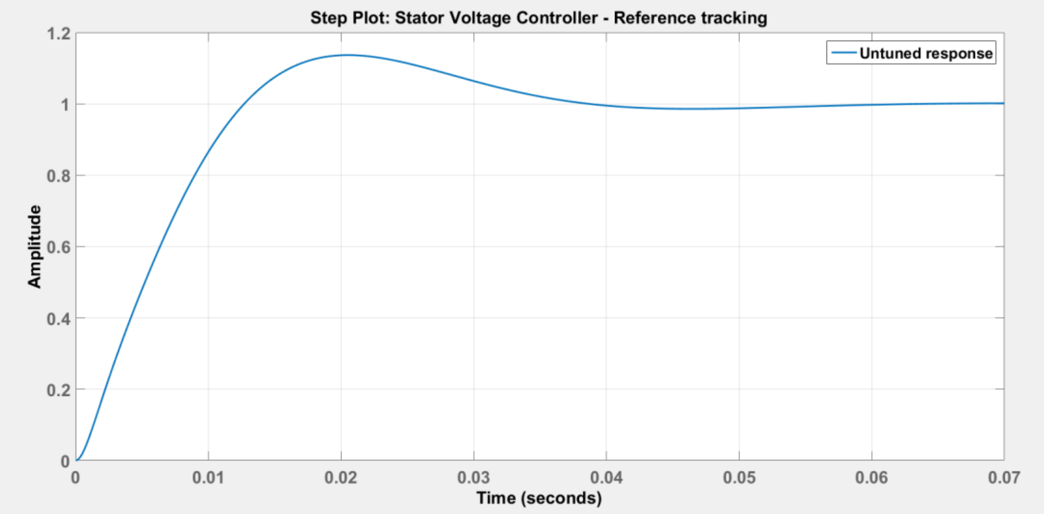

Figure 5.5: The open loop step response of the ac voltage control loop

From the information given in table 5.6 and figure 5.6 below, the time response for the inner loop is 500.72 ms and that of the V_{ac}-controller is 21.8 ms. This is adequate for the required reference to be provided on time for the inner loop. The settling times are 900.22 ms and 59.0 ms for the inner current loop and the V_{ac}-controller respectively.

Table 5-6: Stator voltage control parameters due to the PID control

Gain, K_p	0.10415
Integrator gain, K_i	8.8497
Rise time	21.8 ms
Settling time	59.1 ms
Overshoot	0 %
Peak	1
Phase Margin	90 deg @ 99.9 rad/s
Closed-loop	stable

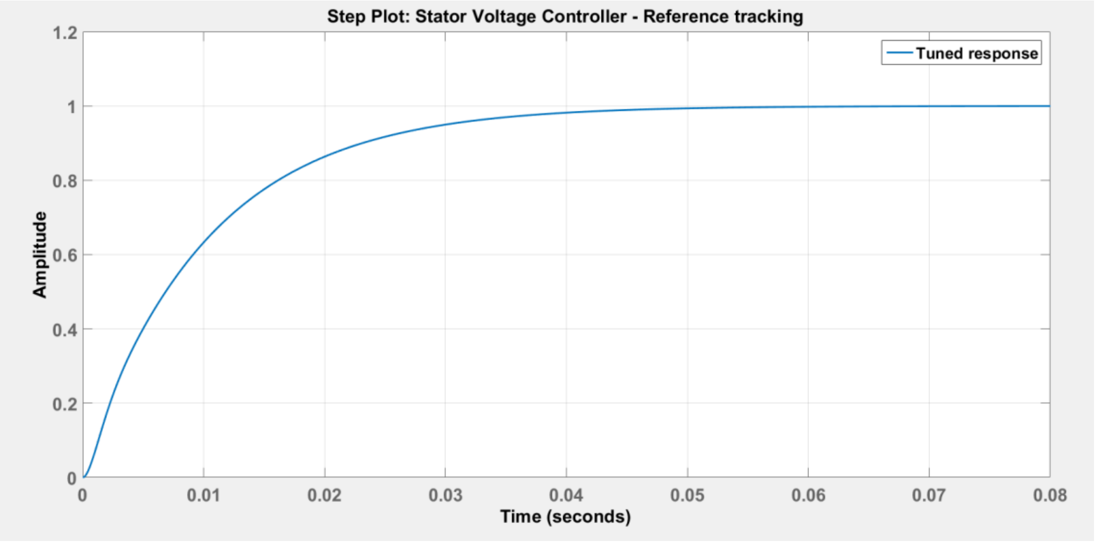

Figure 5.6: The PID controlled step response of the *ac voltage* control loop

5.3 GSC controller design

The GSC controllers have two loops: inner loop which is made up of a current loop and the outer loop which is made up of the MPPT power controller and the reactive power controller.

5.3.1 Inner current loop

The final mathematical model as derived in chapter 3 is:

$$A = \begin{bmatrix} \dfrac{-R_g}{L_{gd}} & 0 \\ 0 & \dfrac{-R_g}{L_{gq}} \end{bmatrix} \tag{5.10}$$

$$B = \begin{bmatrix} \dfrac{1}{L_{gd}} & 0 & 0 \\ 0 & 0 & 0 \end{bmatrix} \tag{5.11}$$

$$C = [1 \quad 0] \tag{5.12}$$

$$D = [0] \tag{5.13}$$

Matlab software is used to obtain the system's transfer function given in Eq. 5.14 below. The detailed coding is available on the Appendix B.

$$T_{inner\_open} = \frac{11430}{s + 9.383} \tag{5.14}$$

Then, the closed loop is:

$$T_{inner\_closed} = \frac{11430\, s \; + \; 1.072 \cdot 10^{5}}{s^{2} + 1.145 \cdot 10^{4}\, s + 1.073 \cdot 10^{5}} \tag{5.15}$$

Therefore, this closed loop is then imported to the pidtoool design space using the matlab command: pid(T_{inner_closed}). Table 5.7 shows the un-tuned parameters and figure 5.7 shows the step response of the system. The control design approach here is to set the outer loop to be quicker than the inner loop so that the reference signal for the inner loop can be readily available for the inner controller when it starts working.

Table 5-7: Open loop parameters for the inner current loop control

Gain, K_p	0.00085572
Integrator gain, K_i	0.024097
Rise time	86.3 ms
Settling time	315.0 ms
Overshoot	13.8 %
Peak	1.14
Phase Margin	60 deg @ 16.7 rad/s
Closed-loop	stable

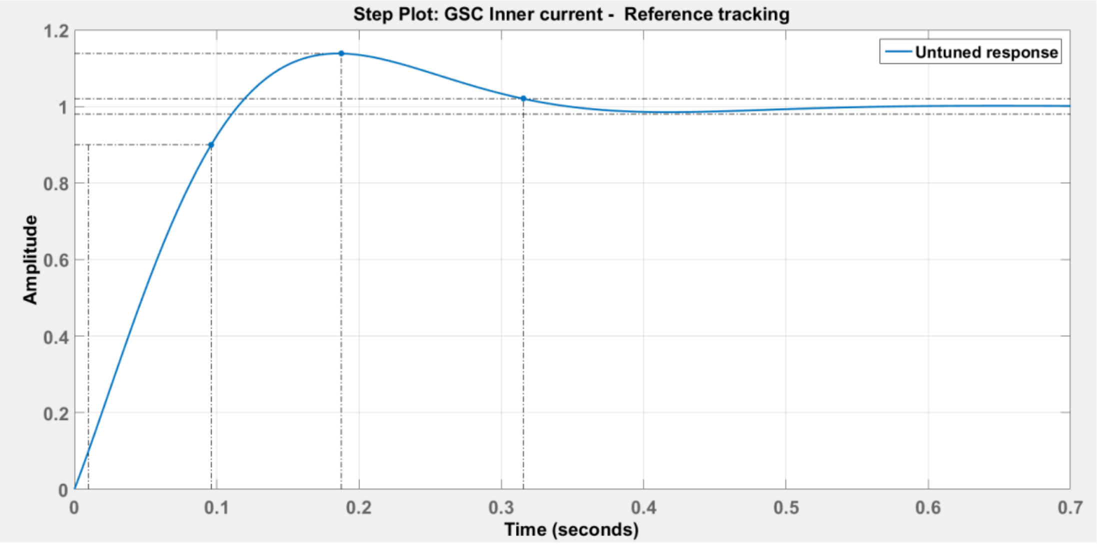

Figure 5.7: The open loop step response of the GSC Inner current control loop

From the information in table 5.7 and figure 5.7, the inner current loop is tuned such that the rise time is slower than that of the outer controllers. The achieved results are presented in table 5.8 and figure 5.8 below

Table 5-8: Inner current loop control parameters due to PID control

Gain, K_p	3.5067
Integrator gain, K_i	2460.3024
Rise time	522 ms
Settling time	841.0 ms
Overshoot	1.54 %
Peak	1.02
Phase Margin	89 deg @ 401×10^3rad/s
Closed-loop	stable

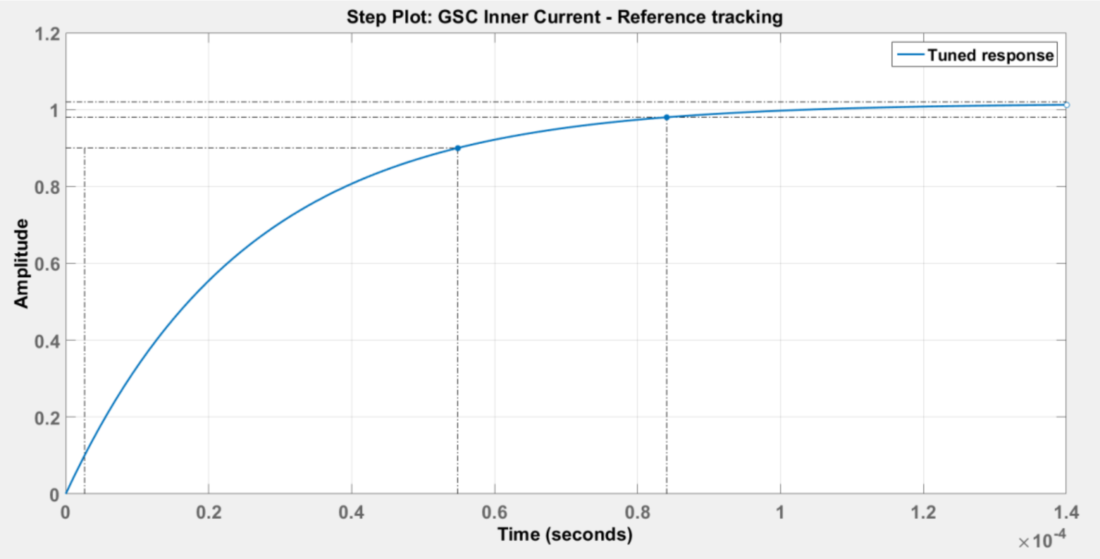

Figure 5.8: The PID controlled step response of the GSC Inner current control loop

5.4 Outer current control loop

These controllers must have almost the same time response so that they would simultaneously provide the reference signals to the inner loop at the time it is required as set out.

The closed loop of the inner current loop with the tuned response included is:

$$T_{tuned\_inner\_closed} = \frac{2.55\times10^{9}s^{3}+2.393\times10^{10}s^{2}+1.109\times10^{8}s}{s^{4}+2.55\times10^{9}s^{3}+2.393\times10^{10}s^{2}+1.109\times10^{8}s} \tag{5.16}$$

5.4.1 Active Power controller

The control objective for the active power controller is to track the reference. The initial un-tuned response parameters are shown in table 5.9 and figure 5.9 below. The control approach here is to coordinate the time response of the controller so as to provide the reference signal to the inner loop at the same time. This is very important.

The active power transfer function closed loop used to design the controller is:

$$T_{active\_power}=\left(\frac{\left(\begin{array}{l}2.027\times10^{12}s^{7}+5.168\times10^{21}s^{6}+9.703\times10^{22}s^{5}\\+4.559\times10^{23}s^{4}+4.219\times10^{21}s^{3}+9.773\times10^{18}s^{2}\end{array}\right)}{\begin{array}{l}s^{8}+2.032\times10^{12}s^{7}+5.174\times10^{21}s^{6}+9.715\times10^{22}s^{5}\\+4.564\times10^{23}s^{4}+4.225\times10^{21}s^{3}+9.786\times10^{18}s^{2}\end{array}}\right) \tag{5.17}$$

Table 5-9: Open loop control parameters for the active power control parameters

Gain, K_p	1.1903
Integrator gain, K_i	114688482.3314
Rise time	0.023 µs
Settling time	0.0859 µs
Overshoot	14.3 %
Peak	1.14
Phase Margin	60 deg @ 622x10^6 rad/s
Closed-loop	stable

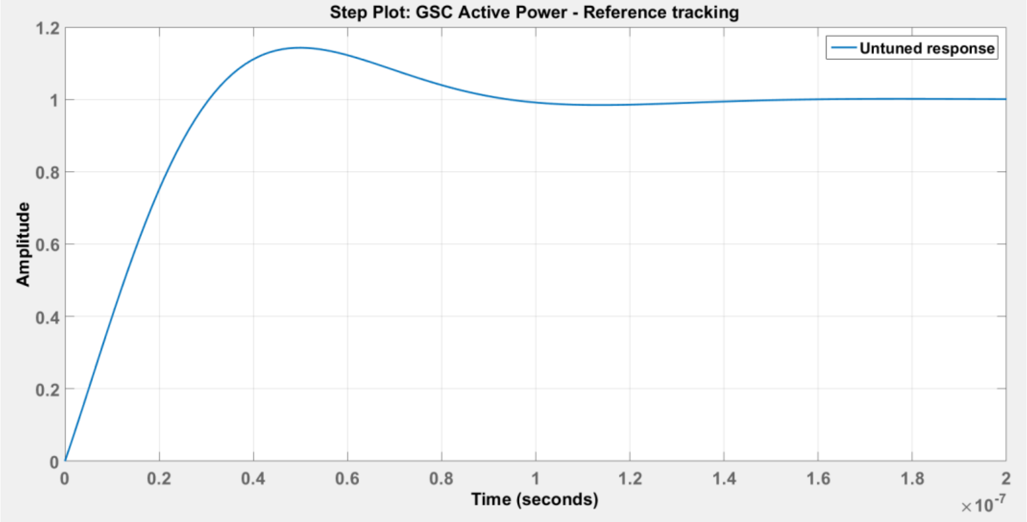

Figure 5.9: The open loop step response of the GSC active power control loop

From the information given by table 5.10 and figure 5.10 below, the time response for the inner loop is 522.00 ms and that of the active power controller is 21.30 ms. This is adequate for the required reference signal to be provided on time for the inner loop. The settling times are 841.02 ms and 37.90 ms for the inner current loop and the active power controller respectively. The tuned response is satisfactory to the control objective for this system.

Table 5-10: The Active power control parameters due to PID control

Gain, K_p	2.2306 ×105
Integrator gain, K_i	1033.8281
Rise time	21.3 ms
Settling time	37.9 ms
Overshoot	0 %
Peak	1.0
Phase Margin	90 deg @ 1.03x10^3 rad/s
Closed-loop	stable

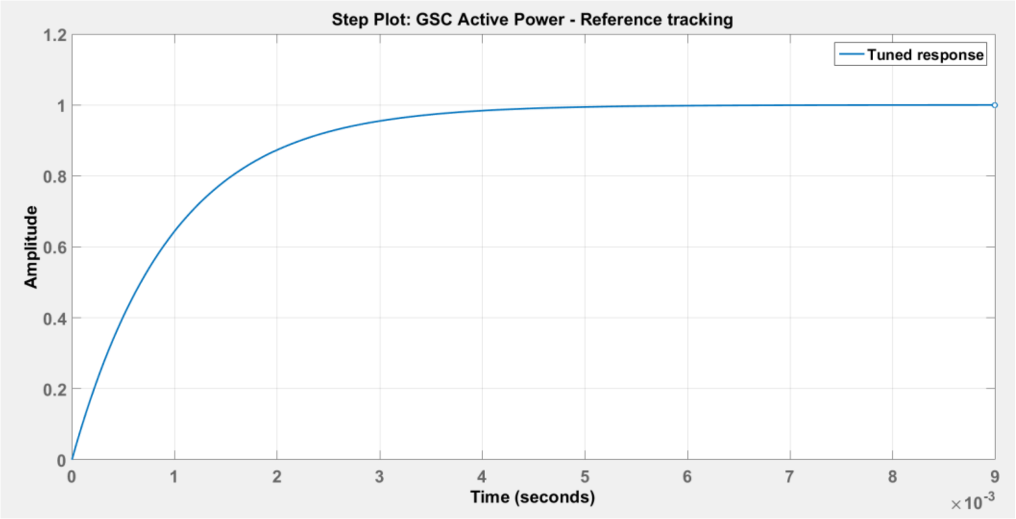

Figure 5.10: The PID controlled step response of the GSC active power control loop

5.4.2 Reactive power Control

This controller should match the time response of the MPPT power controller so that at the end, there are able to provide the reference signals for the inner controller on time simultaneously. Table 5.11 and figure 5.11 show the initial un-tuned parameters for the reactive controller.

The reactive power control closed loop transfer function is:

$$T_{reactive\_power} = \frac{\begin{pmatrix} 2.027\times10^{12}s^{7} + 5.168\times10^{21}s^{6} + 9.703\times10^{22}s^{5} \\ +4.559\times10^{23}s^{4} + 4.219\times10^{21}s^{3} + 9.773\times10^{18}s^{2} \end{pmatrix}}{\begin{pmatrix} s^{8} + 2.032\times10^{12}s^{7} + 5.174\times10^{21}s^{6} + 9.715\times10^{22}s^{5} \\ +4.564\times10^{23}s^{4} + 4.225\times10^{21}s^{3} + 9.786\times10^{18}s^{2} \end{pmatrix}} \tag{5.18}$$

This closed loop is then imported to the matlab pidtool workspace. It is then tuned accordingly to meet the control objectives.

Table 5-11: Open loop control parameters for the reactive power

Gain, K_p	1.1903
Integrator gain, K_i	114688482.3314
Rise time	0.023 µs
Settling time	0.0859 µs
Overshoot	14.3 %
Peak	1.14
Phase Margin	60 deg @ 622x10^{6} rad/s
Closed-loop	stable

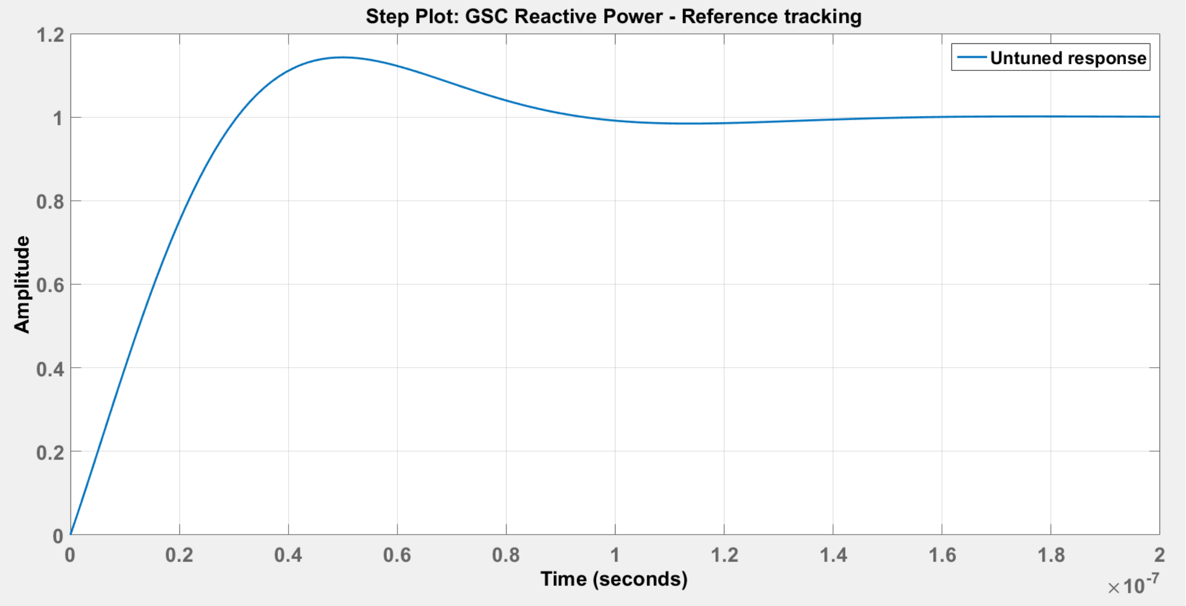

Figure 5.11: The open loop step response of the GSC reactive power control loop

From the information given by table 5.12 and figure 5.12 below, the time response for the inner loop is 522.00 ms and that of the reactive power controller is 21.30 ms. This is adequate for the required reference signal to be provided on time for the inner loop. The settling times are 841.02 ms and 37.90 ms for the inner current loop and the active power controller respectively. The tuned response is satisfactory to the control objective for this system.

Table 5-12: Reactive power control parameters due to PID control

Gain, K_p	2.2306 x105
Integrator gain, K_i	1033.8281
Rise time	21.3 ms
Settling time	37.9 ms
Overshoot	0%
Peak	1.0
Phase Margin	90 deg @ 1.03x10^3 rad/s
Closed-loop	stable

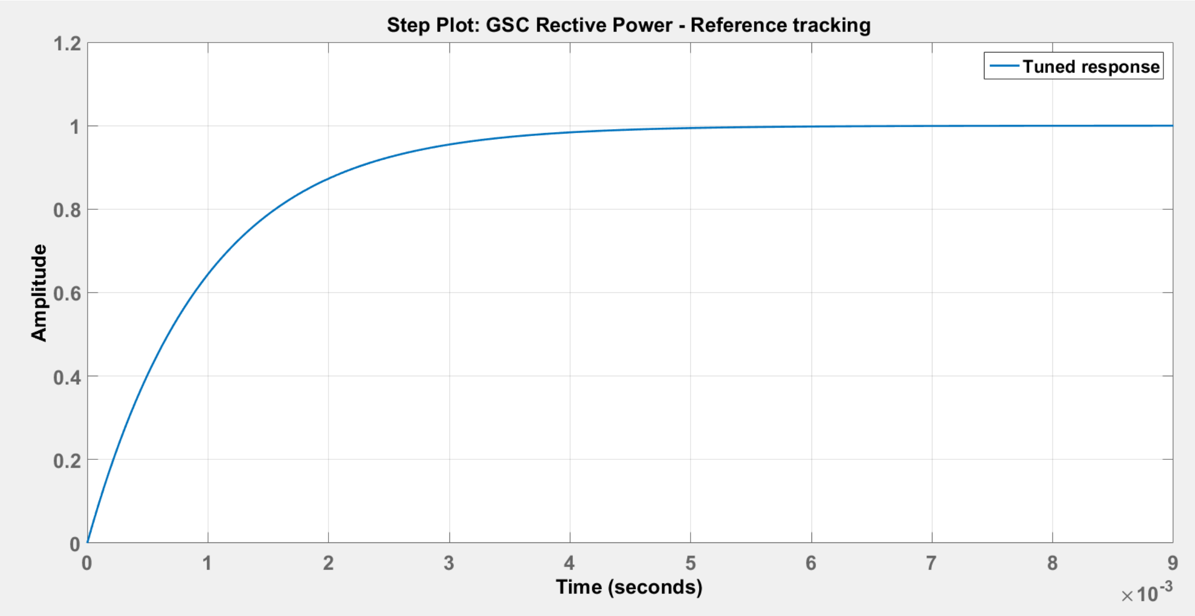

Figure 5.12: The PID controlled step response of the GSC reactive power control loop

5.4.3 Pitch angle control

The control objective for the pitch controller is to track the reference and maintain an optimal pitch angle. The initial un-tuned response parameters are shown in table 5.13 and figure 5.13 below.

The pitch angle transfer function closed loop used to design the controller is:

$$T_{pitch} = \frac{816180}{625s^2 + 6450s + 2000} \tag{5.17}$$

Table 5-13: Open loop control parameters for the pitch angle

Gain, K_p	0.0028098
Integrator gain, K_i	0.0026984
Rise time	2.53 s
Settling time	9.25 s
Overshoot	13.8 %
Peak	1.14
Phase Margin	60 deg @ 0.57 rad/s
Closed-loop	stable

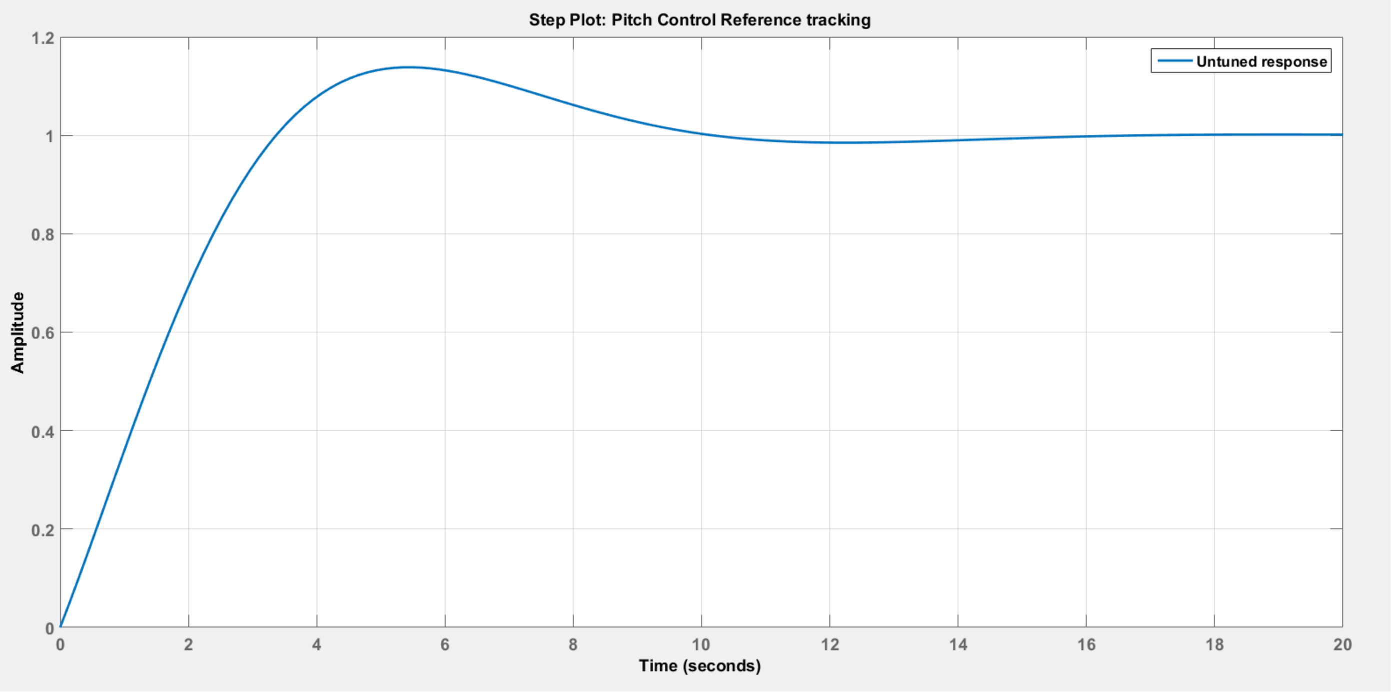

Figure 5.13: The open loop step response of the pitch angle control loop

From the information given by table 5.14 and figure 5.14 below, the time response for the pitch angle system is 2.3 ms. This achieves the control objective.

Table 5-14: Pitch angle control parameters due to PID control

Gain, K_p	4.3509
Integrator gain, K_i	1156.2996
Rise time	2.3 ms
Settling time	13 ms
Overshoot	16.1%
Peak	1.21
Phase Margin	65 deg @ 570 rad/s
Closed-loop	stable

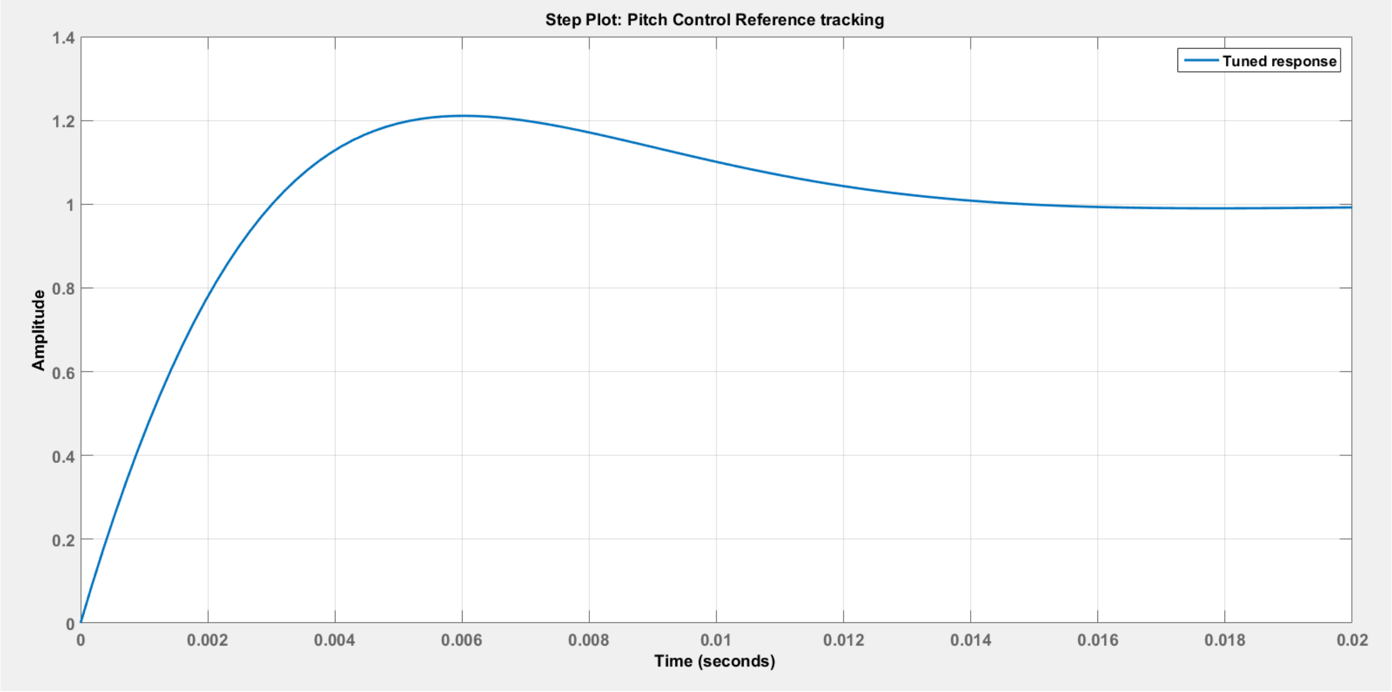

Figure 5.14: The PID controlled step response of the pitch angle

CHAPTER 6: PRESENTATION AND DISCUSSIONS

This chapter presents the results obtained from simulating the wind system. Detailed discussions and analysis are carried out on the results to understand them. Where the result contains some important observations or points, it is re-simulated at the reference point and further solid deductions are made where possible.

6.1 Wind Turbine Results

The wind is simulated by varying the input values to the turbine system model in Psim software. This then serves to represent the wind speed in real life. It does not purely reflect the full practical behaviour of the wind hence the results vary to the practical one or with other software packages that take into consideration the wind distribution: extreme wind, wind shear, wake turbulence, flow inclination, wind distribution and turbulence intensity see figure 6.1 for details.

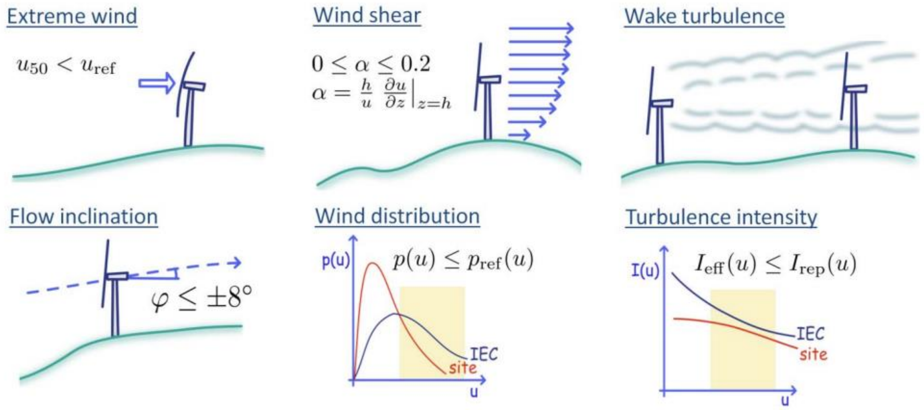

Figure 6.1: Distribution of wind flow as a function of height

6.1.1 Wind data in South Africa

Eastern Cape Province in South Africa has been selected as the focus area for this research. This is because currently there are 13 wind turbine farms installed in the country and fully in operation. Then six (46%) of these wind farms are in Eastern Cape hence selected.

The average wind speed in the Eastern Cape from the wind data is approximately 6 m/s and it is taken as the reference wind speed to give a good predication of the expected power to be harvested from the wind in the province. For the upper wind behaviour, a wind speed of 11 m/s has been selected based from the wind data provided.

The wind speed is varied from 6 m/s at the start to 11 m/s at 1s. Since practically the wind does not change instantaneously, the acceralation of the wind is set to:

$$a = \frac{v_f - v_i}{t_f - t_i} \tag{6.1}$$

The change between the final speed V_f and the initial speed V_i is divided by the change between the final time t_f and the initial time t_i .

Hence,

$$a = \frac{11-6}{1.1-1.0} = 50 \text{ m/s}^2 \tag{6.2}$$

Figure 6.2 shows the wind speed profile for the system in this project.

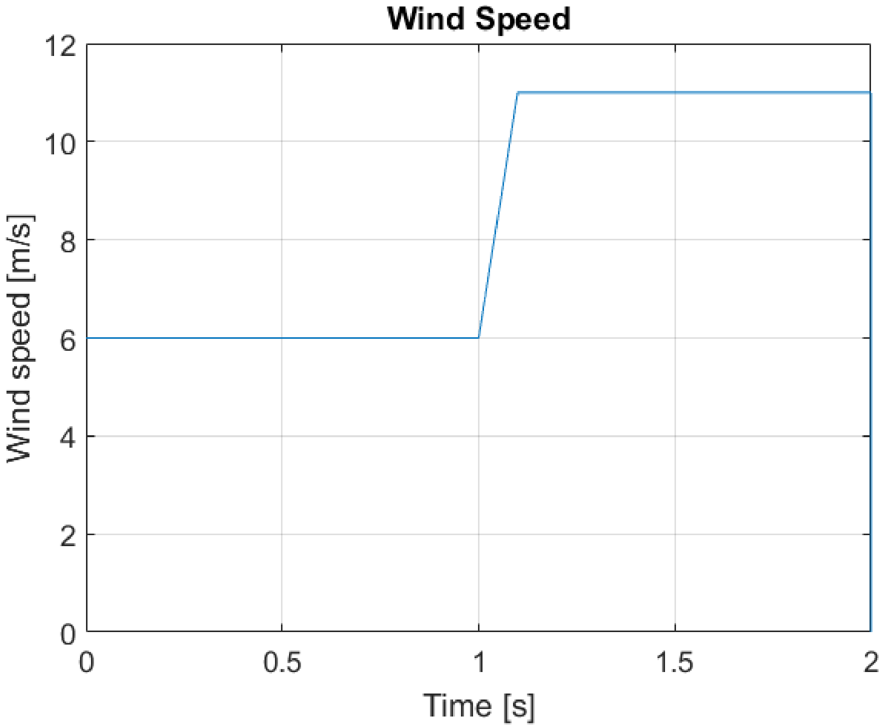

Figure 6.2: Wind speed for the wind energy conversion system being simulated in Psim software

6.1.2 Mechanical angular speed

The rotor responds to the wind speed at the beginning of the simulations as shown in figure 6.3 below. It ramps to 0.885 rad/s then gradually settles down around 0.755 rad/s for the 6 m/s wind speed. At 1*s*, it responds to the change in wind speed by increasing at a rate complimenting that of the wind speed. It then settles to its new value at 0.891 rad/s as expected.

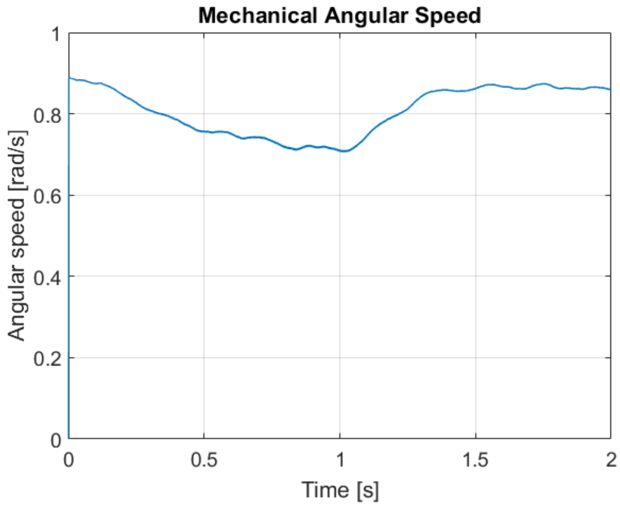

Figure 6.3: The simulated angular speed when the wind speed is varied

It cannot be distinctly deduced that the angular speed settles down as shown in figure 6.4 for the 6 m/s wind speed. To verify the observation, a second simulation is carried out with the reference speed of the research, 6 m/s, see figure 6.4. It can now be solidly deduced that the angular speed repositions itself to settle at the 0.755 rad/s speed when the wind speed is at 6 m/s and it has not been changed throughout the simulation period.

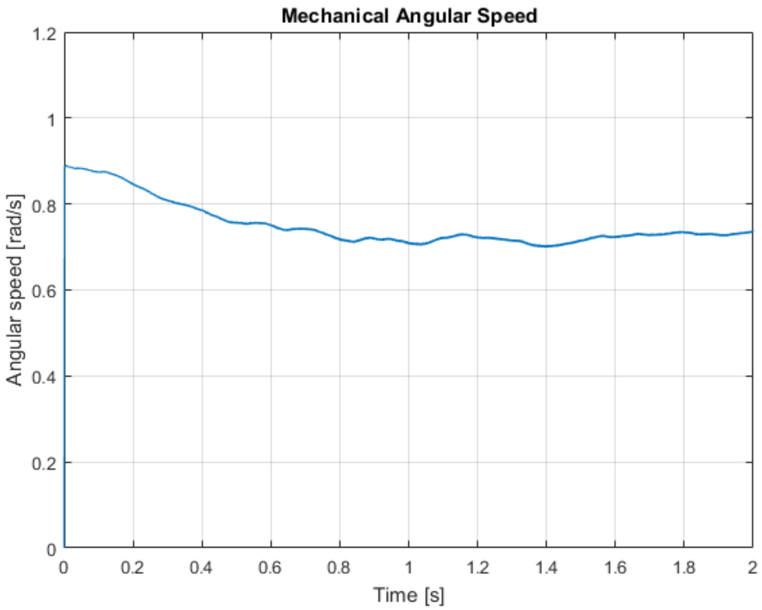

Figure 6.4: The simulated angular speed at constant wind speed of 6 m/s

6.2 PMSG Results

The angular speed serves as a control variable to the generator. Therefore, the generator upon receiving the command from the angular speed, it starts to generate the power as demonstrated in the figure 6.5 below.

6.2.1 PMSG Power system curve

The initial power produced at the speed of 6 m/s has ripples in the first 0.25s due to machine dynamics but the controller quickly settles it thereafter. Practically, generators are run for a period of time before they are synchronised to the grid. This enables them to reach synchronism levels at steady states hence avoid the grid system from receiving distorted generators' outputs such as voltage, frequency, current etc. These distorted generators' outputs may propagate through the grid system which may cause it to collapse. The reactive power ramps up at the beginning to support for the voltage being produced. It then gradually reduces to approximately zero when the machine has fully settled and the voltage is stable. Since it is not very clear that the reactive power does settle down in figure 6.6, Second simulations at the 6 m/s reference points are carried out and figure 6.6 shows the results. It is clear that the reactive power does settle down after establishing a constant voltage.

The wind speed is varied from 6 m/s to 11 m/s at t = 1s. The active power increases gradually as it responds to the change in wind speed. At t = 1s, the reactive power increases again to keep the voltage from increasing up as the power generated increases. Eq.6.3 shows the linear relationship between the active power P, reactive power Q, apparent power S, voltage V, and current I. So the voltage is linearly proportional to P, therefore an increase to P forces the voltage and current to increase. Since the voltage needs to be kept constant, the reactive power compensates for this by increasing so as to keep the voltage constant. At the end, it's the current which increases symmetrically to the active power.

$$S = VI \tag{6.3}$$

$$\begin{aligned} P &= VI\cos\theta \\ Q &= VI\sin\theta \end{aligned} \tag{6.4}$$

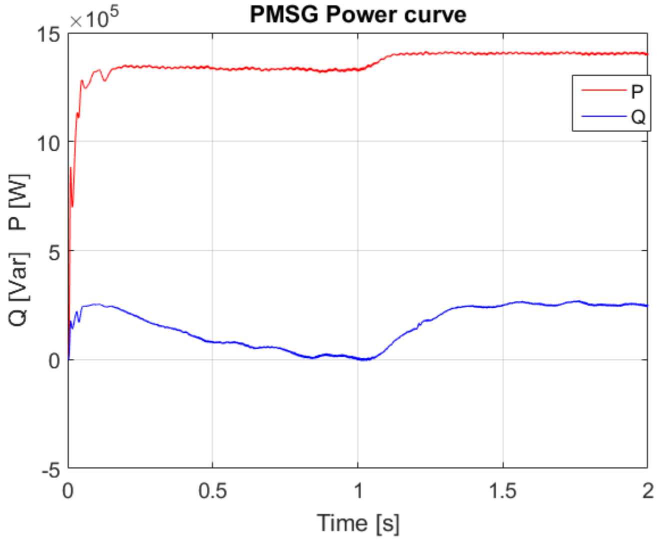

Figure 6.5: PMSG simulated power curve with the wind speed varied

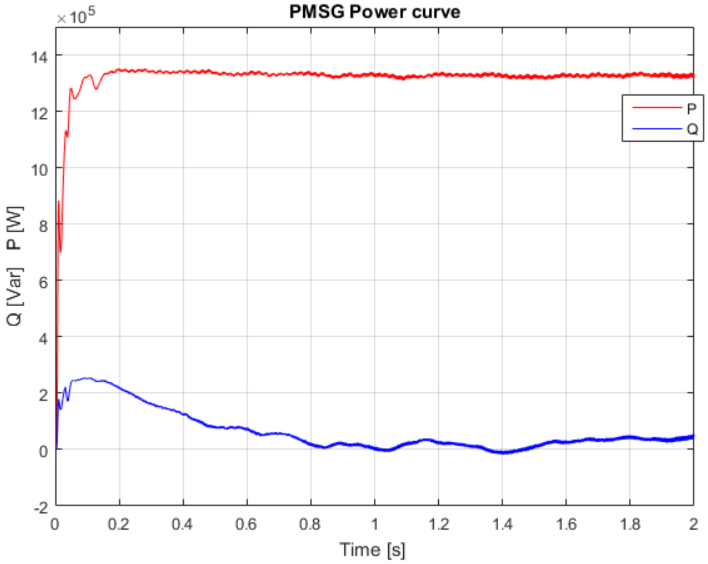

Figure 6.6: PMSG simulated power curve with the wind speed constant at 6 m/s

For the wind speed of 6 m/s, the measured active power and reactive power at t = 0.974s is P =1.326 MW and Q = 14.38 kVAr respectively. Therefore, the power factor ($p.f$) is:

$$Q = P\tan\theta$$

$$\tan\theta = \frac{Q}{P} \tag{6.5}$$

$$\theta = \tan^{-1}\left(\frac{14.38 \text{ kVAr}}{1.326 \text{ MW}}\right)$$

$$\therefore \cos\theta = 0.9999$$

According to the datasheet, the rated power factor, *p.f* = 0.8921. It can be solidly deduced that the VSC is able to improve consistently the power factor of the stator transmission side to approximately 0.9999.

Similarly, for the wind speed of 11 m/s, the measured active power and reactive power at *t* = 1.975s is *P* =1.410 MW and *Q* = 0.2523 MVAr respectively. Therefore, the power factor (*p.f*) is:

$$Q = P\tan\theta$$

$$\tan\theta = \frac{Q}{P} \tag{6.6}$$

$$\theta = \tan^{-1}\left(\frac{0.2523\ \text{MVAr}}{1.410\ \text{MW}}\right)$$

$$\therefore \cos\theta = 0.9841$$

This shows a power factor of 0.9841 which is much better than the rated one of 0.8921. This underlines the importance of the VSC function in helping the system cope with voltage support.

6.2.2 PMSG Electrical Torque

The electromagnetic torque produced by the generator at steady state is equal and opposite in direction to the mechanical one. The electromagnetic torque as developed in detail from chapter 2 is:

$$T_e = \frac{3}{2}p\left[i_{sq}\psi_{PM}\right] \tag{6.7}$$

It can be deduced from Eq.6.7 that the electromagnetic torque varies directly proportional to the q-component of the stator current. This relationship is observed from the graphs below: figure 6.7 and figure 6.8.

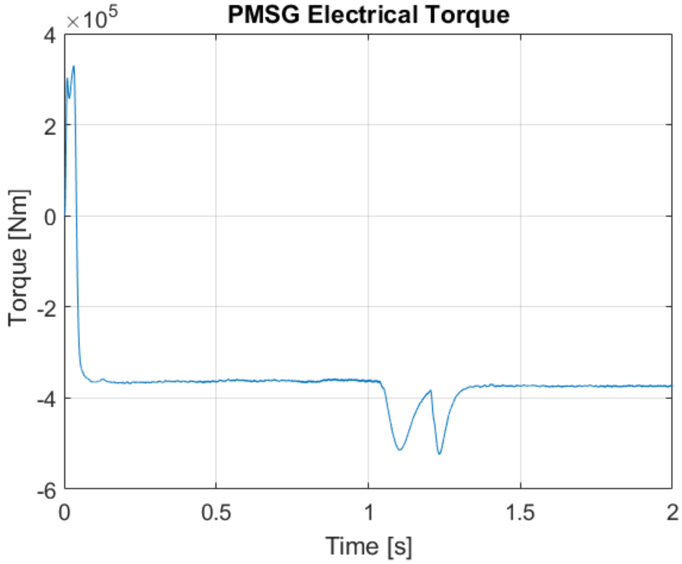

Figure 6.7: PMSG simulated electromagnetic torque curve

6.2.3 Stator dq-component Currents

The controller tracking performance is investigated using the stator *dq* currents in figure 6.8. The controller starts with a small overshoot then keeps full tracking throughout the period leading to 1*s*. The under-current before *t* = 1s in the graph is due to the lower power production at wind speed 6 m/s; hence, lower current. At *t* =1s, the power production increases so the controller firstly losses track of the reference, but it quickly responds and finds the reference. Thereafter it perfectly tracks the reference current as the power production has increased and so is the current hence there are matching.

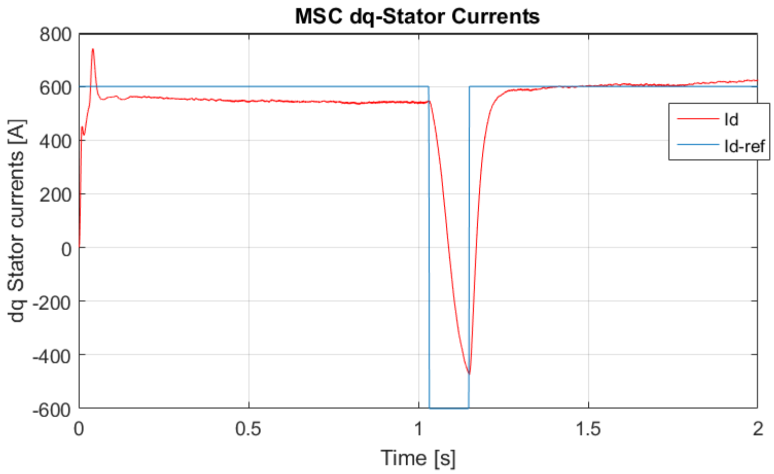

Figure 6.8: The simulated stator current *d*-component

The same explanation extends to the I_q current. The reference ($I_{q\text{-}ref}$) remains constant throughout even at *t* = 1s because the stator voltage is constant. The under-current before *t* = 1s in the graph is due to the lower power production at wind speed 6 m/s; hence, lower current. At t =1s, the power production increases so the controller firstly losses track of the reference, but it quickly responds and finds the reference. The responds time is equivalent to the time it takes the reactive power to settle down. Thereafter it perfectly tracks the reference current as the power production has increased and so is the current hence there are matching. The spike is due to the changes in the reactive power; see fig. 6.9.

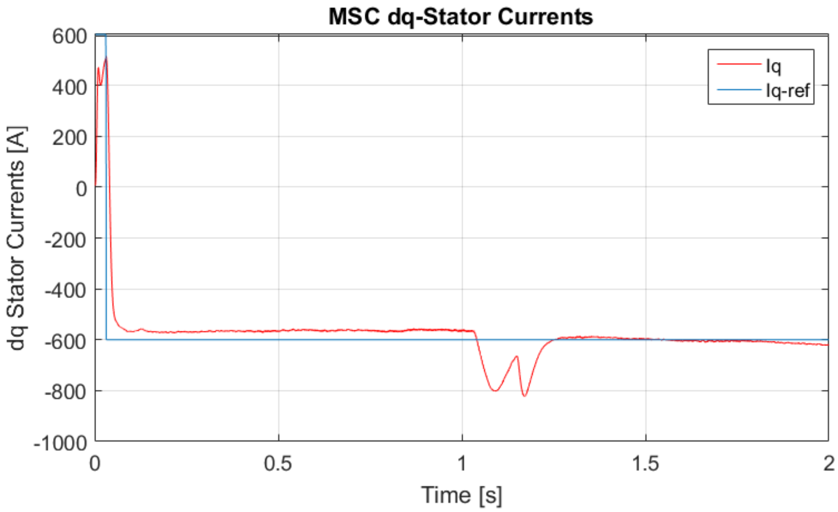

Figure 6.9: The simulated stator current *q*-component

6.2.4 Stator *abc* currents

The *abc* stator current waveform is shown in the figure 6.10 below. It is not perfectly sinusoidal because there are some harmonics left in the system. Since the focus of the research is on control design, these results are accepted for continual analysis of the system.

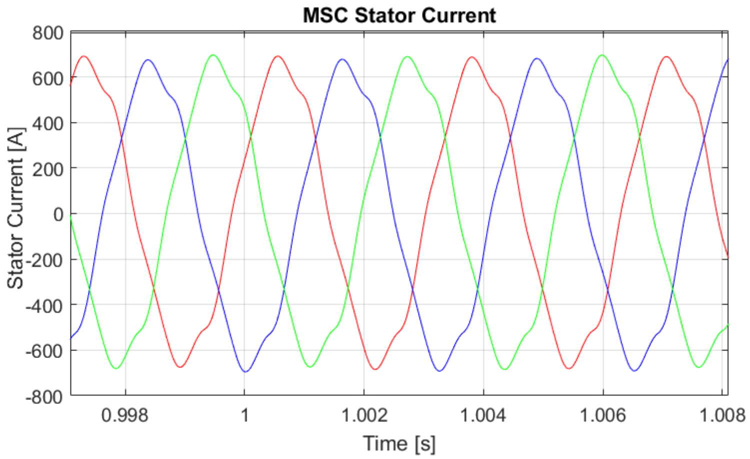

Figure 6.10: The simulated *abc* stator currents

6.2.5 Stator *abc* Voltage

The *abc* stator voltage graph is shown in figure 6.11 below. It has a good waveform which is within the accepted performance.

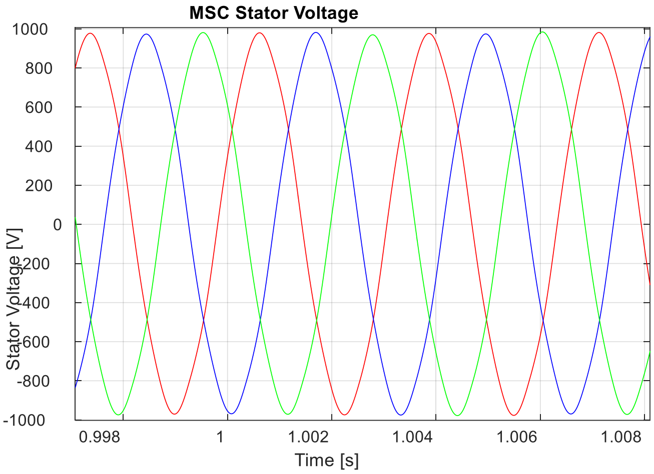

Figure 6.11: Zoomed in simulated *abc* stator currents

6.3 MSC results

This section presents the results obtained from the machine side of the converter.

6.3.1 SPWM carrier wave

Figure 6.12 below shows the carrier wave which is then compared to the input voltage from the controller corrected or modified signal using a comparator. This voltage is obtained after converting the *dq* controller voltage signals to the *abc* controller voltage signals.

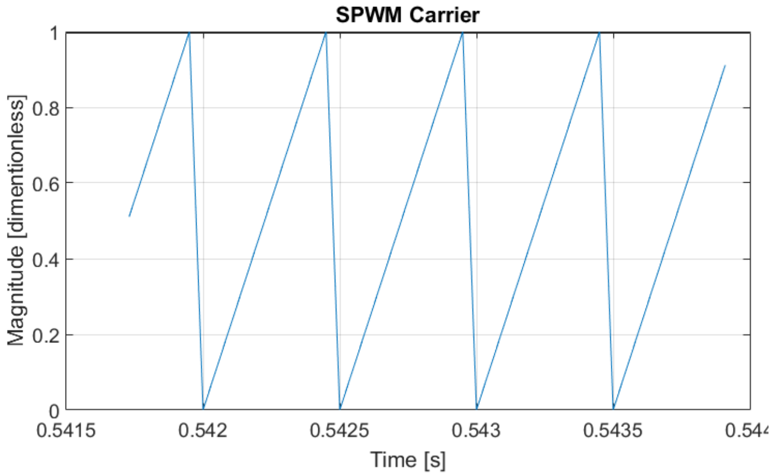

Figure 6.12: Zoomed in SPWM carrier signal waveform

6.3.2 SPWM triggering signals

The outputs of the comparator are the signals that are used to trigger the IGBTs on and off. Figure 6.13 below shows the PWM triggering signals results of the produced by the comparator.

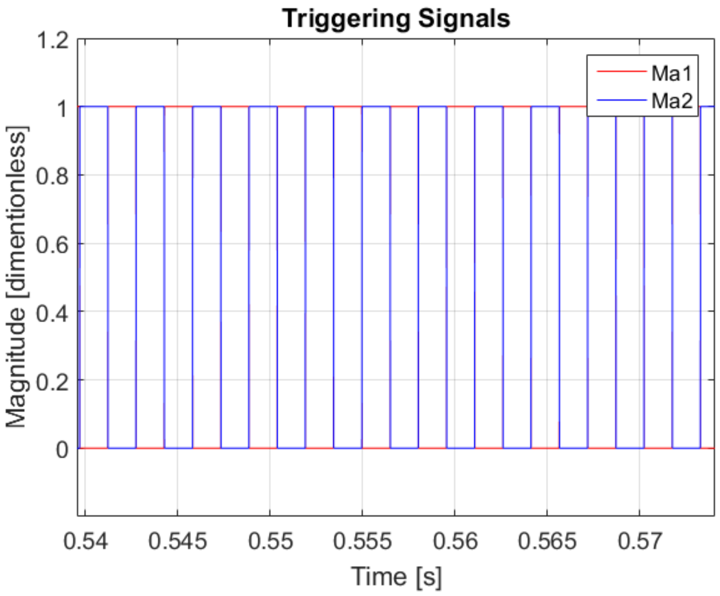

Figure 6.13: Triggering signals for the IGBTs

6.3.3 DC-link Voltage

DC-link voltage control is more challenging for a PMSG wind turbine than a DFIG wind turbine [82]. The controller performs to the desired DC voltage value with 5.477 % overshoot. It also effectively negates the changes at $t = 1$ s due to wind, see Fig.6.14.

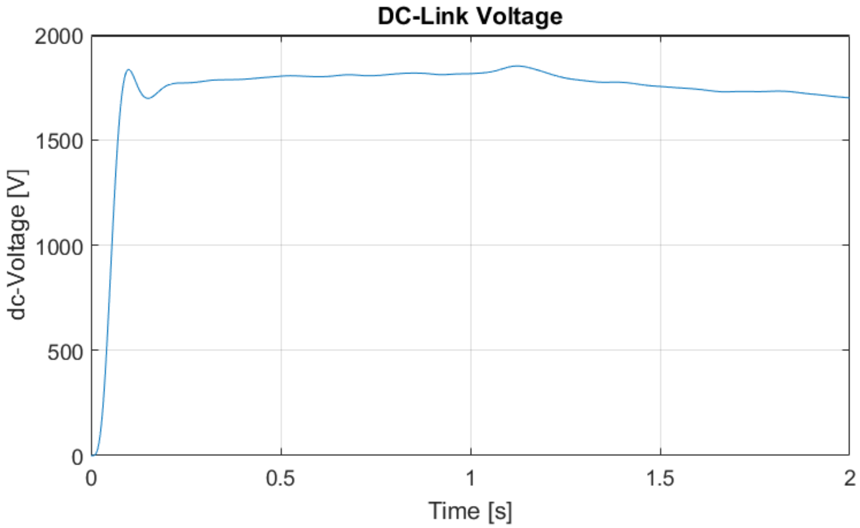

Figure 6.14: The simulated DC-link Voltage

It can be observed from figure 6.15 that the dc-voltage keeps constant throughout if the wind speed is kept constant. This effectively shows that the dc-voltage controller performs to the optimal level in which it is designed.

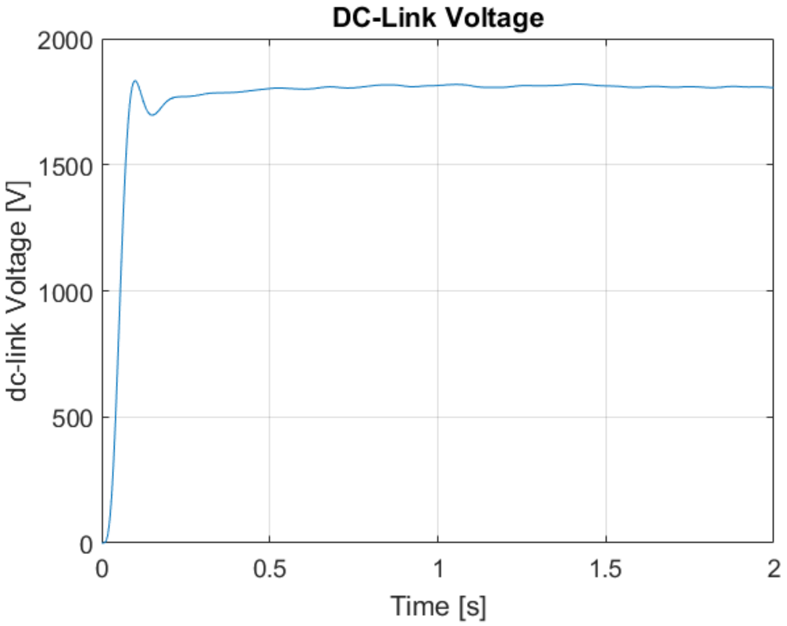

Figure 6.15: DC-Link Voltage simulated at constant wind speed of 6 *m/s*

6.4 GSC results

This section presents the results obtained from the grid side of the converter.

6.4.1 Grid Power system curves

The initial power produced at the speed of 6 m/s has double overshoot in the first 0.25s due to machine dynamics but the controller quickly settles it thereafter. The graphs in figure 6.17 show interesting information: the power produced by the PMSG system is perfectly passed through the converter to the grid as it is. This important observation validates the relationship between the converter power and the grid power:

$$P_{dc} = P_{ac} = I_{dc} V_{dc} \tag{6.8}$$

The reactive power has some spikes at the beginning due to machine responds when it is started then it remains slightly below zero throughout. This shows that the transmission grid is not made up of purely resistive parameters as it has an inductance. It gives an important derivation that the power factor of a transmission grid can never be equal to 1.
For the wind speed of 6 m/s, the measured active power and reactive power at t = 0.988s is P =1.407 MW and Q = 49.53 kVAr respectively. Therefore, the power factor (*p.f*) is:

$$\begin{gathered} Q = P\tan\theta \\ \tan\theta = \frac{Q}{P} \\ \theta = \tan^{-1}\left(\frac{49.53\ \text{kVAr}}{1.407\ \text{MW}}\right) \\ \therefore \cos\theta = 0.9993 \end{gathered} \tag{6.9}$$

Following the same calculation as above for the wind speed at 11 m/s, the power factor is found to be 0.9996 which is similar to the one at 6 m/s as expected.

The active power graph in figure 6.16 is negative. This may suggest that the VSC is drawing power from the utility grid. To fully understand how the power exchange occurs between the VSC and utility grid, a point of reference is assumed that the utility grid is modelled as an infinite bus hence $V_{ac} < 0^\circ$ (the voltage is assumed to be very constant). And the voltage produced by the VSC through modulation is modelled as $V_{conv} < \delta$ with δ being the phase shift angle. Then the apparent power transferred between the two systems is:

$$S_{ac} = V_{ac} I_{ac} \tag{6.10}$$

The current flowing through the transmission line depends on the phase reactor hence:

$$I_{ac} = \frac{V_{ac}\angle 0° - V_{con}\angle \delta°}{j\omega L_g} \tag{6.11}$$

∴

$$S_{ac} = V_{ac}\left[\frac{V_{ac}\angle 0° - V_{con}\angle \delta°}{j\omega L_g}\right] \tag{6.12}$$

Expanding the brackets and simplifying gives:

$$S_{ac} = \frac{-V_{ac}V_{conv}}{\omega L_g}\sin(\delta) + j\left(\frac{V_{ac}^2}{\omega L_g} - \frac{V_{ac}V_{conv}}{\omega L_g}\cos(\delta)\right) \tag{6.13}$$

It can be deduced from Eq. 6.13 that the active and reactive powers are:

$$P_{ac} = \frac{-V_{ac}V_{conv}}{\omega L_g}\sin(\delta) \tag{6.14}$$

$$Q_{ac} = j\left(\frac{V_{ac}^2}{\omega L_g} - \frac{V_{ac}V_{conv}}{\omega L_g}\cos(\delta)\right) \tag{6.15}$$

Let X_g be the transmission inductance, then

$$P_{ac} = \frac{-V_{ac}V_{conv}}{X_g}\sin(\delta) \tag{6.16}$$

$$Q_{ac} = j\left(\frac{V_{ac}^2}{X_g} - \frac{V_{ac}V_{conv}}{X_g}\cos(\delta)\right) \tag{6.17}$$

So the active power is negative because it flows into the utility grid as demonstrated by Eq. 6.16. The reactive power is below the zero regions as shown by Eq. 6.17. Since V_{ac} is approximately equal to V_{conv} the factor δ maintains the relationship.

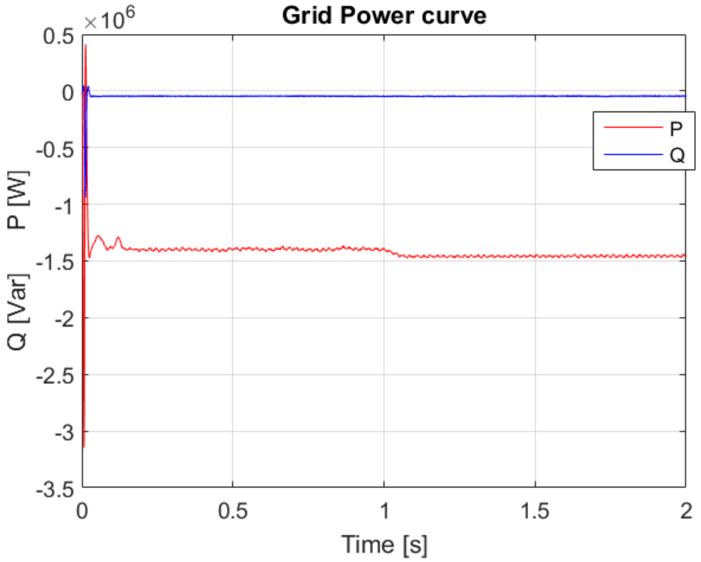

Figure 6.16: Grid simulated power curve showing the relationship of *P* and *Q*

The wind speed is varied from 6 m/s to 11 m/s at *t* = 1s. The active power increases gradually as it responds to the change in wind speed. At *t* = 1s, the reactive power remains constant because the voltage source is from the VSC grid side converter which controls the output voltage through adjusting the modulation index. Eq.6.18 shows the relationship between the grid voltage and the dc voltage. So, when the active power increases, the VSC quickly adjusts the index m, to keep the voltage constant.

$$u_g = u_{dc} \cdot m \cdot \frac{\sqrt{3}}{2\sqrt{2}} \tag{6.18}$$

6.4.2 Grid dq currents

The controller tracking performance is investigated using the grid *dq* currents in figure 6.18. The controller starts with a small double overshoot then keeps full tracking throughout the simulation period. At t =1*s*, the power production increases so the controller follows perfectly track of the reference. The Id current follows the lead of active power since they are related through this equation in Eq.6.17.

$$P_{ac} = \frac{3}{2}\left(u_d i_d + u_q i_q\right) \tag{6.19}$$

Since $U_q = 0$ from the assumption made in chapter 3 and is proven in figure 6.17 below, then

$$P_{ac} = -\frac{3}{2} u_d i_d \tag{6.20}$$

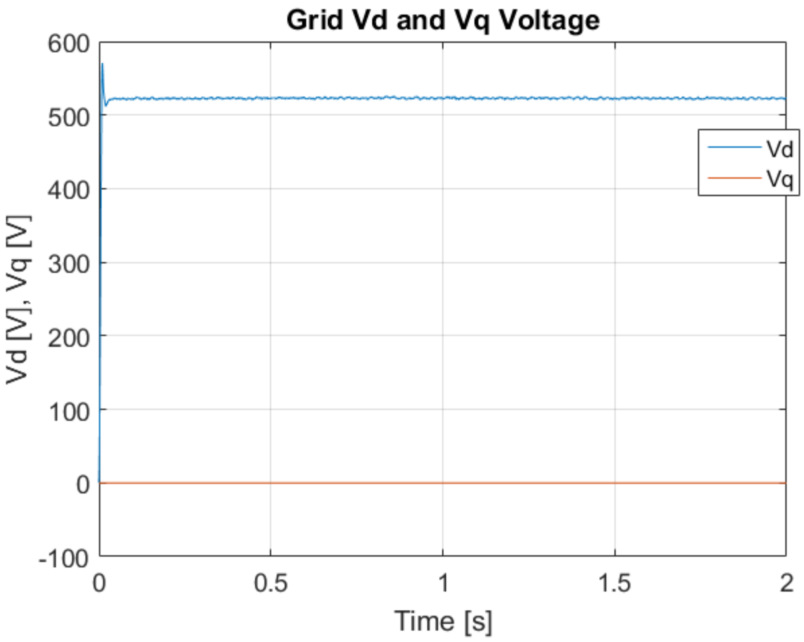

Figure 6.17: Grid Voltage *dq*-components

So, it can be deduced that the grid current d-component is directly controlled by the active power of the grid.

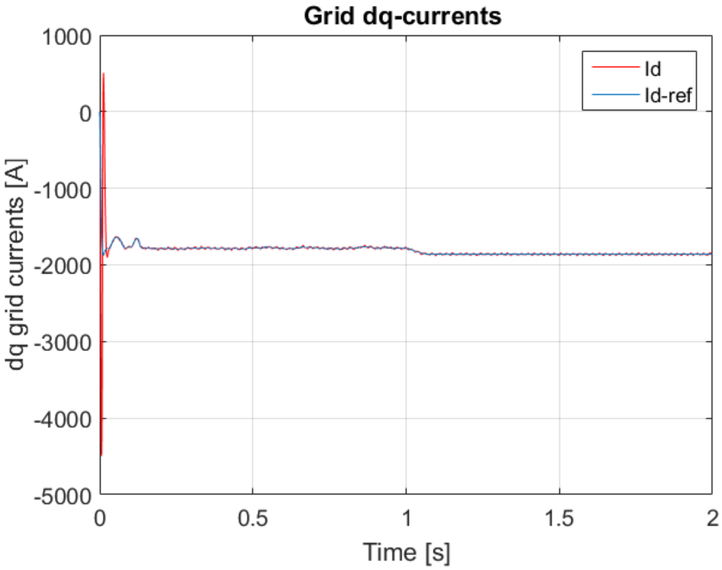

Figure 6.18: The simulated grid current *d*-component

Similarly, the grid current *q*-component is also used to investigate the controller tracking performance of the reactive power controller and the *q*-component of the inner current loop as shown in figure 6.19. The controller starts with a small double overshoot then keeps full tracking throughout the simulation period. At $t = 1s$, the reactive power production remains unchanged, so the controller keeps perfectly track of the reference. The I_q current follows the lead of the reactive power since they are related through this equation in Eq.6.21.

$$Q_{ac} = \frac{3}{2}\left(u_d i_q - u_q i_d\right) \tag{6.21}$$

Since $U_q = 0$ from the assumption made in chapter 3 and is proven in figure 6.18 above, then

$$Q_{ac} = \frac{3}{2} u_d i_q \tag{6.22}$$

So it can be deduced that the grid current q-component is directly controlled by the reactive power of the grid.

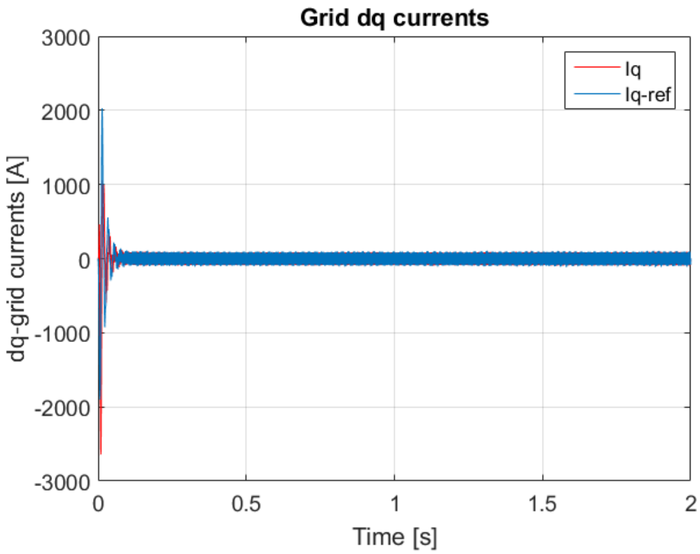

Figure 6.19: The simulated grid current *q*-component

6.4.3 Grid *abc* currents at PCC

The *abc* grid current graph is shown in figure 6.20 below. It has a good waveform which is within the accepted performance

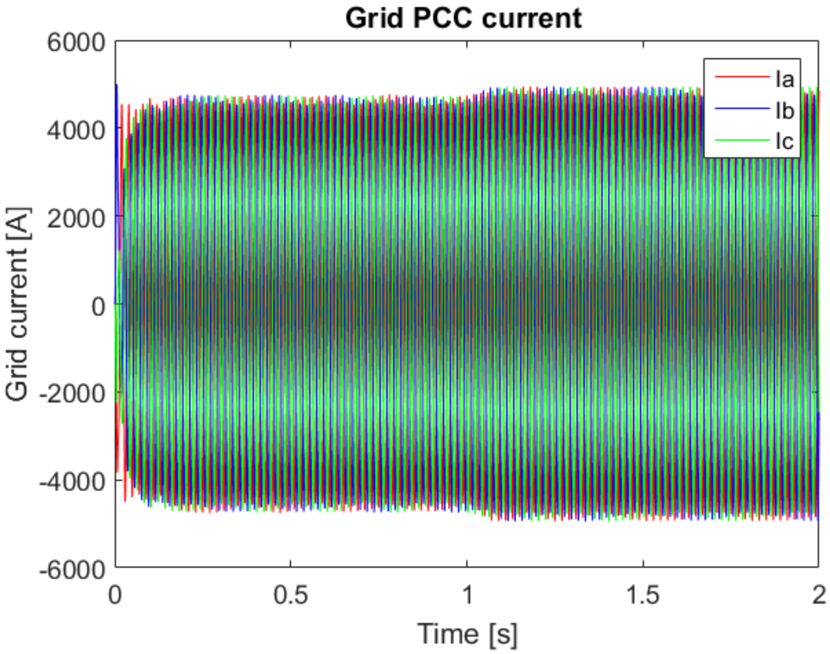

Figure 6.20: The full simulated *abc* grid current

The zoomed abc current at the PCC is shown in the figure 6.21 below. The waveform is clearly displaced 120°.

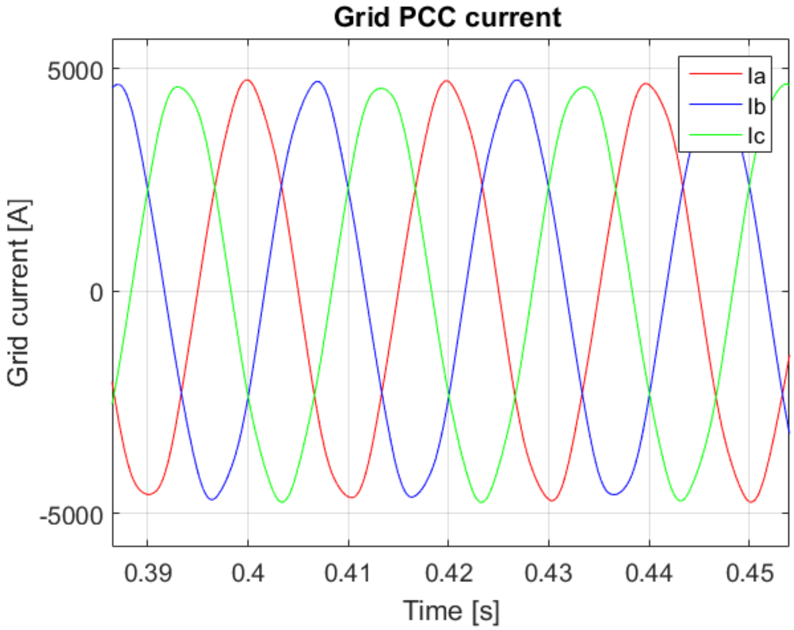

Figure 6.21: Zoomed in simulated *abc* grid current

6.4.4 Grid abc Voltage at the PCC

The *abc* grid voltage graph is shown in figure 6.22 below. It has a good waveform which is within the accepted performance.

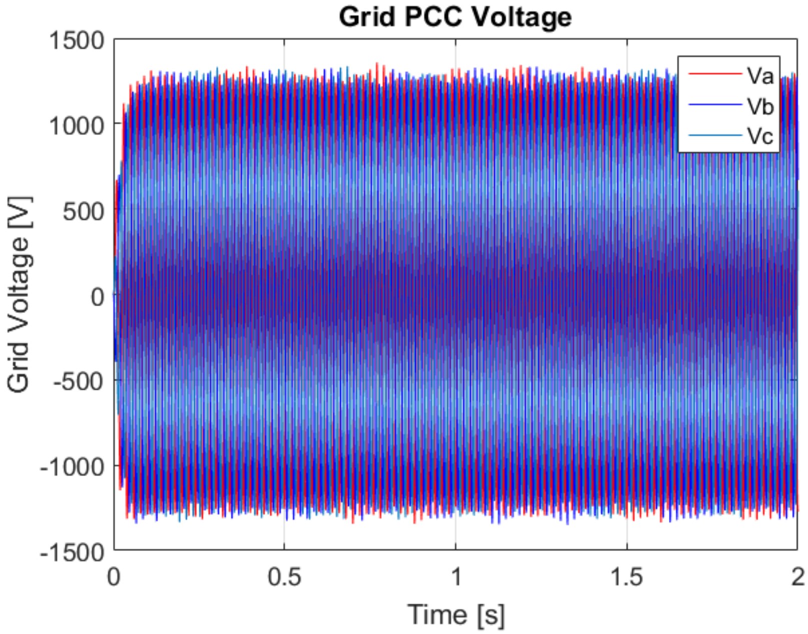

Figure 6.22: The full simulated *abc* grid voltage waveform

The zoomed *abc* voltage at the PCC is shown in the figure 6.23 below. The waveform is clearly displaced 120°.

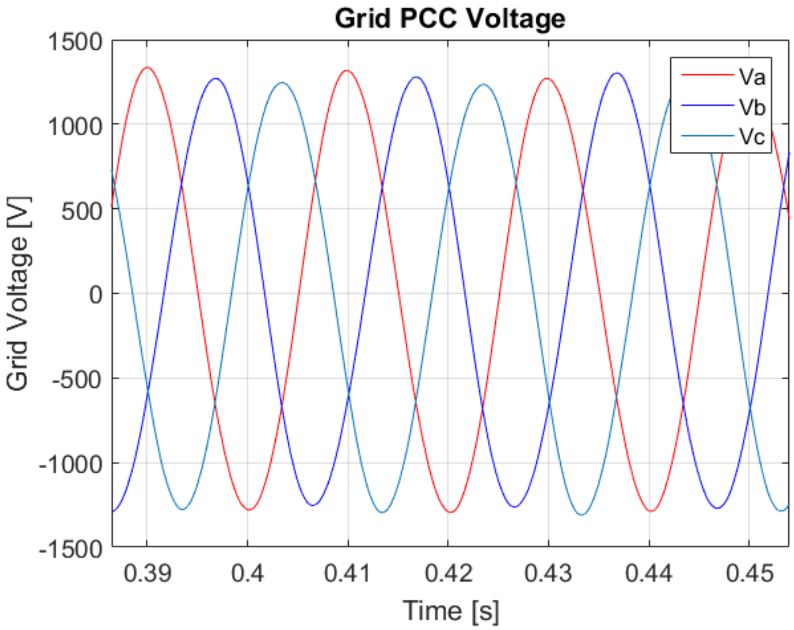

Figure 6.23: Zoomed in *abc* grid voltage waveform

CHAPTER 7: CONCLUSION AND FUTURE WORKS

This chapter provides a conclusion from the system project and the discussions made. It further makes future suggestions on how the system can be developed and applied in other projects.

7.1 Conclusion

The research work carried out in this project presented successful results. The direct PI controller without the feedforward terms was designed to attain optimum performance. The key to achieve optimum performance of a controller is the development of a super accurate mathematical modelling of the system. Chapter 2 set out the detailed mathematical modelling of a wind turbine and a PMSG.

The system was further modelled in the state-space model to enable researchers who are working on small signal analysis of the VSC-based PMSG to use the state-space models for their analysis of the system. Chapter 3 added further detailed mathematical model of the VSC-HVDC. The proposed decoupling method was introduced, and a thorough decoupling process was employed to produce the decoupled transfer functions of the inner current control loops. The optimal torque control MPPT algorithm and vector control method were applied to implement the system.

In chapter 4, the components used for the PMSG and VSC-HVDC systems were rated and sized in accordance with set standards and safety measures. The implementation of the components in Psim was also investigated. Chapter 5 presented the design procedures that were carried out to produce all the controllers for the VSC-based PMSG system.

Finally, chapter 6 investigated the performance of the thoroughly designed PI controllers for the system. The direct PI controller configuration without the decoupled terms was implemented. Based on the results obtained, this thesis successfully implemented the new proposed controller configuration. It can be deduced, therefore, that VSC-based PMSG can be implemented using a direct PI controller to reduce system complexity and improve controller performance.

7.2 Future works

This thesis has successfully demonstrated a new direct PI controller without the decoupled terms. It successfully further tested and implemented it in a VSC-based PMSG and obtained satisfactory good results. The direct PI controller without the decoupled terms research work can be extended to other wind turbines that are VSC-based such as DFIG, SCIG. Fluctuations in the grid can be considered to assess the robustness of the system.

In addition to that, since the VSC has been proven in this thesis to separately control the active and reactive powers, it can be proposed that a three-terminal VSC-based HVDC system be developed for a DFIG wind turbine. Since the stator winding is usually connected directly to the grid, it is proposed that it be connected to the third terminal of the VSC with the machine side converter connected to the rotor winding and the grid side converter connected to the utility grid. This proposal stems from the fact that the VSC can consume or supply a reactive power to produce the magnetic current in the DFIG turbine, the VSC can supply the reactive power as it is able to provide full independent control of the active and reactive power. Following the successful handling of the controllers in this thesis, the controllers are more capable to achieve that objective of supplying the DFIG stator winding with a reactive power from the VSC.

REFERENCES

[1] H. Polinder, J. A. Ferreira, B. B. Jensen, A. B. Abrahamsen, K. Atallah, and R. A. McMahon, "Trends in wind turbine generator systems," *IEEE Journal of Emerging and Selected Topics in Power Electronics,* vol. 1, pp. 174-185, 2013.

[2] M. R. Patel, *Wind and solar power systems: design, analysis, and operation*: CRC press, 2005.

[3] B. Wu, Y. Lang, N. Zargari, and S. Kouro, *Power conversion and control of wind energy systems* vol. 76: John Wiley & Sons, 2011.

[4] M. E. Haque, M. Negnevitsky, and K. M. Muttaqi, "A novel control strategy for a variable speed wind turbine with a permanent magnet synchronous generator," in *Industry Applications Society Annual Meeting, 2008. IAS'08. IEEE*, 2008, pp. 1-8.

[5] Y. Chen, P. Pillay, and A. Khan, "PM wind generator topologies," *IEEE Transactions on Industry Applications,* vol. 41, pp. 1619-1626, 2005.

[6] S. Li, T. A. Haskew, R. P. Swatloski, and W. Gathings, "Optimal and direct-current vector control of direct-driven PMSG wind turbines," *IEEE Transactions on power electronics,* vol. 27, pp. 2325-2337, 2012.

[7] N. Hingorani and L. Gyuyi, "Understanding Facts–Concepts and Technology of Flexible AC Transmission Systems: Inst. Elect," ed: Electronic Eng. Press, 1999.

[8] K. Dai, P. Liu, Y. Kang, and J. Chen, "Decoupling current control for voltage source converter in synchronous roating frame," in *Power Electronics and Drive Systems, 2001. Proceedings., 2001 4th IEEE International Conference on*, 2001, pp. 39-43.

[9] Y. Ye, M. Kazerani, and V. Quintana, "A novel modeling and control method for three-phase PWM converters," in *Power Electronics Specialists Conference, 2001. PESC. 2001 IEEE 32nd Annual*, 2001, pp. 102-107.

[10] A. Tabesh and R. Iravani, "Multivariable dynamic model and robust control of a voltage-source converter for power system applications," *IEEE Transactions on Power Delivery,* vol. 24, pp. 462-471, 2009.

[11] A. Eberhard, J. Leigland, and J. Kolker, *South Africa's Renewable Energy IPP Procurement Program*: World Bank Publications, 2014.

[12] G. W. E. Council and G. W. Statistics, "Electronic resource," *Global Wind Statistics 2017.—Mode of access:<http://gwec.net/global-figures/graphs/ Date of access 18 March 2018* 2017.

[13] O. Noureldeen and A. Rashad, "Modeling and investigation of Gulf El-Zayt wind farm for stability studying during extreme gust wind occurrence," *Ain Shams Engineering Journal,* vol. 5, pp. 137-148, 2014.

[14] G. O. G. Tande, "Grid Connection of Deep Sea Wind Farms–Options and Challenges," *SINTEF Energy research, www. we-at-sea. org/docs/sessie 3_ tande deep sea grid iea annex,* vol. 23.

[15] T. M. Haileselassie, "Control of multi-terminal VSC-HVDC systems," Institutt for elkraftteknikk, 2008.

[16] T. Magg, M. Manchen, E. Krige, J. Wasborg, and J. Sundin, "Connecting networks with VSC HVDC in Africa: Caprivi Link interconnector," in *Power Engineering Society Conference and Exposition in Africa (PowerAfrica), 2012 IEEE*, 2012, pp. 1-6.

[17] G. Stamatiou, "Converter interactions in VSC-based HVDC systems," 2015.

[18] J. Belhadj and X. Roboam, "Investigation of different methods to control a small variable-speed wind turbine with PMSM drives," *Journal of Energy Resources Technology,* vol. 129, pp. 200-213, 2007.

[19] P. Kundur, N. J. Balu, and M. G. Lauby, *Power system stability and control* vol. 7: McGraw-hill New York, 1994.

[20] G. Michalke, A. D. Hansen, and T. Hartkopf, "Control strategy of a variable speed wind turbine with multipole permanent magnet synchronous generator," in *2007 European Wind Energy Conference and Exhibition*, 2007.

[21] A. D. Hansen and G. Michalke, "Modelling and control of variable-speed multi-pole permanent magnet synchronous generator wind turbine," *Wind Energy,* vol. 11, pp. 537-554, 2008.

[22] M. A. Poller, "Doubly-fed induction machine models for stability assessment of wind farms," in *Power Tech Conference Proceedings, 2003 IEEE Bologna*, 2003, p. 6 pp. Vol. 3.

[23] A. M. Howlader, N. Urasaki, A. Yona, T. Senjyu, and A. Y. Saber, "A review of output power smoothing methods for wind energy conversion systems," *Renewable and Sustainable Energy Reviews,* vol. 26, pp. 135-146, 2013.

[24] M. A. Abdullah, A. Yatim, C. Tan, and R. Saidur, "A review of maximum power point tracking algorithms for wind energy systems," *Renewable and sustainable energy reviews,* vol. 16, pp. 3220-3227, 2012.

[25] C. Vlad, I. Munteanu, A. I. Bratcu, and E. Ceangă, "Output power maximization of low-power wind energy conversion systems revisited: Possible control solutions," *Energy Conversion and Management,* vol. 51, pp. 305-310, 2010.

[26] Y.-Y. Hong, S.-D. Lu, and C.-S. Chiou, "MPPT for PM wind generator using gradient approximation," *Energy Conversion and Management,* vol. 50, pp. 82-89, 2009.

[27] H. Camblong, I. M. de Alegria, M. Rodriguez, and G. Abad, "Experimental evaluation of wind turbines maximum power point tracking controllers," *Energy Conversion and Management,* vol. 47, pp. 2846-2858, 2006.

[28] A. Yazdani and R. Iravani, *Voltage-sourced converters in power systems: modeling, control, and applications*: John Wiley & Sons, 2010.

[29] Y. Zou, M. Elbuluk, and Y. Sozer, "Stability analysis of maximum power point tracking (MPPT) method in wind power systems," in *Industry Applications Society Annual Meeting (IAS), 2011 IEEE*, 2011, pp. 1-8.

[30] K.-H. Kim, T. L. Van, D.-C. Lee, S.-H. Song, and E.-H. Kim, "Maximum output power tracking control in variable-speed wind turbine systems considering rotor inertial power," *IEEE transactions on industrial electronics,* vol. 60, pp. 3207-3217, 2013.

[31] M. Nasiri, J. Milimonfared, and S. Fathi, "Modeling, analysis and comparison of TSR and OTC methods for MPPT and power smoothing in permanent magnet synchronous generator-based wind turbines," *Energy Conversion and Management,* vol. 86, pp. 892-900, 2014.

[32] A. M. Howlader, N. Urasaki, T. Senjyu, A. Uehara, A. Yona, and A. Saber, "Output power smoothing of wind turbine generation system for the 2-MW permanent magnet synchronous generators," in *Electrical Machines and Systems (ICEMS), 2010 International Conference on*, 2010, pp. 452-457.

[33] A. Abedini and A. Nasiri, "Applications of super capacitors for PMSG wind turbine power smoothing," in *Industrial Electronics, 2008. IECON 2008. 34th Annual Conference of IEEE*, 2008, pp. 3347-3351.

[34] O. Anaya-Lara, N. Jenkins, J. B. Ekanayake, P. Cartwright, and M. Hughes, *Wind energy generation: modelling and control*: John Wiley & Sons, 2011.

[35] M. Lydia, A. I. Selvakumar, S. S. Kumar, and G. E. P. Kumar, "Advanced algorithms for wind turbine power curve modeling," *IEEE Transactions on sustainable energy,* vol. 4, pp. 827-835, 2013.

[36] M. Lydia, S. S. Kumar, A. I. Selvakumar, and G. E. P. Kumar, "A comprehensive review on wind turbine power curve modeling techniques," *Renewable and Sustainable Energy Reviews,* vol. 30, pp. 452-460, 2014.

[37] S. Heier, *Grid integration of wind energy: onshore and offshore conversion systems*: John Wiley & Sons, 2014.

[38] S. Muyeen, J. Tamura, and T. Murata, *Stability augmentation of a grid-connected wind farm*: Springer Science & Business Media, 2008.

[39] D. Petković, Ž. Ćojbašič, and V. Nikolić, "Adaptive neuro-fuzzy approach for wind turbine power coefficient estimation," *Renewable and Sustainable Energy Reviews,* vol. 28, pp. 191-195, 2013.

[40] I. Buehring and L. Freris, "Control policies for wind-energy conversion systems," in *IEE Proceedings C (Generation, Transmission and Distribution)*, 1981, pp. 253-261.

[41] A. M. Knight and G. E. Peters, "Simple wind energy controller for an expanded operating range," *IEEE Transactions on Energy Conversion,* vol. 20, pp. 459-466, 2005.

[42] D. Kumar and K. Chatterjee, "A review of conventional and advanced MPPT algorithms for wind energy systems," *Renewable and sustainable energy reviews,* vol. 55, pp. 957-970, 2016.

[43] S. Ganjefar, A. A. Ghassemi, and M. M. Ahmadi, "Improving efficiency of two-type maximum power point tracking methods of tip-speed ratio and optimum torque in wind turbine system using a quantum neural network," *Energy,* vol. 67, pp. 444-453, 2014.

[44] S. Morimoto, H. Nakayama, M. Sanada, and Y. Takeda, "Sensorless output maximization control for variable-speed wind generation system using IPMSG," in *Industry Applications Conference, 2003. 38th IAS Annual Meeting. Conference Record of the*, 2003, pp. 1464-1471.

[45] A. Dahbi, M. Hachemi, N. Nait-Said, and M.-S. Nait-Said, "Realization and control of a wind turbine connected to the grid by using PMSG," *Energy Conversion and Management,* vol. 84, pp. 346-353, 2014.

[46] F. Blaabjerg, M. Liserre, and K. Ma, "Power electronics converters for wind turbine systems," *IEEE transactions on Industry Applications,* vol. 48, pp. 708-719, 2012.

[47] N. Huang, "Simulation of power control of a wind turbine permanent magnet synchronous generator system," 2013.

[48] K. Khan, S. Javed Arif, and M. Jamil Asghar, "Harnessing Low Power Wind Energy from Riverine and Isolated Potential Pockets using Wound Rotor Induction Machines," *J Earth Sci Climat Change S,* vol. 12, p. 2, 2012.

[49] H.-W. Kim, S.-S. Kim, and H.-S. Ko, "Modeling and control of PMSG-based variable-speed wind turbine," *Electric Power Systems Research,* vol. 80, pp. 46-52, 2010.

[50] H. Merabet Boulouiha, A. Allali, A. Tahri, A. Draou, and M. Denai, "A simple maximum power point tracking based control strategy applied to a variable speed squirrel cage induction generator," *Journal of Renewable and Sustainable Energy,* vol. 4, p. 053124, 2012.

[51] N. Freire, J. Estima, and A. Cardoso, "A comparative analysis of PMSG drives based on vector control and direct control techniques for wind turbine applications," *Przegląd Elektrotechniczny,* vol. 88, pp. 184-187, 2012.

[52] L. Xu, L. Yao, and C. Sasse, "Grid integration of large DFIG-based wind farms using VSC transmission," *IEEE Transactions on Power Systems,* vol. 22, pp. 976-984, 2007.

[53] N. Flourentzou, V. G. Agelidis, and G. D. Demetriades, "VSC-based HVDC power transmission systems: An overview," *IEEE Transactions on power electronics,* vol. 24, pp. 592-602, 2009.

[54] L. Harnefors, M. Bongiorno, and S. Lundberg, "Input-admittance calculation and shaping for controlled voltage-source converters," *IEEE transactions on industrial electronics,* vol. 54, pp. 3323-3334, 2007.

[55] P. Haugland, "It's time to connect: Technical description of HVDC Light® technology," *ABB Techincal Report,* 2008.

[56] Y. Jiang, "Active and reactive power control for transmission system with voltage souce converters," Institutionen för elkraftteknik, 1997.

[57] C. Du, *VSC-HVDC for industrial power systems*: Chalmers University of Technology, 2007.

[58] C. Bajracharya, "Control of VSC-HVDC for wind power," ed: Institutt for elkraftteknikk, 2008.

[59] T. W. Shire, "VSC-HVDC based network reinforcement," *Delft University of Technology, Delft,* 2009.

[60] L. Wang and N. Ertugrul, "Selection of PI compensator parameters for VSC-HVDC system using decoupled control strategy," in *Universities Power Engineering Conference (AUPEC), 2010 20th Australasian*, 2010, pp. 1-7.

[61] L. Harnefors and H.-P. Nee, "Model-based current control of AC machines using the internal model control method," *IEEE Transactions on Industry Applications,* vol. 34, pp. 133-141, 1998.

[62] M. Beza, "Control of energy storage equipped shunt-connected converter for electric power system stability enhancement," 2012.

[63] L. Angquist and M. Bongiorno, "Auto-normalizing phase-locked loop for grid-connected converters," in *Energy Conversion Congress and Exposition, 2009. ECCE 2009. IEEE*, 2009, pp. 2957-2964.

[64] !!! INVALID CITATION !!!

[65] D. Watson. *,"Wind turbines and the wind energy - how much power is in the wind?"*. Available: http://www.ftexploring.com/energy/wind-enrgy.html

[66] A. Betz, "Behavior of vortex systems," 1933.

[67] S. Chichester, "Grid integration of wind energy conversion systems," *Wiley, 385p,* 1999.

[68] O. Wasynczuk, D. Man, and J. Sullivan, "Dynamic behavior of a class of wind turbine generators during randon wind fluctuations," *IEEE Transactions on power apparatus and systems*, pp. 2837-2845, 1981.

[69] P. Anderson and A. Bose, "Stability simulation of wind turbine systems," *IEEE transactions on power apparatus and systems*, pp. 3791-3795, 1983.

[70] C. Carrillo, A. O. Montaño, J. Cidrás, and E. Díaz-Dorado, "Review of power curve modelling for wind turbines," *Renewable and Sustainable Energy Reviews*, vol. 21, pp. 572-581, 2013.

[71] E. Koutroulis and K. Kalaitzakis, "Design of a maximum power tracking system for wind-energy-conversion applications," *IEEE transactions on industrial electronics*, vol. 53, pp. 486-494, 2006.

[72] V. Akhmatov, "Analysis of dynamic behavior of electric power systems with large amount of wind power," *Electrical Power Engineering*, 2003.

[73] V. Akhamatov, A. Nielsen, J. Pedersen, and O. Nymann, "Variable speed wind turbines with multi-pole synchronous permanent magnet generators. Part 1: Modelling in dynamic simulation tools," *Wind Engergy*, pp. 531-548, 2003.

[74] G. Michalke, A. D. Hansen, and T. Hartkopf, "Control strategy of a variable speed wind turbine with multipole permanent magnet synchronous generator," in *2007 European Wind Energy Conference and Exhibition*, 2007.

[75] E. Spooner and A. Williamson, "Direct coupled, permanent magnet generators for wind turbine applications," *IEE Proceedings-Electric Power Applications*, vol. 143, pp. 1-8, 1996.

[76] A. E. Fitzgerald, C. Kingsley, S. D. Umans, and B. James, *Electric machinery* vol. 5: McGraw-Hill New York, 2003.

[77] O. Gomis-Bellmunt, A. Junyent-Ferré, A. Sumper, and J. Bergas-Jané, "Control of a wind farm based on synchronous generators with a central HVDC-VSC converter," *IEEE Transactions on power systems*, vol. 26, pp. 1632-1640, 2011.

[78] O. Katsuhiko, "Modern control engineering," ed, 2010.

[79] T. W. Shire, "VSC-HVDC based Network Reinforcement," Masters, Department of High-Voltage Components and Power Systems, Delft University of Technology, 2009.

[80] Y. Errami, M. Ouassaid, and M. Maaroufi, "Control of a PMSG based wind energy generation system for power maximization and grid fault conditions," *Energy Procedia*, vol. 42, pp. 220-229, 2013.

[81] A. D. Hansen and G. Michalke, "Multi-pole permanent magnet synchronous generator wind turbines' grid support capability in uninterrupted operation during grid faults," *IET Renewable Power Generation*, vol. 3, pp. 333-348, 2009.

[82] G. Michalke and A. D. Hansen, "Modelling and control of variable speed wind turbines for power system studies," *Wind Energy*, vol. 13, pp. 307-322, 2010.

[83] S. M. Tripathi, A. N. Tiwari, and S. Deependra, "Grid-integrated permanent magnet synchronous generator based wind energy conversion systems: A technology review," *Renewable and Sustainable Energy Reviews*, vol. 51, pp. 1288-1305, 2015.

[84] S. R. Bowes and S. Grewal, "A novel harmonic elimination PWM strategy," in *Seventh International Conference on Power Electronics and Variable Speed Drives*, London, 1998, pp. 426-432.

[85] Y. Oğuz, İ. Güney, and H. Çalık, "Power quality control and design of power converter for variable-speed wind energy conversion system with permanent-magnet synchronous generator," *The Scientific World Journal,* vol. 2013, 2013.

[86] N. Shore, K. Adamson, P. Bard, R. Burton, C. Clarke, A. Coutu, *et al.*, "DC side filters for multiterminal HVDC systems," *IEEE Transactions on Power Delivery,* vol. 11, pp. 1970-1984, 1996.

[87] C. Smith, M. Redfern, and S. Potts, "Improvement in the performance of on-load tap changer transformers operating in series," in *Power Engineering Society General Meeting, 2003, IEEE*, 2003, pp. 1905-1905.

[88] H. ABB, "R Light It’s Time to Connect," ed: Technical Brochure, Dec, 2012.

[89] N.-Y. Dai and M.-C. Wong, "Design considerations of coupling inductance for active power filters," in *Industrial Electronics and Applications (ICIEA), 2011 6th IEEE Conference on*, 2011, pp. 1370-1375.

[90] H. ABB, "Light It’s time to connect, Technical Brochure, Dec. 2012," ed.

[91] G. Adam, *Voltage Source Converter: modulation, modelling, control and applications in power systems*, 2014.

[92] J. Arrillaga, *High voltage direct current transmission*: Iet, 1998.

[93] G. J. Wakileh, *Power systems harmonics: fundamentals, analysis and filter design*: Springer Science & Business Media, 2001.

APPENDIX A : MSC INNER CURRENT CONTROLLER MATLAB CODE

```
%PI Controller design for the inner current q-component
clc
R = 0.821e-3;  %stator resistance
L= 1.5731e-3;  %stator inductance

A= [-R/L 0;0 -R/L];
B=[1/L 0;0 0];
C=[1 0];
D=[0];

T=ss(A,B,C,D);
T=tf(T)

%Since this returns two transfer outputs for the two inputs, reset the transfer as given on
%to form 1 output

s=tf('s')
Td= 635.7/(s+0.5219)

Tdc = Td/(Td+1)

%step(Tdc)

pidtool(Tdc)
```

APPENDIX B: MSC DIRECT VOLTAGE CONTROLLER MATLAB CODE

```
%PI Controller design for the Vdc-component
 R = 0.821e-3;
L= 1.5731e-3;
Cap = 11.83e-3;
Kp = 3.1981
Ki = 2046.3904

A= [-R/L 0;0 -R/L];
B=[1/L 0;0 0];
C=[1 0];
D=[0];

T=ss(A,B,C,D);
T=tf(T)
 %Since this returns two transfer outputs for the two inputs, reset the transfer as given on
%to form 1 output
 Td= 635.7/(s+0.5219);
 Tdc = Td/(Td+1)    %Inner current transfer function
C_inner_GSC = Kp + Ki/s % Inner designed controller parameters
Tinner = Td*C_inner_GSC/(Td*C_inner_GSC+1) %%%Tunned Inner Transfer function or the controlled inner transfer function

%%%%%% Outer controller design  %%%%%%%%%%
s=tf('s');
Tdc_vol=1/(s*Cap)   %%Vdc-voltage Transfer function
Tdc_control=Tinner*Tdc_vol/(Tinner*Tdc_vol+1) %%% Closed loop transfer function

%step(Tinner)

pidtool(Tdc_control)
```

APPENDIX C: MSC STATOR VOLTAGE CONTROLLER MATLAB CODE

```
%PI Controller design for the Stator Voltage
 R = 0.821e-3;
L= 1.5731e-3;
 A= [-R/L 0;0 -R/L];
B=[1/L 0;0 0];
C=[1 0];
D=[0];

T=ss(A,B,C,D);
T=tf(T)
 %Since this returns two transfer outputs for the two inputs, reset the transfer as given on
%to form 1 output
 Td= 635.7/(s+0.5219);
 Tdc = Td/(Td+1)    %Inner current transfer function
C_inner_GSC = Kp + Ki/s % Inner designed controller parameters
Tinner = Td*C_inner_GSC/(Td*C_inner_GSC+1) %%%Tunned Inner closed loop Transfer function or the controlled inner transfer function

%%%%%% Outer controller design %%%%%%%%%%
s=tf('s');
Tsta_vol=1.5/(s*L)   %%Vdc-voltage Transfer function
Tac_control=Tinner*Tsta_vol/(Tinner*Tdc_vol+1) %%% Closed loop transfer function

%step(Tinner)

pidtool(Tac_control)
```

APPENDIX D: GSC INNER CURRENT CONTROLLER MATLAB CODE

```
%PI Controller design for the GSC Inner current-component
clc
R = 0.821e-3;
L= 0.0875e-3;

A= [-R/L 0;0 -R/L];
B=[1/L 0;0 0];
C=[1 0];
D=[0];

T=ss(A,B,C,D);
T=tf(T)

%Since this returns two transfer outputs for the two inputs, reset the transfer as given on
%to form 1 output

Td= 1.143e4/(s+9.383)

Tdc = Td/(Td+1)

%step(Tdc)
pidtool(Tdc)
```

APPENDIX E: GSC ACTIVE POWER CONTROLLER MATLAB CODE

```
%PI Controller design for the P-component
 R = 0.821e-3;
L= 0.0875e-3;
Vd=530
Kp = 2.2306e5;
Ki = 1033.8281;

A= [-R/L 0;0 -R/L];
B=[1/L 0;0 0];
C=[1 0];
D=[0];

T=ss(A,B,C,D);
T=tf(T)

%Since this returns two transfer outputs for the two inputs, reset the transfer as given on
%to form 1 output

Td= 1.143e4/(s+9.383)

Tdc = Td/(Td+1)    %Inner current transfer function

C_inner_GSC = Kp + Ki/s % Inner designed controller parameters

Tinner = Td*C_inner_GSC/(Td*C_inner_GSC+1) %%%Tunned Inner Transfer function or the controlled inner transfer function

%%%%%% Outer controller design  %%%%%%%%%%

Tpower=Tinner*1.5*Vd/(Tinner*1.5*Vd+1)

%step(Tinner)
```

```
pidtool(Tpower)
```

APPENDIX F: GSC REACTIVE POWER CONTROLLER MATLAB CODE

```
%PI Controller design for the Q-component
 R = 0.821e-3;
L= 0.0875e-3;
Vd=530
Kp = 2.2306e5;
Ki = 1033.8281;

A= [-R/L 0;0 -R/L];
B=[1/L 0;0 0];
C=[1 0];
D=[0];
 T=ss(A,B,C,D);
T=tf(T)
 %Since this returns two transfer outputs for the two inputs, reset the transfer as given on
%to form 1 output
 Td= 1.143e4/(s+9.383)
 Tdc = Td/(Td+1)    %Inner current transfer function
 C_inner_GSC = Kp + Ki/s % Inner designed controller parameters
 Tinner = Td*C_inner_GSC/(Td*C_inner_GSC+1) %%%Tunned Inner Transfer function or the controlled inner transfer function
 %%%%%% Outer controller design  %%%%%%%%%%
 Tpower=Tinner*1.5*Vd/(Tinner*1.5*Vd+1)

%step(Tinner)
 pidtool(Tpower)
```

APPENDIX G: PITCH ANGLE CONTROLLER MATLAB CODE

```
%PI Controller design for the PITCH ANGLE CONTROLLER
clear
clc

B=2000;
J=6250;
Tb=0.1;
Tm=848.83e3;
Te=32.65e3;

s=tf('s')

Tf=(1/(Tb*s+1)*((Tm-Te)/(J*s+B)))

pidtool(Tf)
```